UNIVERSITÀ
DEGLI STUDI
DI PADOVA

Sede Amministrativa: *Università degli Studi di Padova*

CISAS - Centro d'Ateneo di Studi e Attività Spaziali "G. Colombo"

CORSO DI DOTTORATO DI RICERCA IN: Scienze Tecnologie e Misure Spaziali

CURRICOLO: Misure Meccaniche per l'Ingegneria e lo Spazio (MMIS)

CICLO XXIX

Blade Tip Timing and Blade Tip Clearance Measurement System Based on Magnetoresistive Sensors

Coordinatore Corso: *Ch.mo Prof. Giampiero Naletto*

Coordinatore Curricolo: *Ch.mo Prof. Stefano Debei*

Supervisore: *Ch.mo Prof. Gianluca Rossi*

Dottorando: *Roberto Tomassini*

"Innovazione è vedere ciò che hanno visto tutti

e pensare ciò che nessuno ha pensato"

Albert Szint Gurgyi

Abstract

The accurate control of running gaps between static and rotating components is vital to preserve mechanical integrity and ensure a correct functioning of any rotating machinery. In aero-engines, tip leakage above the airfoil tip results in relevant aerodynamic losses, therefore the gap between the rotor blades tip and the casing must be the smallest possible, but enough to avoid contacts. One way to measure and monitoring tip gap is by a Blade Tip Clearance (BTC) technique.

The measurement of blade vibrations and eigen frequencies is also a crucial part of the development of any new gas turbine or aero-engine. For more than half a century, this has been performed by installing strain gauges on the blades and using telemetry to transmit the signals. The Blade Tip Timing (BTT) technique, (i.e. measuring the blade time of arrival from the casing at different angular locations with proximity sensors) is currently being adopted by all manufacturers as a replacement for the classical strain gauge technique because of its non-intrusive character.

However, the aero engines presents an extremely challenging environment for the application of reliable in-service instrumentation. Current studies focus on sensors development, new data processing methods and the realization of a standard for such measurements.

In this thesis, a simultaneous BTC & BTT measurement system was designed, realized and optimized using magnetoresistive sensing elements. A simultaneous BTC & BTT system ensures the measurement of the gap between the rotor blades and the casing and the measurement of blade vibrations. Different types of probes have been proposed and are currently used to monitor these parameters: optical, capacitive, microwave, eddy current. The sensors developed in this research project are based on the magnetoresistivity. Dedicated hardware and software components had to be designed and manufactured. Two external test at Fogale Nanotech in France and at the Military Research Institute of Technology (ITWL) in Poland are reported. The measurement chain was fully characterized and the innovative instrumentation for BTT and BTC measurements based on the magnetoresistivity has achieved promising performance for a professional product.

This work was realized in a collaboration between the “Centro di Ateneo di Studi e Attività Spaziali G.Colombo” – CISAS, Padova, Italy, the Engineering Department of the University of Perugia, Italy and the Von Karman Institute, Rhode Saint Genese, Belgium.

Summary

During the development of a new machine there are two fundamental aspects to take into account: the mechanical structure of the machine and its efficiency. A fundamental part of the design and the development of a rotating machinery is the determination of reliable and performing geometries. From a mechanical and structural point of view, the machine components must provide a certain life in safe conditions, for instance avoiding resonance phenomena in the working range of the machine. At the same time, the machine components must provide also an high efficiency. It is not the case that the perfect structural part it is also the most efficient, very often the definitive geometries of a turbomachine are a compromise between structural and efficiency requirements. In this scenario it is necessary to have a robust design process and numerical analysis of stress and strain levels, of the loads as well as the performance of the parts of the machine. Finally, it will be mandatory to have experimental validation sessions. Considering for instance an industrial gas turbine or aero-engines, it is fundamental that the rotor blades and disks will be accurately designed for a long life (fatigue life), safe working conditions far away from resonances and dangerous fluid-structure interactions and characterized by high efficiency. The design team and the aerothermal team must collaborate in designing and defining geometries that, *numerically*, will be reliable and that provide high energetic machine efficiency. Fundamental will be than the *experimental validation* of the prototypes, carried out in test benches properly equipped. This last part is realized using professional instrumentation to validate the prototypes and to certify their performance. In particular, concerning rotor blades and disks, the experimental test regards the monitoring and measurement of blade vibrations during operation and the running gaps between the blade tip and the casing, key parameter for an high aerodynamic efficiency. The instrumentation used can be with *contact* with the rotating parts or *contactless*. The latter are the so-called Blade Tip Timing (BTT) and Blade Tip Clearance (BTC) measurement systems.

The aim of this PhD thesis is the development of a BTT & BTC measurement chain based on new magnetoresistive sensors. This instrumentation is already commercially available and it is used in turbomachinery testing since years, but there is a continuous development in the frame of *new sensor technologies* and *data processing methods*.

During the first year of the PhD new magnetoresistive probes were designed and realized to provide simultaneous measurements of “blade tip gap” and “blade vibrations”. A dedicated electronic and software for the signal analysis had to be developed. The work started from preliminary test using the magnetoresistive sensing elements and carring-out the characterization at the passage of

ferromagnetic parts. Then, test benches were developed to deeply study the layout of the sensor and to analyse the signal to noise ratio at the blade passage. Once the probe geometry was defined, the first year ended with the realization of a dedicated electronic for the signal amplification and filtering and a software for the signal analysis.

The second year of the PhD was focused on the experimental characterization of the measurement chain and on the development of mathematical models. Once the instrumentation was completed, it was the time to characterize fundamental parameters like the rise time, uncertainty levels on blade tip gap measurements, definition of key parameter for the vibration measurements and the studies on the influence of external sources of errors. To extend the know-how, 2D and 3D mathematical models were realized to simulate operating conditions and for future developments.

The last part of this research work was the validation of the instrumentation, the optimization of hardware and software and comparisons with existing BTT and BTC instrumentation. In particular, once the whole measurement chain was realized and characterized, it was necessary to validate the instrumentation against some commercial and certified probes. For that reason, external test were performed in the test benches of Fogale Nanotech in France and in the second compressor stage of a real military jet-engine at the military research institute of technology (ITWL) in Poland. The results were very satisfactory and it was possible to improve the performance and the accuracy of the whole system.

Sommario

Nello sviluppo di un macchinario ci sono due aspetti fondamentali che devono sempre essere considerati: la meccanica della struttura e il suo rendimento. Una parte fondamentale della progettazione e sviluppo di una macchina rotante è la definizione di geometrie che siano affidabili e performanti allo stesso tempo. Da un punto di vista meccanico-strutturale, i componenti in movimento devono garantire una certa durata nel tempo rispettando dei margini di sicurezza, come operare in un regime lontano da risonanze e fenomeni dannosi. Se da un lato una certa geometria può soddisfare tali requisiti, dal punto di vista energetico il macchinario dovrà essere efficiente. Non è detto che il componente strutturalmente perfetto sia anche efficiente, anzi, molto spesso nella progettazione di una nuova turbomacchina, la versione definitiva prevede un compromesso fra i due aspetti. Tali esigenze richiedono un rigoroso metodo di progettazione e analisi numerica degli stati di tensione, delle sollecitazione e delle performance delle componenti del macchinario che dovranno poi, imprescindibilmente, essere validate sperimentalmente. Considerando ad esempio il caso di turbine a gas industriali o motori aeronautici, è fondamentale che i componenti della turbomacchina e, in particolare palette e dischi rotanti, siano correttamente dimensionati per una lunga vita a fatica, che in condizioni di lavoro si trovino ben lontani da risonanze e fenomeni di interazione fluido-struttura potenzialmente dannosi e che presentino alti rendimenti. Il team di progettisti strutturali insieme al team degli esperti di fluidodinamica dovranno così dimensionare e definire delle geometrie che, *numericamente,* siano strutturalmente affidabili e allo stesso tempo garantiscano un alto rendimento energetico della macchina. Fondamentale è poi la *validazione sperimentale* dei prototipi proposti, fatta su banchi prova opportunamente strumentati. Questa ultima parte è condotta utilizzando strumentazione professionale fine a validare i prototipi e certificarne le performance. In particolare, sempre con riferimento a palette e dischi rotanti, sperimentalmente vengono monitorate e misurate le vibrazioni delle pale in esercizio e il gap esistente tra la punta della pala e il casing, parametro chiave per un'alta efficienza aerodinamica. La strumentazione utilizzata può essere a *contatto* con le parti in moto, o di tipo *non a contatto*. In questo ultimo caso si parla di sistemi di misura Blade Tip Timing (BTT) e Blade Tip Clearance (BTC).

L'argomento di questa tesi di dottorato è lo sviluppo di una catena di misura BTT & BTC basata su nuove sonde magnetoresistive. Tale strumentazione già esiste ed è ampliamente usata nel settore delle turbomacchine, ma è in continuo aggiornamento sotto gli aspetti dello *sviluppo di nuovi sensori* e nuove *tecniche di analisi e processing dei dati*.

Durante il primo anno del corso di dottorato sono state progettate e realizzate le sonde analogiche magnetoresistive per misure simultanee di “blade tip gap” e “blade vibrations”. Elettronica dedicata e software di analisi del segnale sono stati sviluppati di conseguenza. Si è partiti da prove preliminari con gli elementi sensibili magnetoresistivi e loro caratterizzazione al passaggio di componenti ferromagnetiche. Si è poi sviluppato dei banchi prova per uno studio approfondito del layout del sensore e l’analisi del rapporto segnale rumore al passaggio di palette di turbomacchine. Definita la geometria della sonda e i suoi componenti, il primo anno si è concluso con la realizzazione dell’elettronica dedicata per l’amplificazione e filtraggio del segnale e il software per le misure a partire dall’analisi del segnale.

Il secondo anno di dottorato si è concentrato nella caratterizzazione sperimentale della catena di misura e nello sviluppo di modelli matematici. Completata la realizzazione della strumentazione, sono stati caratterizzati i parametri fondamentali quali rise time, incertezza in misure di blade tip gap, definizione dei parametri chiave per il calcolo delle vibrazioni e studio dell’influenza di sorgenti esterne di disturbo. Per completare il know-how sviluppato sono stati realizzati dei modelli matematici 2D e 3D per la simulazione delle prove sperimentali e per utilizzo in sviluppi futuri.

L’ultima parte del dottorato si è focalizzata sulla validazione della strumentazione, l’ottimizzazione delle componenti hardware e software e comparative con strumentazione esistente. In particolare, realizzata e caratterizzata l’intera catena di misura, è stato necessario validare la strumentazione con delle sonde commerciali professionali certificate. A tal fine, è stato possibile eseguire dei test su banco prova presso Fogale Nanotech, in Francia e sul secondo stadio di compressore di un motore aeronautico militare presso l’istituto di ricerca militare (ITWL) in Polonia. Risultati più che soddisfacenti hanno confermato la validità dei componenti sviluppati e dei modelli realizzati, consentendo di migliorare le performance generali e l’accuratezza di misura.

Contents

List of figures

1 Introduction

1.1 Background

The engines currently installed in aircrafts contain limited instrumentation for monitoring the engine condition in service. On line health monitoring sensors would allow improvements on safety and, at the same time, reduce whole life costs and maintenance requirements. However, the aero engines presents an extremely challenging environment for the application of reliable instrumentation.

The accurate control of running gaps between static and rotating components is vital to preserve mechanical integrity and ensure a correct functioning of any rotating machinery. In aero engines, tip leakage above the airfoil tip also results in relevant aerodynamic losses. One way to measure and monitor tip gap is by a Blade Tip Clearance (BTC) technique. The clearance variation occurs as a consequence of manufacturing and installation tolerances, vibrations, different expansion rates of blades, rotor disk and casing induced by thermal and speed transient [1].

The measurements of vibration and eigen frequencies is a crucial part of the development of any new gas turbine or aero-engine. All turbomachinery blades and components experience vibration during operation due to several sources like: unbalance, pressure distorsions, flutter, stall and surge. Unfortunately this undesirable structural motion affects fatigue life, performance and integrity [2]. For more than half a century, vibration measurement has been performed by installing strain gauges on the blades and using telemetry to transmit the signals. The Blade Tip Timing (BTT) technique, is currently being adopted by all manufacturers as a replacement for the classical strain gauge technique because of its non-intrusive character. The aim of the blade tip-timing measurement system is to evaluate the time at which a point on a rotating blade tip passes a stationary point. In the absence of any structural vibration, the blade arrival time would depend only on the rotational speed of the blade. On the other hand, when the tip of the blade is vibrating, the arrival time will depend on the amplitude, frequency and phase of vibration. Hence, the blade motion can, in theory, be determined from the arrival data.

Various types of sensors have been proposed for BTC and BTT systems including electromagnetic, magnetic, inductive, optical, capacitance, eddy currents and microwave [3]. The engines present an extremely challenging environment for the application of these monitoring sensors but still now, no one reliable and accurate in service system exist.

There are several requirements that such an instrumentation should satisfy to be used in a modern engine: small sensor size, freedom from geometry sensitivity, measure of the real clearance (casing - blade tip), tolerance to debris, suitable for high temperature measurements, reliable, long life [4]. About 10 years ago, Von Flotow [5] reports a list of patents filed by various developers of blade tip sensing systems, this demonstrates the level of interest and activities in that field.

The aim of this project was to develop and test a new sensor for clearance and vibration measurements in turbomachines, based on magnetoresistive sensing elements. This research work started from the consolidate experience and the state of the art on non-intrusive measurement systems developed by the research groups of the Universities of Perugia and Ancona, in collaboration with important turbomachine manufacturers like the ex-Nuovo Pignone. In fact, Prof. E.P. Tomasini, prof G. Rossi, prof. N. Paone and the Engineer P. Nava have been working on this topic since the first 90s' [65-66]. Beside that, couple of years before this research project has started, the University of Perugia was already testing the digital magnetoresistive sensors [67].

1.2 Literature review

The literature survey has started from the VKI LS on Tip Timing and Tip Clearance problems in turbomachines [6]. Then, some information on vibration and clearance effects were gathered from the library. Starting from the VKI LS several references about BTT and BTC application systems were found, mainly collecting the most important, interesting and some recent publications with different sensor technologies. Improvements and new publications from authors were also collected. The next step was performed searching for BTT data analysis methods. It was not easy to find information on this topic because of confidentiality issues. Finally the last part of the bibliographic research was focused on the magnetoresistive sensing elements and related applications, with particular attention to the aero engine.

1.2.1 BTC and BTT measurement systems

Various kind of sensors have been proposed to measure the gap between blade tip and casing as well as blade vibrations. Chana in [3] gives an overview of the main type of sensors: optical, capacitance, eddy current, microwave and pressure. Optical probes are largely used for blade tip timing thanks to the fast response achievable and very small spot size. Cardwell [7] used an optical system to compare the result with an eddy current sensor. Gallego [8] and Heath [9] used optical systems to validate a new timing technique. Moreover, optical probes were also used for blade tip

clearance as reported by Dhadwal et. al [10] and Pfister [11]. Zielinski [12] reports a capacitance based tip timing system for crack detection on an industrial gas turbine. He made a comparison between the result of capacitance sensors and reliable data from strain gauges. A recent work at VKI with the same type of sensor was made by Lavagnoli et al [13]. They reported that blade tip-casing gap can be measured within 25 μm (20:1) at a working distance of 1 mm. General Dynamics Advanced Technology Systems [14] have patented a three coil differential and shielded eddy current sensor for tip timing. Chana [7] has recently developed and tested eddy current sensors on an aero engine. Tests have been performed using sensors mounted on Rolls-Royce and QuinetiQ facilities. Grzybowski [15] and Maslovskiy [16] presented a system based on microwave sensors for clearance measurements. The same type of probe was also used by Wagner et. al [17] for vibration measurements. Detailed measurements of the pressure field on the casing of a turbo-machine can also potentially provide information about the tip clearance and tip timing. Belsterling [18] in 1971 suggested using a non-contact pressure measurement method for determining blade tip gap and displacement.

1.2.2 Measurements without holes

Measurements done through the casing wall without making holes in it would be very advantageous. Some interesting articles related to this topic have been found. Rickman [19] reported in 1982 the use of a commercially available eddy current sensor to measure blade speed through the casing of a diesel engine's turbocharger for use as a fault detector. More recently, Von Flotow et al. [20] tested the response of an eddy current sensor through different shielding materials in the thickness range below 2mm. They reported that titanium and stainless steel did not affect the sensor significantly while aluminum reduces the signal by approximately half. Finally, also Chana [7] confirmed the possibility to measure through different shielding materials with the same kind of sensor, obtaining an acceptable signal attenuation for a few mm thickness.

1.2.3 Blade Tip Timing Data Processing

Tip timing measurements consist of three steps as follows:

1. Data acquisition: the acquisition of blade time of arrival data from a number of probes mounted around the casing
2. Data postprocessing: the derivation of characteristic vibration parameters such as blade displacement from the measured data

3. Data analysis: the analysis of the sampled blade tip deflection to retrieve the vibration properties of the rotating assembly

Data postprocessing consists first in identifying surplus or missing blade readings in the data file and to correct it. Then to process the timing information into blade displacements. Details are given by Gallego [8, 21] and Carrington [22]. Finally, the step 3 is crucial as it provides important information about the dynamic behavior of the assembly. In this project, a methodology based on the cross-correlation function has been developed to process the tip-timing data. Further detail will be given in this report and can also be found in previous work by Prof. Gianluca Rossi, during his PhD Thesis [23]. A number of methods have been proposed in literature like the single parameter technique developed by Zablotskiy and Korostelev [24], the two-parameter plot method (Heath et al [25, 26]), the technique by Zielinski and Ziller [27] ,and various autoregressive methods (Dimitriadis et al. [28], Carrington et al. [29], Gallego [30], Gallego and Dimitriadis [31]). The processing is further complicated when two or more modes of vibration exist simultaneously. This is not an uncommon event and has been repeatedly reported in the literature regarding aeroengine vibration problems since the early investigations of Armstrong and Stevenson [32]. Autoregressive-based methods and the two-parameter plot method have been shown to fail when two simultaneous synchronous resonances from simulated BTT data are analysed (Gallego [30]). Robinson [33, 34] reported the existence at Pratt and Whitney of techniques for decoupling two simultaneously occurring synchronous modes. This vibration condition is also referred to (Jones [35] , Hayes et al. [36]). However, no description of the methodology is given by the mentioned authors. Also Gallego presents some methods for the analysis of BTT data from assemblies undergoing two simultaneous resonances [37]. Having a rotor blade vibrating at two modes and considering the displacement of the tip as a linear superposition of two undamped sinusoids, it is possible to determine the autoregressive coefficients. Than, the frequencies of vibration can be recovered. The linear autoregressive model requests the rotational speed of the rotor to be constant or varying very slowly in the period of the computation. This method can be used both for data acquired in one revolution or in multiple revolutions. In the latter case the method has been called MGARES. After an intensive experimental validation of the proposed methods, Gallego [8] recommended MGARES as the method for the analysis of BTT data from assemblies undergoing single and multiple simultaneous resonances.

1.3 Objective of the research project

The specific objectives of this research work derive from the intention of designing and realizing a BTC and BTT measurement system based on new magnetoresistive sensing elements. These objectives can be summarized as:

1. design and realization of a new probe;
2. development of dedicated hardware and software components;
3. characterization and experimental investigations of the whole instrumentation chain ;
4. comparisons and validations with existing systems.

1.4 Structure of the thesis

The work reported in this thesis has been divided into eight sections.

Chapter 2 introduces the theory of vibration in rotating components. Particular attention is given to blade and disk vibration modes. Finally, the phenomenon of blade tip clearance variation is described.

Chapter 3 explains the principle on which a Tip-Timing and Tip Clearance system works.

The design, development and realization phases of the measurement system are reported in chapter 4.

Chapter 5 and 6 focus on experimental measurements of tip-clearance and tip-timing. The characterization of the sensor for clearance measurements and its calibration curve is illustrated. Blade vibrations were simulated and measured on test benches and real turbomachines.

Some aspects of the whole measurement chain were improved during this work. Chapter 7 summarizes the main developments.

Finally, conclusions from this research project are drawn in Chapter 8. The main features and performances are summarized. The thesis ends with recommendations for future work.

2 Fundamentals of blade vibration and blade tip clearance problems in turbomachinery

2.1 Introduction

High cycle fatigue of blades due to dynamic loading during vibration is the main cause of engine failures. Understanding the mechanism of these vibrations forms an essential basis for a designer to avoid a design operating with dangerous vibrations. This chapter goes stepwise through the possible vibrations of a bladed disk. First the blade and disk vibrations are explained separately, finally the combination of both vibrations is handled. The chapter ends with an overview on blade tip gap variation problems.

2.2 Blade modes

2.2.1 Classification of blade modes

Vibrations take place in the neighbourhood of certain frequencies, called eigenfrequencies, which are typical for the vibrating object. Each eigenfrequency has a characteristic mode shape (= eigenmode). This is the shape of the vibrational pattern. Mode shapes of a blade are typically divided into four families, [38]: flap wise bending (F), edgewise bending (E), torsional bending (T) and an axial mode (A).

Since blades usually have a very complex shape, it is common to investigate their vibratory properties using three simplified models according to their geometric characteristics such as length, thickness and chord, [38]:

(a) If the length-to-chord aspect ratio (=Length/Chord) is high (larger than 5) and the thickness is small compared to the length, then the blade is considered as a uni-dimensional structure and modelled as a beam.

(b) If the length-to-chord aspect ratio is low and the thickness is still small compared to the other dimensions, then the blade is considered as a two dimensional structure and modelled as a thin plate or shell.

(c) If the blade has a low length-to-chord aspect ratio and is considered as being thick, then it is a three-dimensional structure. In this case, the blade is modelled as a thick shell.

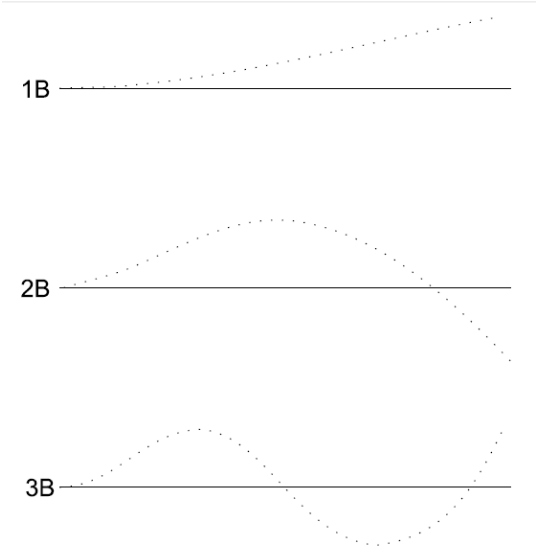

Figure 2.1 First 3 bending modes of beam with one end fixed and one end free

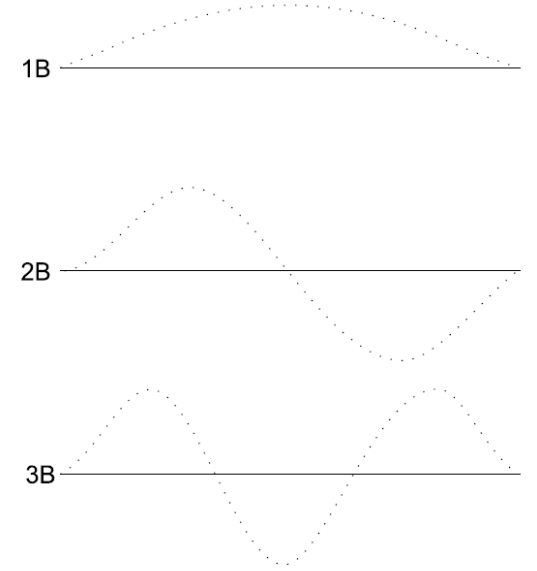

Figure 2.2 First 3 bending modes of beam with both ends fixed

The simple beam model (a) has the simplest vibration characteristics. Let's consider two beams with different end conditions that can correspond to the situation of a realistic blade. The first beam has a clamped and a free end, which corresponds to an unshrouded blade. The other beam is clamped at both ends and represents a shrouded blade. Figures 2.1 and 2.2 represent their first three bending modes. Notice the points with no deflection, they are called "nodal points".

The mode shapes of thin and thick shells are more complex, because the motions can take place in three dimensions. Figure 2.3 depicts the mode shapes of the first flap wise, edgewise and torsional bending mode. Even more complex mode shapes are formed when two or more modes appear

simultaneously. It is clear that determining the type of mode shape (especially complex ones), is not an easy task.

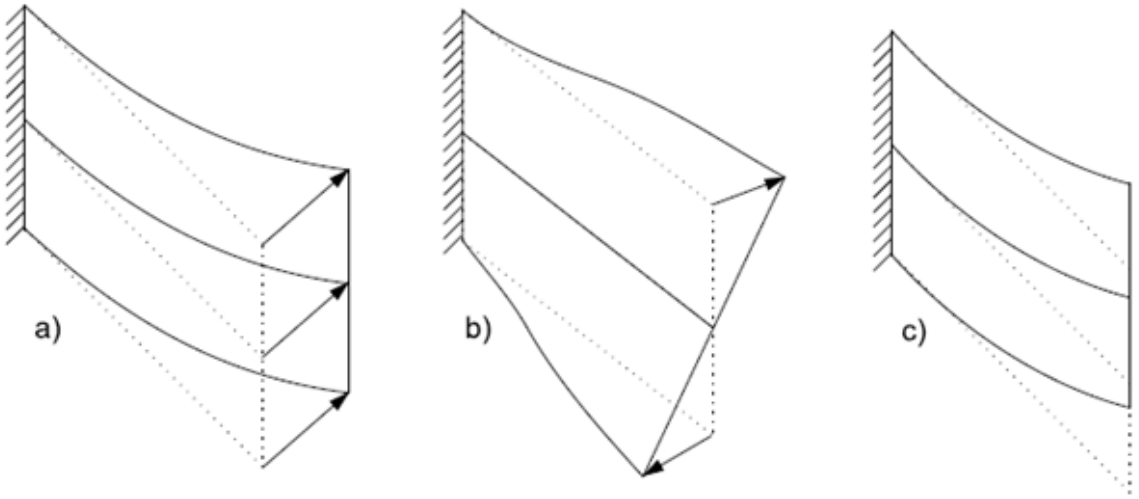

Figure 2.3 Mode shapes of cantilevered thin shells a) First flap wise bending mode; b) First torsional mode ; c) First edgewise bending mode

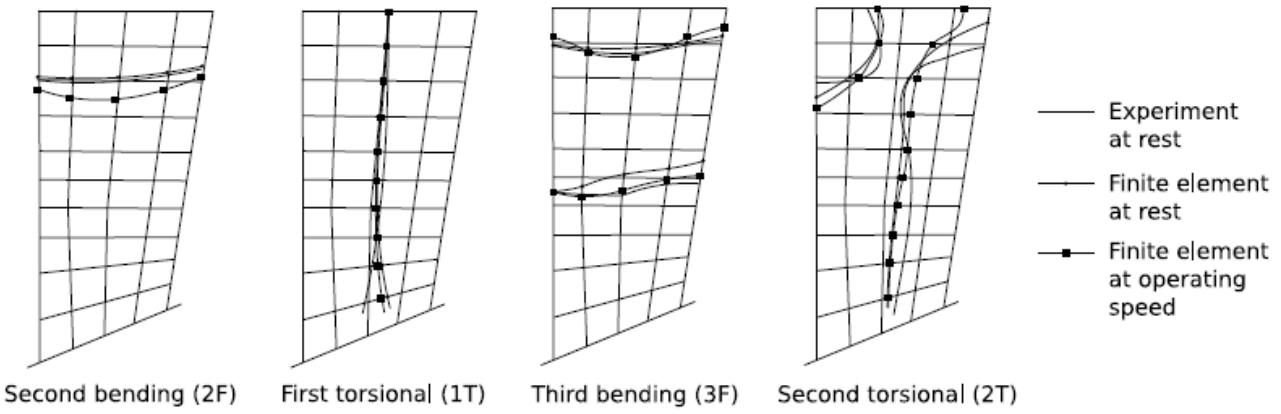

Figure 2.4 Nodal lines of modes shapes from cantilevered blades

Specifying nodal lines is generally found as the most convenient way to describe mode shapes. These lines represent points which have no displacement during vibration, see figure 2.4. When investigating the vibratory behaviour of a blade, it is always useful to look first at the nodal lines. They give quick information about the mode shape and the places where strong deflections are expected. Figure 2.5 is an example of mode shape classification from a cantilevered blade by means of the nodal lines, [39]. Two types of nodal lines are indicated. The horizontal lines represent m radial directed nodal lines and the vertical lines are n axially or tangentially directed nodal lines.

Note that in all shown cases, a vertical nodal line lies on the line where the blade is fixed to the hub. The blades in the first and the third column (m=0 and m=2) are vibrating in bending modes. The middle column (m=1) has blades that are subjected to a torsional mode.

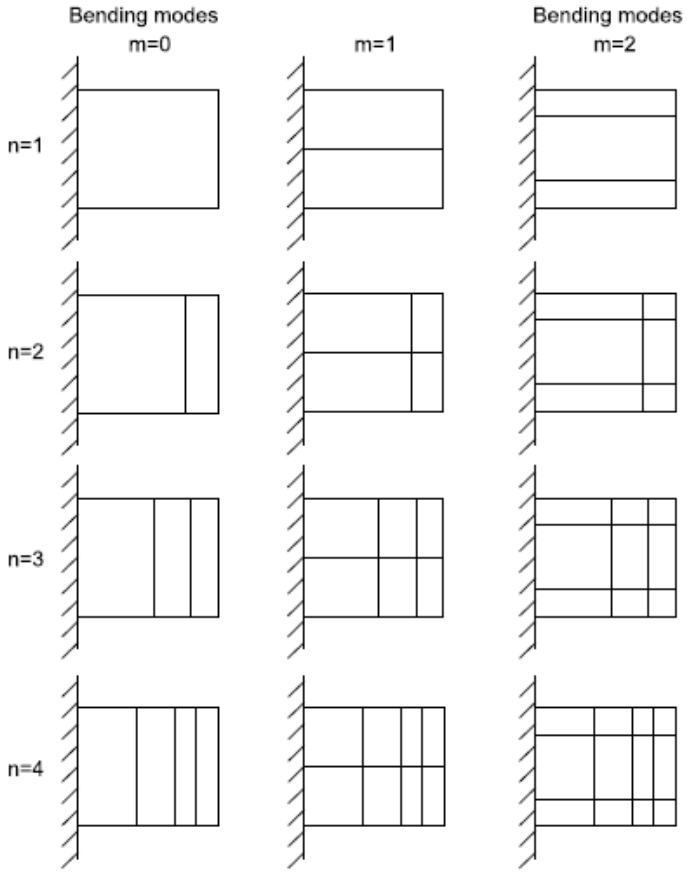

Figure 2.5 Mode shape classification of a cantilevered blade

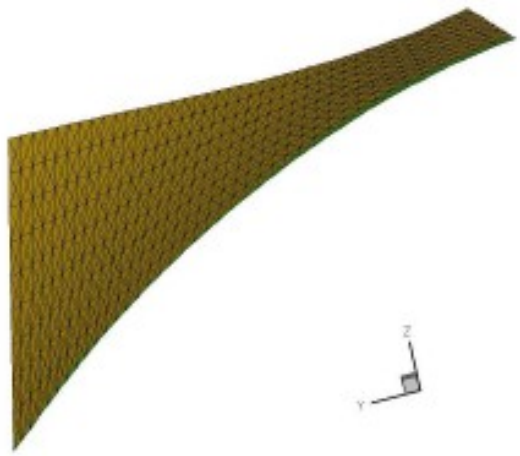

Figure 2.6 Non-vibrating radial compressor blade

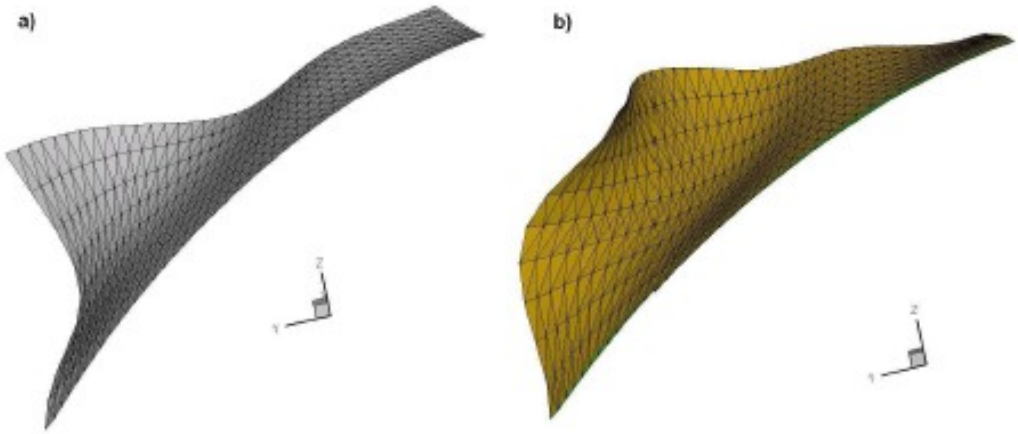

Figure 2.7 Two vibrating modes of a radial compressor blade

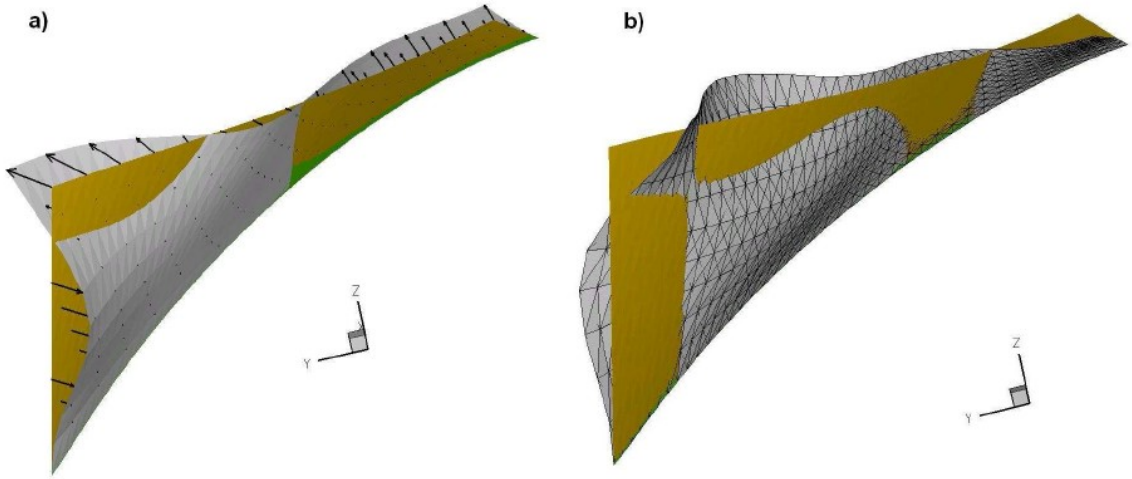

Figure 2.8 Two vibrating modes of a radial compressor blade with nodal line indication

The strength of this method can be illustrated by analysing the complex mode shapes of a non-rotating radial compressor blade. The hub is simulated by applying fixed boundary conditions on the blade's root. Finally, the mode shapes are obtained with a Finite Element Program. Figure 2.6 illustrates the non-vibrating blade, whereas two mode shapes (without nodal lines) are given by figure 2.7a and b. In figure 2.8, nodal lines are formed by the intersections of the blade at rest and at a vibrating condition. The nodal lines clearly indicate the (m,n) parameters of the modes. Figure 2.8a with (m,n) = (1,2) is a torsional mode. Figure 2.8b with (m,n) = (3,2) is a bending mode.The blades in figures 2.6, 2.7 and 2.8 are modelled as thick shells. A step closer towards real blades would be a model that uses tetrahedral blocks. This 3D model type seriously increases the computational time for finding eigenfrequencies and modes, but reaches a higher accuracy. In most cases (simple blade shapes) the gain in accuracy is not worth the larger computational time

compared to the previous presented models. On the other hand, since blade failures are mostly caused by metal fatigue due to vibrations, it remains very important to predict them as accurate as possible.

2.2.2 Parameters affecting the blade mode properties

The effect of the blade shape:

- Taper affects the values of the eigenfrequencies but doesn't change anything to the mode shapes. There is though a difference between tapering the chord or the thickness, see figure 2.9. A decrease in chord gives an increase in both bending and torsional mode frequencies. Giving taper to the thickness (decreasing the thickness) results into, [39]:

• An increase of the first bending frequency

• A decrease in frequency for all other higher bending modes

• A decrease in frequency for all torsional modes

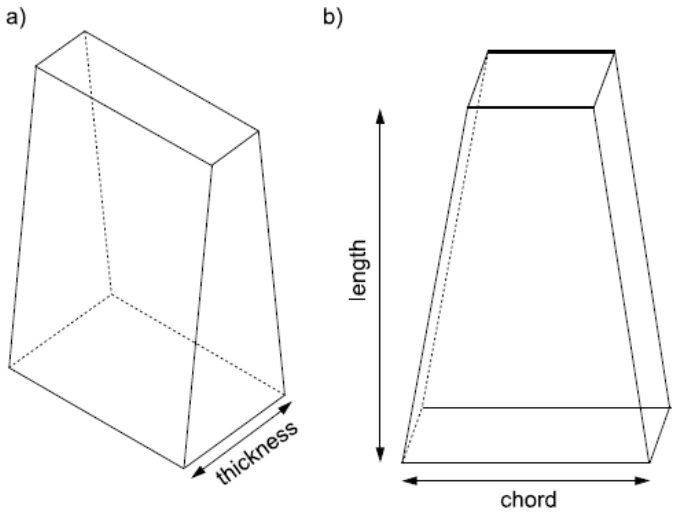

Figure 2.9 Taper of blades in a) thickness and b) chord

- Adding twist appears to have the opposite influence, namely same eigenfrequencies and different mode shapes for the bending modes. The latter is caused by combinations of blade modes that interact. Giving more complexity to a blade increases the chance that different mode shapes will influence each other. As the pre-twist increases, the blade's torsional stiffness increases. Therefore, torsional frequencies will increase with increasing pre-twist angle, [39].

- All blade vibration frequencies appear to increase almost linearly with increasing blade thickness, [40].

- A centrifugal compressor blade outlet angle has great influence on the mechanical and dynamic characteristic of a blade. When decreasing the outlet angle from 60 down to 0° (backswept blades, where 0° is a radial directed blade), the stress due to centrifugal force in the blade outlet part at the hub diminishes with 40%, see figure 2.10, [41].

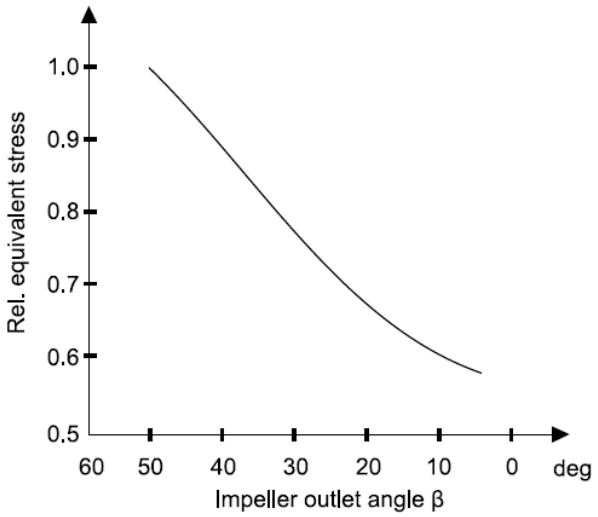

Figure 2.10 Equivalent stress in blade outlet part at hub due to centrifugal forces

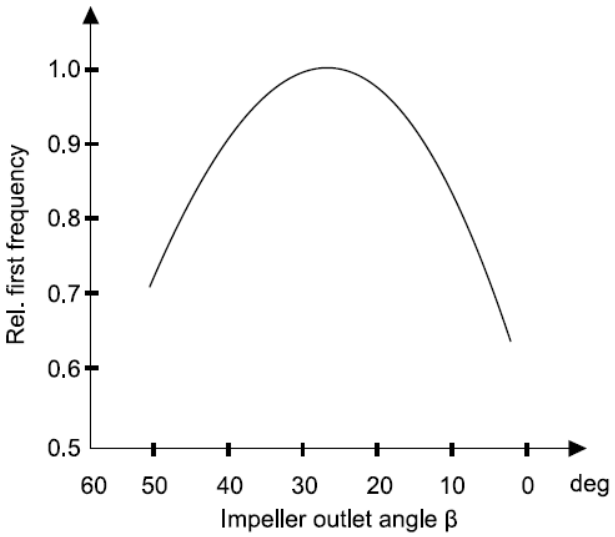

Figure 2.11 First bending frequency of a blade as function of the blade impeller

- The influence of the blade outlet angle on the dynamic behaviour of a centrifugal compressor blade is shown in figure 2.11. Stiffening of the structure for the first bending mode is indicated by

the change in eigenfrequency. The example in figure 2.11 achieves a maximum stiffness at approximately 30°, [41].

The effect of operating conditions, [38]:

- Rotating blades are submitted to a centrifugal force. Large twisted blades can suffer from a change in their geometry due to this force. However, the most important influence of the centrifugal force is a stiffening of the blades. This causes in turn an increase of the natural frequencies with some corresponding changes in the mode shapes. In figure 2.12 the basic feature of centrifugal stiffening is shown by a centrifugal force Fc pulling at the non-vibrating blades. When a blade starts to vibrate, it's gravitational point will move due to the blade's motion. This shift causes Fc to create a moment around the blade's root. One can see that the centrifugal force stabilizes vibrations normal to the rotation plane (2.12 b), because the moment counteracts the motions. Vibrations in the rotation plane (2.12 a) have an additional destabilizing moment. This is due to the changing direction of Fc, during the blade's motion, which creates a small force component in the same direction as the motion of the vibrating blade.

- Next to the stiffening effect due to the centrifugal force, is the de-stiffening effect (= a lowering of the eigenfrequencies) due to a temperature increase. Since the temperature, of a fluid passing a blade, usually increases with increasing operating speed, it is possible that both effects will compensate each other. This is certainly the case for high pressure compressors and low pressure turbines. In case of a high pressure turbine and a low pressure compressor, respectively the thermal and rotation effect will dominate. This behaviour is strongly dependent on the blade material properties.

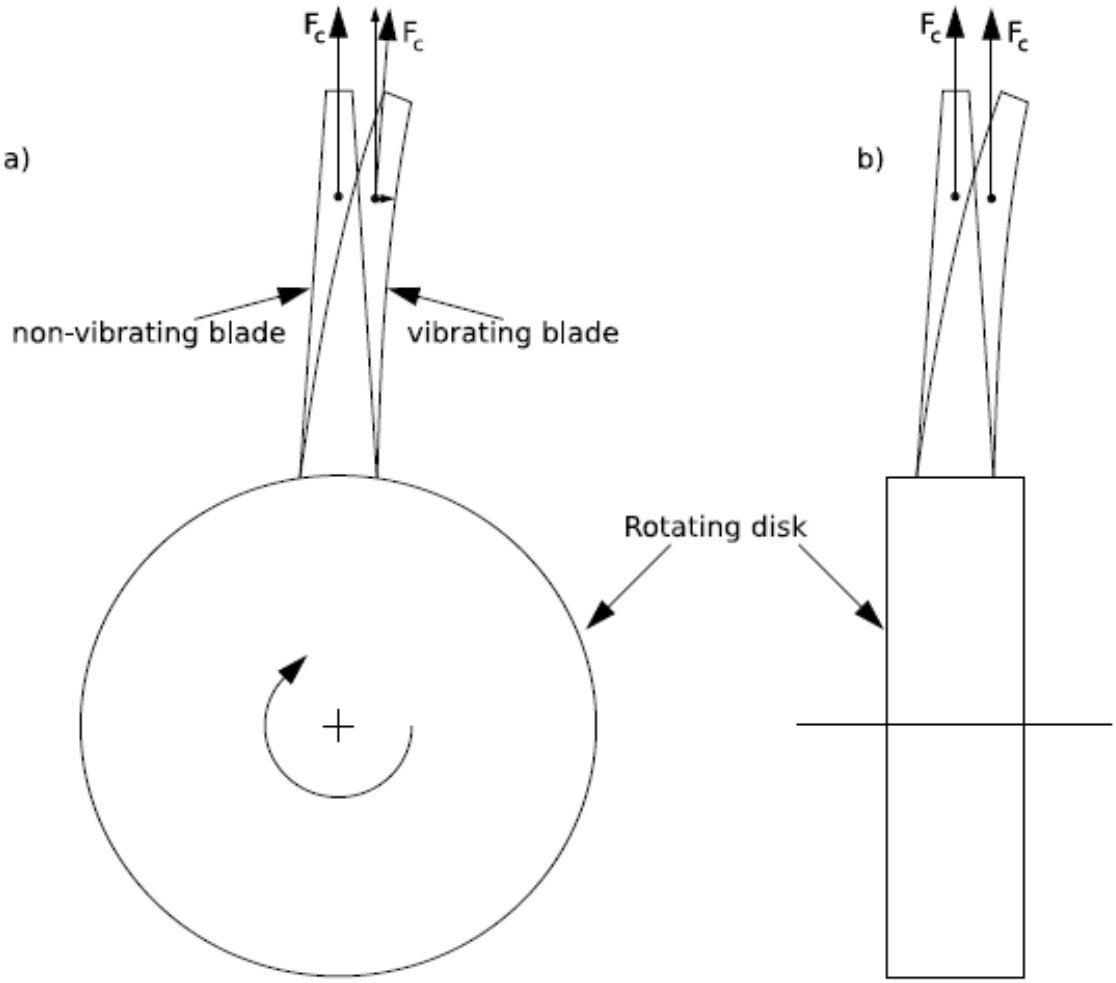

Figure 2.12 Centrifugal stiffening: a) tangential vibration; b) axial vibration

2.3 Disk modes

A disk has, similar to blades, eigenmodes and eigenfrequencies. The vibration of a disk is characterised by circumferential and radial sinusoidal displacements on respectively concentric circles and radial lines. The nodal points of these displacements form respectively nodal diameters (ND) and nodal circles (NC). The disk motions for modes ranging from 0 up to 3 ND (with 1 NC on the circumference) are depicted in figure 2.13 a. Figure 2.13b shows the displacements for 1 up to 4 NC modes without nodal diameters. Combinations of nodal diameters and nodal circles result in complex shapes as depicted in figure 2.14, [42]. These sinusoidal patterns are possible in axial, radial and tangential direction, see figure 2.15, [43].

Generally, when the frequency goes up, the number of nodal diameters (and circles) increases. Nodal diameter modes are grouped into families, where each family is characterized by a mode shape (axial, tangential or radial) with one specific number of nodal circles. Figure 2.16 shows the eigenfrequency behaviour from three families (0 NC, 1 NC and 2 NC) having the same mode shape.

It is common to present the response of diametral modes (no NC) on concentric circles. The disk rim, which has the largest displacements, is most suited for this purpose, see figure 2.17.

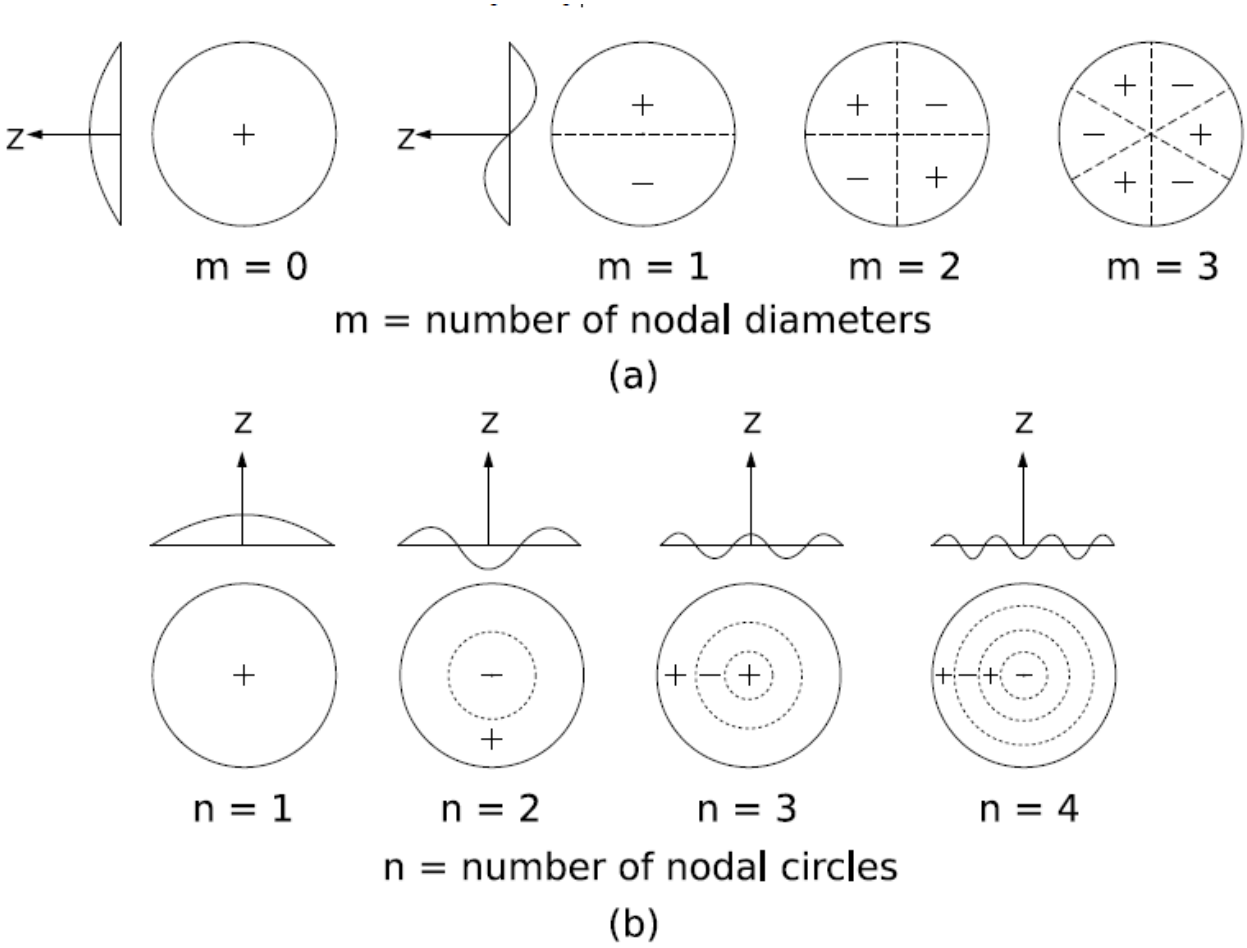

Figure 2.13 Deformation of disk with a) only ND(1 NC) and b) only NC

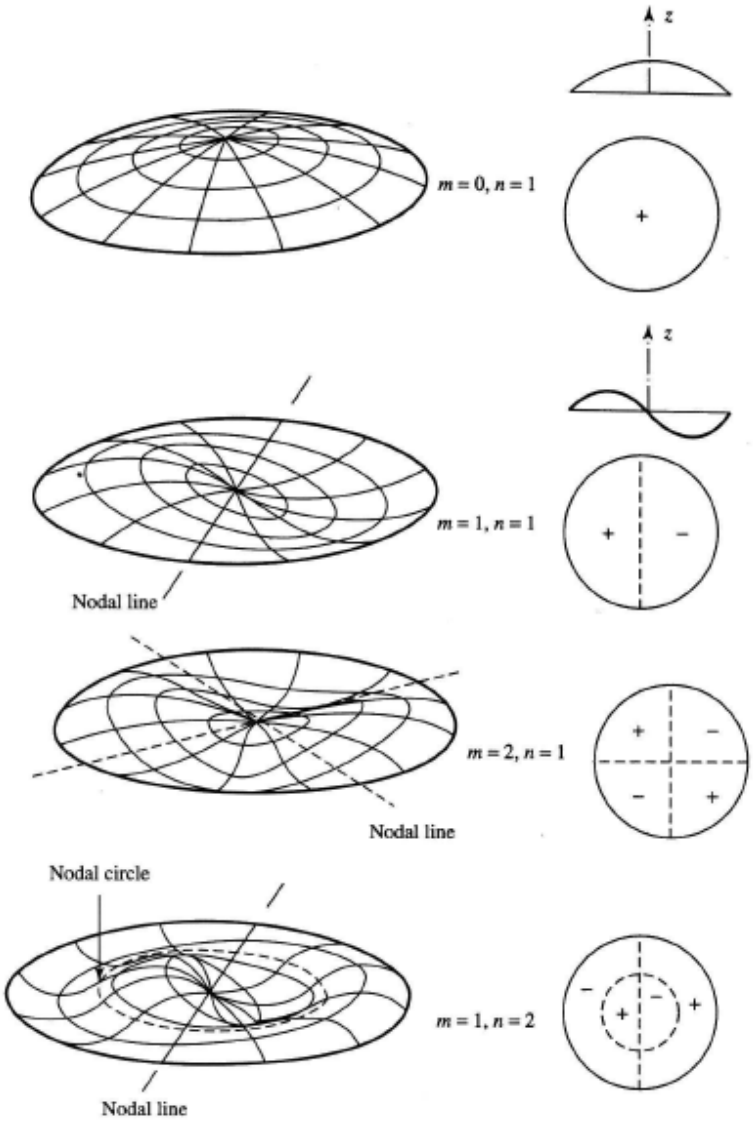

Figure 2.14 Axial deformations of a disk with m = number of ND and n = number of NC

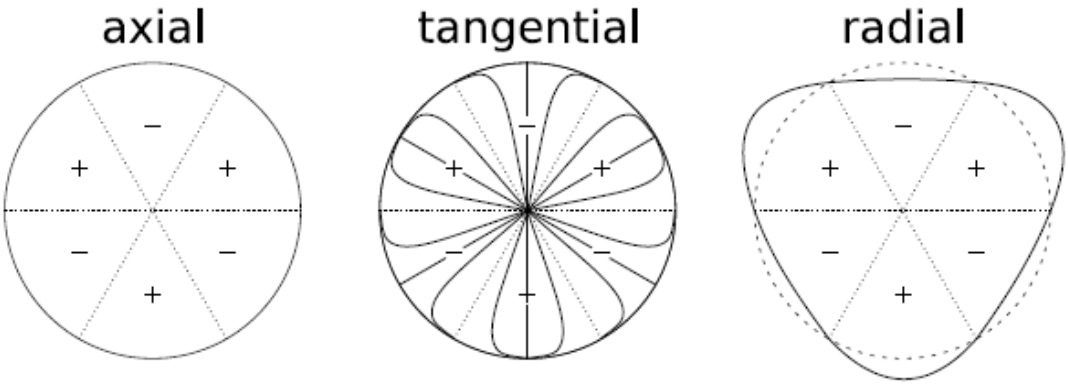

Figure 2.15 Disk vibrations

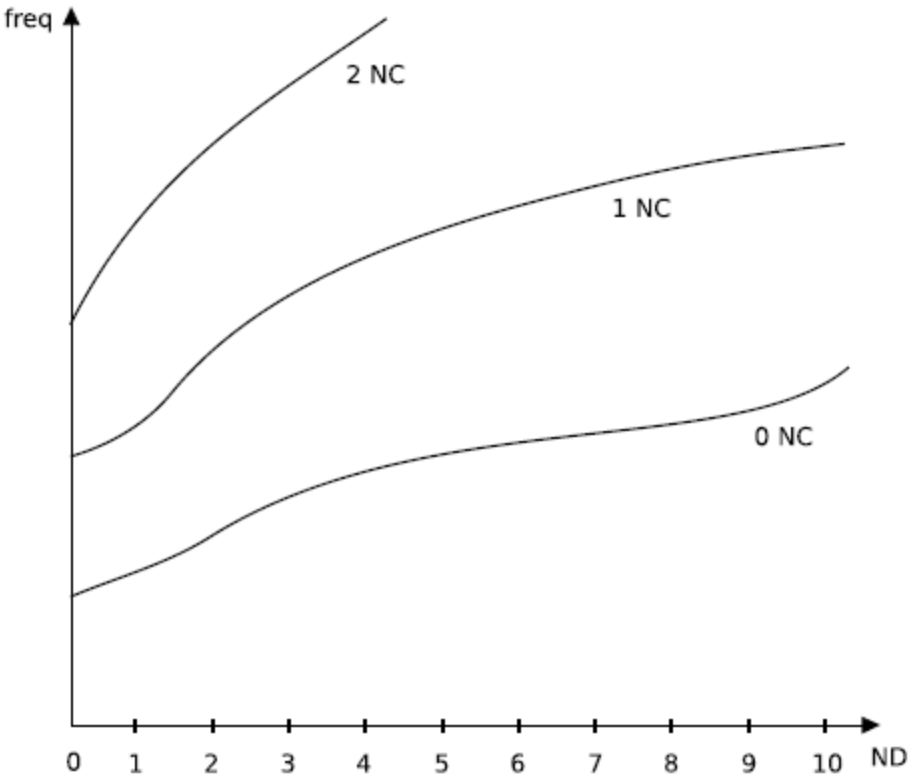

Figure 2.16 Families of a disk mode

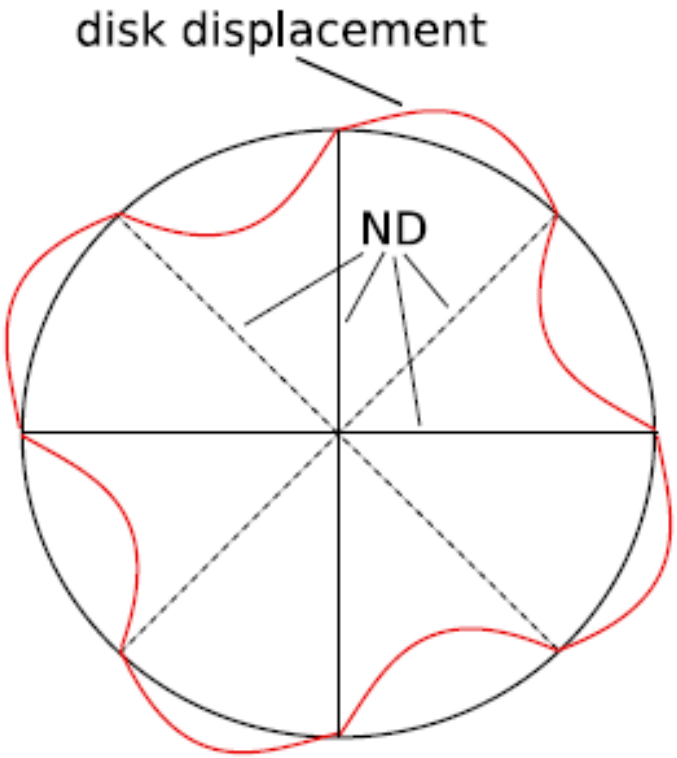

Figure 2.17 Presentation of 4 ND mode with displacements in axial direction

2.4 Bladed disk modes

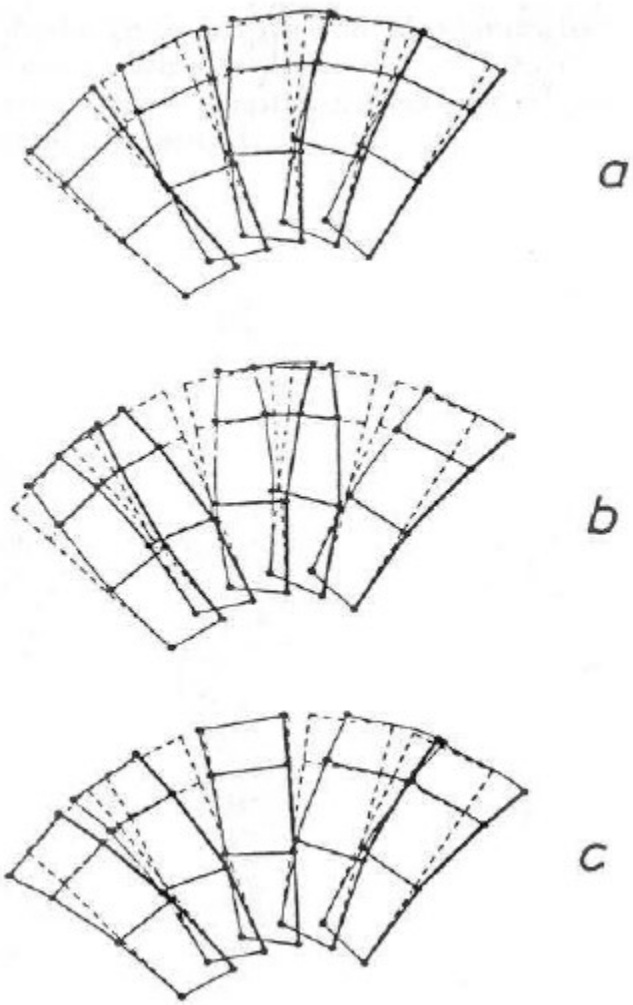

Figure 2.18 First bending modes of blades coupled through a disk: a) in-phase vibration; b) counter current vibration; c) one blade at rest

When combining the blades with a disk into a bladed disk, vibrations of both components must be taken into consideration, [44]. Because all blades are connected to each other through the disk and optionally a shroud, a coupling between the blades will exist. This blade coupling creates bladed disk modes which are characterized by the motions of the blades relative to each other. At a given moment, all blades will have the same mode shape but with different amplitude, see figure 2.18. Nodal diameters and circles are also used to categorize bladed disk modes. For instance, the first tangential blade bending mode (= 1T) is possible on a bladed disk for several numbers of nodal diameters. One can group these blade coupling modes together into one family. On their turn, each family has a specific number of nodal circles. This means that many families are possible for, in this case the first tangential blade bending mode. For instance, the 3 different modes, although the

blades have the same mode shape, of the bladed disk in figure 2.18 are part of one family if they all occur with the same number of nodal circles. Considering the modes within one family: With 0 nodal diameters all blades are moving in phase, but starting from 1 nodal diameter the blade amplitudes follow a sinusoidal pattern. The points of no displacement (where the sinus is zero) are on a nodal diameter. When a nodal diameter lies on a blade, then the amplitude of its blade mode is zero (the entire blade is at rest). If a nodal diameter would lie in between two blades, then both blades will have an opposite sign for the amplitude of their mode shape. For a bladed disk with an even number of N blades there can be maximum N/2 nodal diameters, if N is odd the maximum is (N-1)/2. Higher numbers of nodal diameters are possible but they are indistinguishable. An example of a 36 bladed disk, where the 4^{th} and 32^{nd} diametral patterns are indistinguishable, is given in figure 2.19. Note that the dots in this figure indicate the position of the blades at a certain moment, thus at every moment the position of the blades for a 4 ND pattern is the same as for a 32 ND pattern. Although the 32 ND sinusoidal pattern has a higher frequency then the 4 ND pattern, the blades experience a vibration as would it be a 4 ND pattern at an eigenfrequency of the 4 ND pattern.

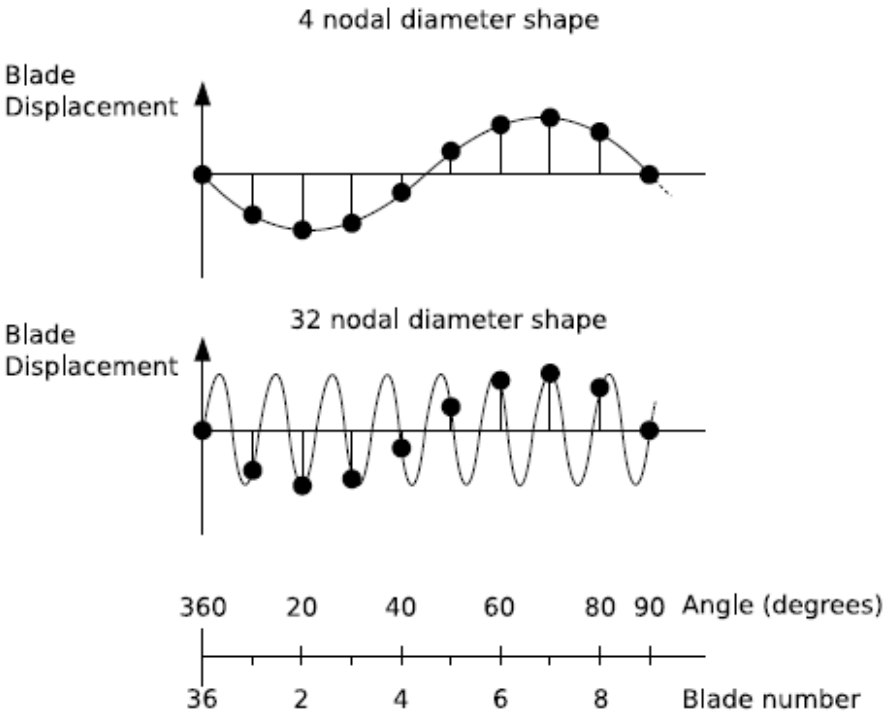

Figure 2.19 Indistinguishable 4th and 32nd nodal diameter pattern of a 36 bladed disk

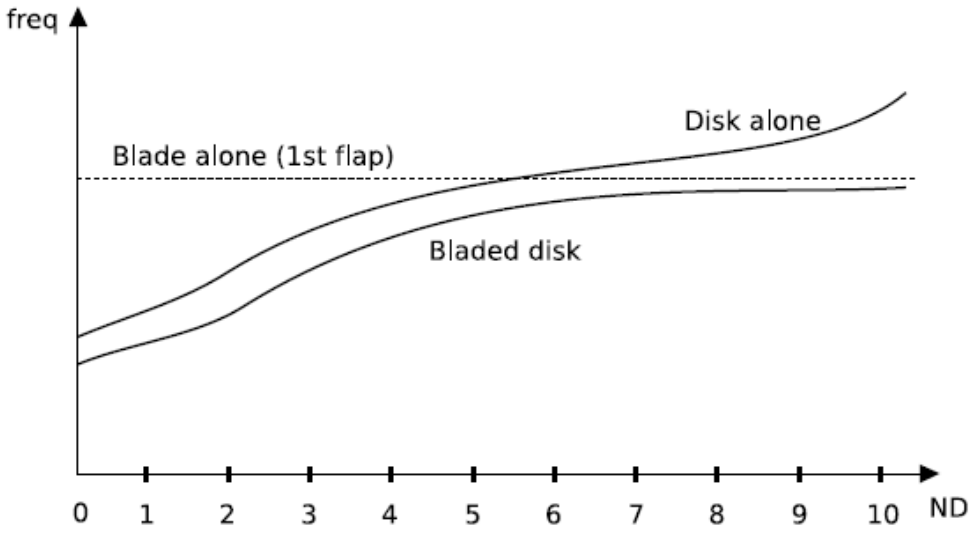

Figure 2.20 Disk stiffening effect caused by increasing number of nodal diameters

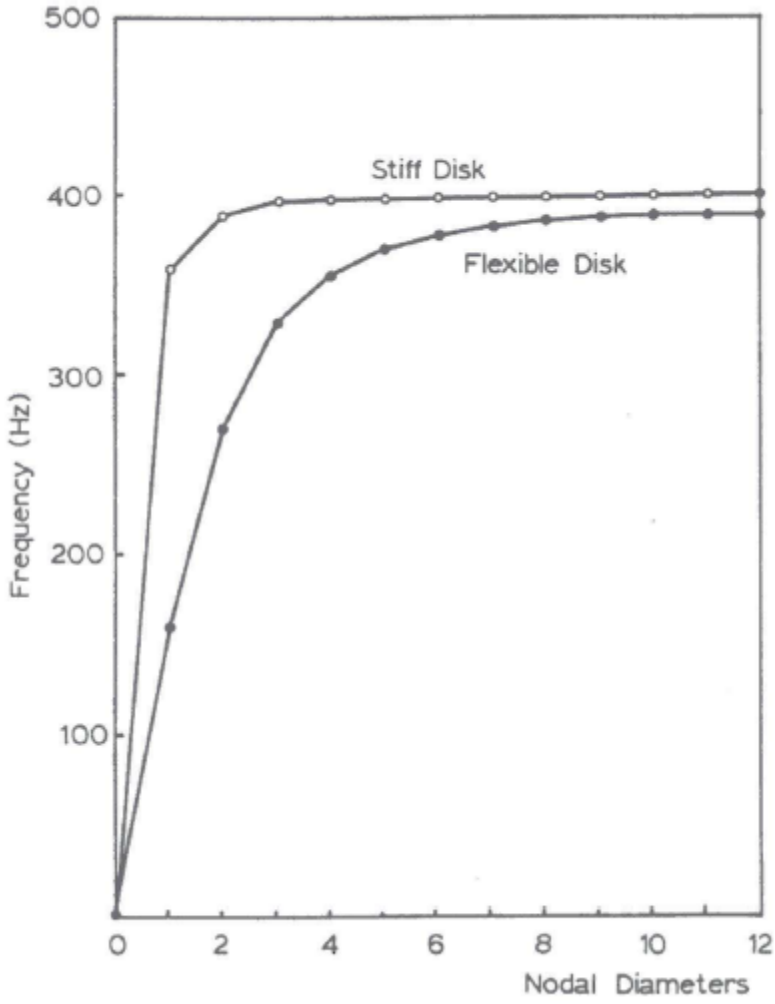

Figure 2.21 Effect of disk stiffeness on the bladed disk modes

Generally, the number of nodal diameters increases with increasing frequency within one family. The only exception is the 0 nodal diameter mode which is in most cases harder to achieve than the 1 and 2 nodal diameter patterns and therefore has a higher frequency. Important to notice, as the number of nodal diameters increases (up to N/2 for N even), the natural frequency in each family approaches one of the cantilevered blade frequencies, see figure 2.20. The latter is the natural frequency of a single blade with one root fixed in case of an unshrouded disk. This behaviour is caused by the progressive stiffening of the disk as it adopts more complex shapes (= more nodal diameters). In case of a very stiff disk, the coupling between the blades is very low, so the natural frequencies are very close, even at small numbers of nodal diameters, to the blade alone frequencies. The stiffness effect is illustrated in figure 2.21. An increase in number of nodal circles will also make the disk stiffer. This stiffening has the same influence as the increase in nodal diameters, but it will additionally cause these families (starting from the first nodal circle) to occur at higher frequencies. There is a very important difference in handling a bladed disk, where blades and disk have or don't have comparable stiffness. In case they do, there will be a strong blade coupling and a dynamic analysis of the whole disk is necessary to provide accurate estimates of the natural frequencies and mode shapes. However, when a disk is very stiff compared to his blades, it's influence can be disregarded and a dynamic analysis of a single blade is sufficient, because only the blades are vibrating.

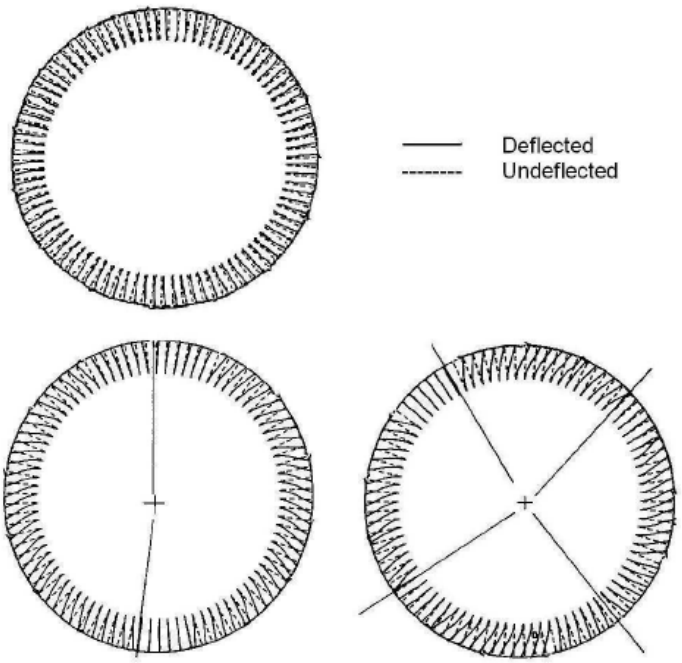

Figure 2.22 Nodal diameters in bladed disk with 6 blades in each disk sector

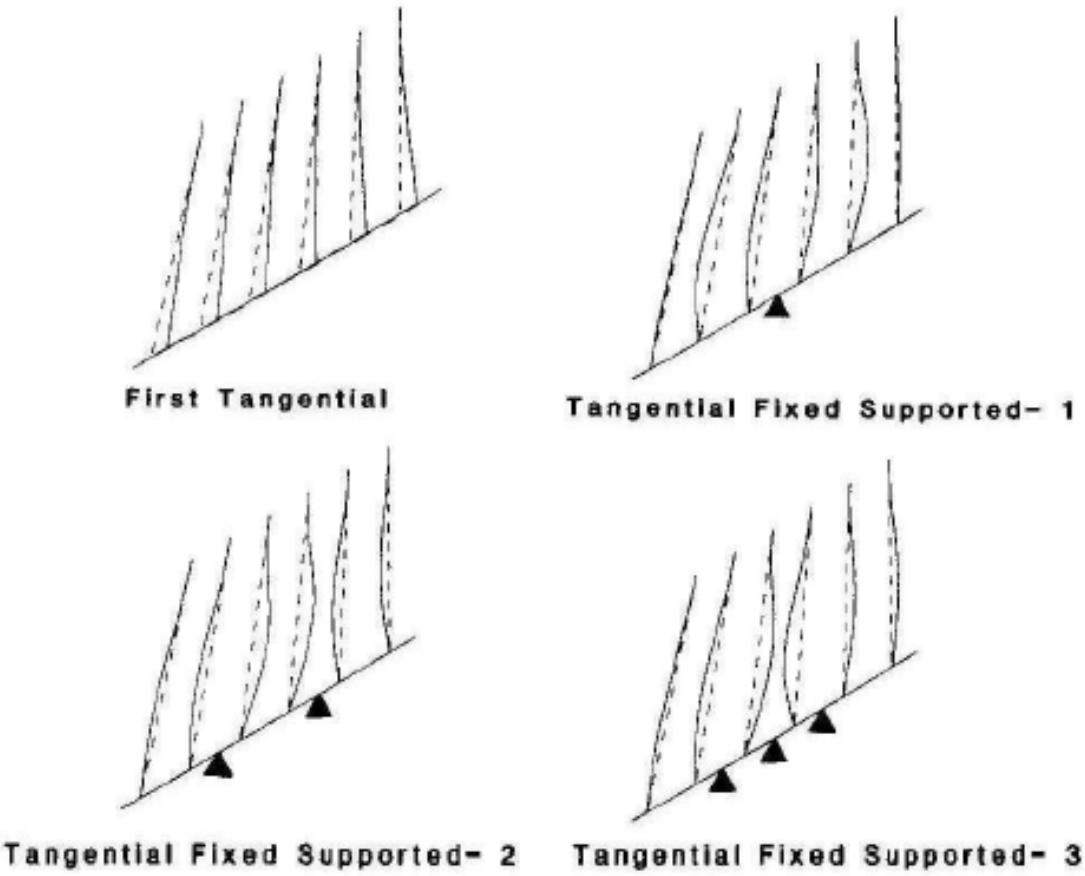

Figure 2.23 Mode shapes of one disk sector where a black arrow denotes the position of a nodal diameter

When blades are grouped into sectors, for example six blades in one sector, the vibrational character of the bladed disk is even more difficult to evaluate, [45]. Figure 2.22 illustrates bladed disks, where each blade belongs to a sector of 6 blades. As long as the nodal diameters lie in between adjacent sectors, all blades have the same displacements within each sector, see figure 2.22. When a nodal diameter intersects a sector, new modes are created within this sector. Different modes for an individual sector are shown in figure 2.23. All blades are vibrating with the same blade mode, but as one or more nodal diameters (indicated with black triangle) intersect a sector, the amplitudes of the blade modes are changed.

Single and double modes:

Each circumferential symmetric bladed assembly has certain well defined types of vibration modes. The most important feature is the existence of two mode types in one family, namely single and double modes. The latter one is the most common. A double mode consists actually of two orthogonal harmonic modes (a sin and a cos) with the same natural frequency. There is no unique vibration pattern that can be specified for these double modes. One should consider two orthogonal

shapes and when the structure is vibrating at that natural frequency, the structure can assume any form given by a linear combination of the two specified shapes. Suitable shapes are given by cos(nθ) and sin(nθ). These are circumferential distributions of displacement around the assembly with n nodal diameters. So at the natural frequency, the assembly can vibrate in any combination of these two patterns, that is in a shape of the form cos(nθ + ϕ). This implies that the assembly vibrates with n nodal diameters whatever the bladed disk mode shape may be. The orientation of these diameters depends on some additional external influence. It is thus possible that the nodal diameters lie on a blade or somewhere in between two blades, [44].

The single modes, only one mode at resonance, correspond to motions with either all the blades in phase (0 nodal diameters) or out of phase (N/2 nodal diameters, only possible if N is even).

Important remarks:

The 0 and 1 nodal diameter modes at the lower end of each family have a special characteristic. These three modes (one single and one double) differ from all the other modes (two or more nodal diameters) because they have a net motion of the centre of the disk. A 0 nodal diameter mode involves an axial or a torsional disk movement (see movement of the blades in figure 2.24c) while a 1 nodal diameter mode has translation of the disk along a diameter (see figure 2.24b). Therefore these three modes are also influenced by the shaft and bearings which support the disk. One should include these components to have more accurate estimates of the 0 and 1 nodal diameter modes, [44]. One must also take into account a second coupling between the different mode shapes. A coupling is likely to happen when both the frequency and the number of nodal diameters of two different mode shapes (for example first bending and first torsion) are close to each other. The influence of coupling is quite weak for modes that only represent pure bending or torsion, but it is significant for highly coupled modes like the FE-T (flapwise + edgewise + torsional) mode, [38].

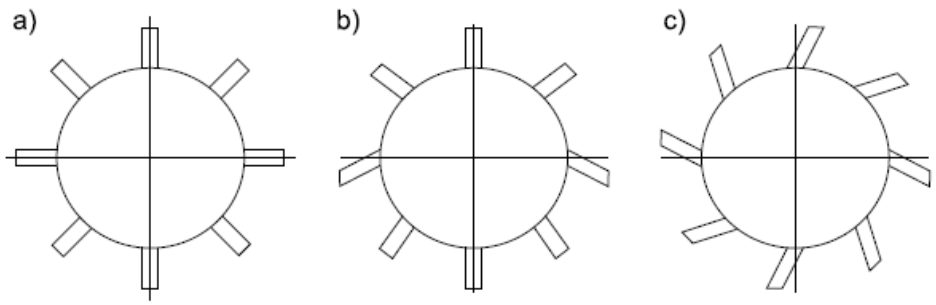

Figure 2.24 Blade motions during vibration: a) No vibration, b) 1ND with translation along diameter, c) 0ND with torsional disk movement

2.5 Bladed disk response

2.5.1 Engine order excitations

Excitations of a bladed disk are very closely related to engine orders (EO). The latter are harmonics (natural multiples) of the rotation speed. For example, a rotation speed of 3000 RPM is equivalent to (3000/60) rates per second = 50 Hz. Thus the first harmonic (=1 EO) is 50 Hz, the second (=2 EO) 100 Hz, the third (=3 EO) 150 Hz, etc. One pressure fluctuation (caused by for example a vane) during one rotation will be experienced by an observer rotating with the disk, as a pulsation of first EO. For instance, 5 vanes will cause pulsations of the 5^{th} EO, because the observer feels 5 pulsations per rotation. Sometimes these pulsations have strong higher Fourier components, thus previous example may also experience pulsations of the 10^{th}, 15^{th}, 20^{th}…EO. It is proven from tests that these Fourier components weaken as the component number increases.

2.5.2 Response of a bladed disk

Two angular coordinate systems are defined to describe the response of a bladed disk, [46]. The first one is a stationary reference frame where θ_0 represents the angle. The other reference frame is fixed to the disk rotating with rotational speed Ω (rad/s) and uses the angle θ. The relation between both coordinates is given by: $\theta_0 = \theta - \Omega\ t$ since the direction of the rotation and the angles are chosen opposite to each other.

Excitations with a certain EO are mostly initiated by pressure distortion fields of, for instance, S distortions located in the flow field. Generally, these pressure distortion fields are equally spaced on the circumference and do not have abrupt changes. Therefore, they can be represented as a sinusoidal forcing function V with amplitude A/2 (see figure 2.25), [47]:

$$V\ (\theta, t) = \frac{A}{2} * cos(S(\theta\ - \Omega t)) \tag{2.1}$$

The bladed rotor has M blades which transfer the forcing function V to the disk. It is thus very likely that they affect the nodal diametral patterns. The presence of the blades is approximated by a Fourier series in circumferential direction. For simplicity only the first component of this series is used such that blades are represented by:

$$B\ (\theta) = \frac{1}{2} * (1 + cos(M\theta)) \tag{2.2}$$

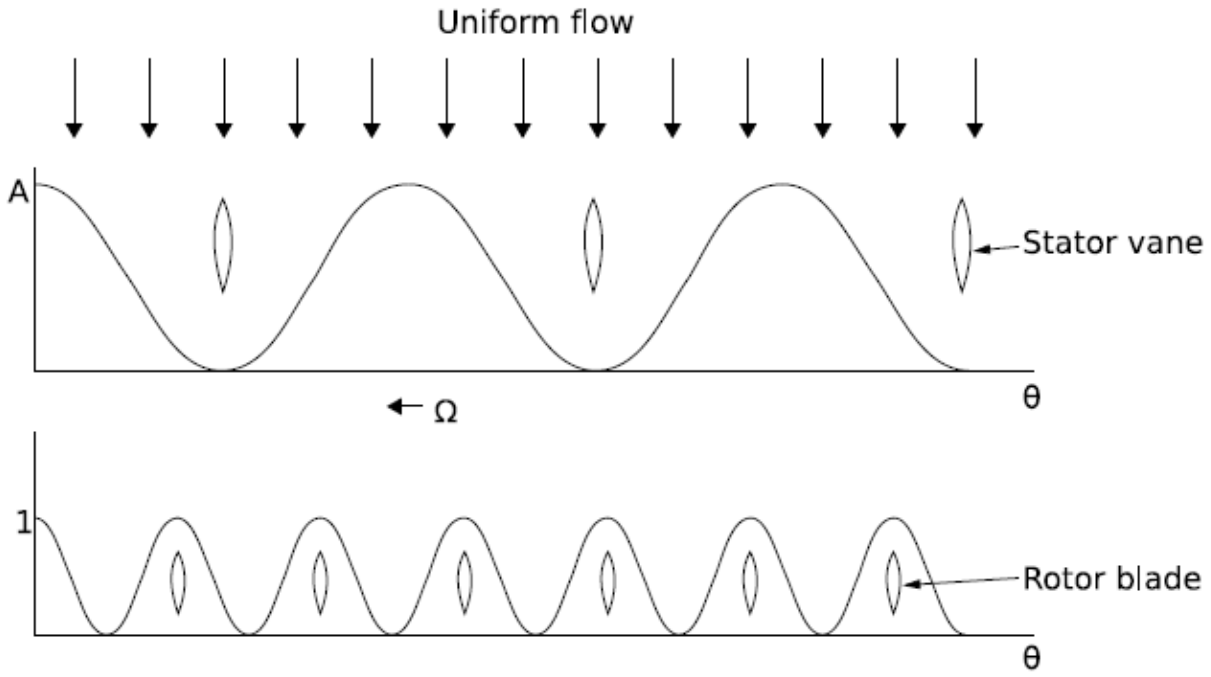

Figure 2.25 Sinusoidal distortioned flow due to the stator vanes (upper graph) and the sinusoidal representation of the rotor blades (lower graph)

The actual force F, felt by the blades, is then:

$$F\ (\theta) = V(\theta, t) * B(\theta) \tag{2.3}$$

Or:

$$F\ (\theta, t) = \frac{A}{4}\cos(S(\theta - \Omega t)) + \frac{A}{4}\cos(S(\theta - \Omega t))\cos(M\theta) \tag{2.4}$$

The double mode shapes of the n^{th} diametral mode are assumed to be $\phi_1(\theta) = \cos(n\theta)$ and $\phi_2(\theta) = \sin(n\theta)$ with eigenfrequencies ω_{n1} and ω_{n2}. Studying the response of a bladed disk in it's n^{th} diametral mode due to a force F is commonly done by using generalized forces N_1 and N_2 (for respectively the cosine and sine mode). The generalized force for each assumed mode is calculated with:

$$N_i = \int_0^{2\pi} F(\theta, t)\phi_i(\theta)\, d\theta \tag{2.5}$$

Or:

$$N_1 = \int_0^{2\pi} F(\theta, t)cos(n\theta)\, d\theta \tag{2.6}$$

$$N_2 = \int_0^{2\pi} F(\theta, t) sin(n\theta)\, d\theta \tag{2.7}$$

Substitution of the force F from (1.4) into (1.6) gives:

$$N_1 = \frac{A}{4}\cos(S\,\Omega t))\int_0^{2\pi}\cos(S\theta)cos(n\theta)\,d\theta + \frac{A}{8}\cos(S\,\Omega t)\int_0^{2\pi}\cos((M-S)\theta)cos(n\theta)\,d\theta + \frac{A}{8}\cos(S\,\Omega t)\int_0^{2\pi}\cos((M+S)\theta)cos(n\theta)\,d\theta \tag{2.8}$$

The terms in this expression are always zero except for the following numbers of nodal diameters n:

n = S → $N_1 = \frac{A\pi}{4}\cos(S\Omega t)$ (2.9a)

n = M - S → $N_1 = \frac{A\pi}{8}\cos(S\Omega t)$ (2.9b)

n = M + S → $N_1 = \frac{A\pi}{8}\cos(S\Omega t)$ (2.9a)

Similar for the generalized force N_2:

n = S → $N_2 = -\frac{A\pi}{4}\sin(S\Omega t)$ (2.10a)

n = M - S → $N_2 = \frac{A\pi}{8}\sin(S\Omega t)$ (2.10b)

n = M + S → $N_2 = -\frac{A\pi}{8}\sin(S\Omega t)$ (2.10a)

If a very lightly-damped system is assumed the generalized responses are calculated with a simplified convolution integral:

$$q_1(t) = \frac{1}{m_{n1}\omega_{n1}}\int_0^t N_1(\tau)sin(\omega_{n1}(t-\tau))\,d\tau \tag{2.11}$$

$$q_2(t) = \frac{1}{m_{n2}\omega_{n2}}\int_0^t N_2(\tau)sin(\omega_{n2}(t-\tau))\,d\tau \tag{2.12}$$

Where m is the modal mass or generalized mass of the mode. After integration, the generalized responses are found to be:

$$q_1(t) = W_{11}\cos(S\Omega t) + W_{12}\cos(\omega_{n1}t) \tag{2.13}$$

$$q_2(t) = W_{21}\sin(S\Omega t) + W_{22}\sin(\omega_{n2}t) \tag{2.14}$$

The parameters W_{ii} depend on the values of the generalized forces N_1 and N_2. On their turn, they depend on the number of nodal diameters (1.9 and 1.10). Therefore, in case the number of nodal diameters is equal to the number of stator vanes (n = S), the parameters Wii become:

$$W_{11} = \frac{-\pi A}{4m_{n1}(n^2\Omega^2 - \omega_{n1}^2)} \qquad W_{12} = \frac{\pi A}{4m_{n1}(n^2\Omega^2 - \omega_{n1}^2)}$$

$$W_{21} = \frac{-\pi A}{4m_{n2}(n^2\Omega^2 - \omega_{n2}^2)} \qquad W_{22} = \frac{\pi A}{4m_{n2}(n^2\Omega^2 - \omega_{n2}^2)}$$

Note that all W_{ii} can also be found for n = M − S and n = M + S.

One can see from the equations of the generalized responses (2.13 and 2.14) that once the system is set into motion, it will tend to vibrate at its natural frequency as well as to follow the frequency of the excitation. Since the system is (lightly) damped, the part of the motion not sustained by the sinusoidal excitation will eventually die out. This is the transient motion which describes the oscillations under free vibration at the natural frequency of the system. The motion sustained by the sinusoidal excitation is called the steady-state response.

Hence the system vibrates at the excitation frequency. It is thus possible to drop the second terms in the expressions of the generalized responses, because they represent a transient response. Therefore, the steady-state solution of the responses is:

$$q_1(t) = W_{11}\cos(S\Omega t) \tag{2.15}$$

$$q_2(t) = W_{21}\sin(S\Omega t) \tag{2.16}$$

The total response is calculated by the mode summation formula:

$$X(\theta, t) = \sum_{i=1}^{2} \emptyset_i(\theta) q_i(t) \tag{2.17}$$

Or:

$$X(\theta, t) = W_{11}\cos(n\theta)\cos(S\Omega t) + W_{21}\sin(n\theta)\sin(S\Omega t) \tag{2.18}$$

Here the result is considered for a perfectly tuned bladed disk, thus when $\omega_{n1} = \omega_{n2}$ and $m_{n1} = m_{n2}$ the response can be written as:

$$X(\theta, t) = W_{11}\cos(n\theta - S\Omega t) \tag{2.19}$$

Remember that W_{11} only exists ($\neq 0$) when n = S, n = M − S or n = M + S. Since the disk becomes stiffer with increasing nodal diameters, it is unlikely that strong excitations will occur for the case n = M + S. Only investigation of the other two cases is relevant:

-Case: n = S then:

$$X(\theta, t) = W_{11}\cos(n\theta - n\Omega t) = W_{11}\cos(n\theta_0) \tag{2.20}$$

-Case: n = M - S then:

$$X(\theta, t) = W_{11}\cos((M - S)\theta - S\Omega t) = W_{11}\cos(n\theta_0) \tag{2.21}$$

In the first case, the n diametral pattern always travels with the same speed but in the opposite direction of the disk rotation. The response can be seen as a standing wave in the stationary reference frame.

For n = M − S, the disk response has a diametral pattern that can travel in opposite or same direction as the rotation, depending on the values of M and S (whether n is < 0 or > 0). Be aware that a rotating reference frame is used, so the diametral patterns will only rotate slower or faster than the disk speed when they are seen in a fixed reference frame.

Note that there is also danger for 2M − S, M − 2S, 2M − 2S, 3M − S,… modes which are found if higher Fourier components were used for the mathematical representations of the blades and the distortions.

2.5.3 Classification of bladed disk response

In general a distinction is made between two response modes X(θ, t) when resonance occurs, [48]. They differ according to whether the number of rotating blades has an influence or not. In both cases, the initiation is due to a number of stationary elements S.

Critical disk speed resonance

The response for this type is similar as in formula 2.20. The conditions which must be simultaneously fulfilled are written below:

$$\begin{cases} (a) & M > 1 \\ (b) & yS = h = n \\ (c) & f_r = n\Omega \end{cases} \tag{2.22}$$

With: y integer value, typically 1 and 2, higher values give much lower response

M number of rotating blades

S number of stationary elements ex. vanes

h harmonic of speed = EO

f_r natural eigenfrequency during rotation rotational speed in Hertz

n number of nodal diameters

These conditions demand a bladed disk with at least two blades to transfer the pressure fluctuations (forces) to the disk (a). The eigenfrequency of the mode must be equal to the frequency of the excitation (c). For the last but most important condition (b), the bladed disk motions must be in phase with the effective sinusoidal pattern of the excitation source. When the latter condition is not fulfilled, then the effective forces would cancel out in a revolution. This is illustrated in figure 2.26, where an n diameter mode shall be resonant with n and not with n+1 sinusoidal pulsations per revolution.

Example:

It is disconcerning for a 4 nodal diameter mode (n = 4) of a bladed disk to place 4 stator vanes (S = 4) in the inlet. At a certain rotational speed (= disk critical speed), condition (c) will be fulfilled. Since the vanes produce 4 pulsations (h = 4) during one revolution, the first Fourier component (y = 1) of these pulsations fullfills condition (b): 1S = h = n. The same can be said for the second Fourier component (y = 2) of 2 vanes in the inlet, because then 2S = h = n. Note that in this example both critical disk speeds are equal.

Blade/vane interaction resonance

This type is defined as resonance due to the presence of blades. Since blades transfer pressure fluctuations to the disk, there will exist some resonance at certain number of blades. For this type of resonance, the following three conditions must be simultaneously fulfilled:

$$\begin{cases} (a) & |yS \pm zM| = n \\ (b) & yS = h \\ (c) & f_r = yS\Omega \end{cases} \tag{2.23}$$

with z an integer value, typically 1 and 2, higher values give much lower response. From condition (a) one can conclude not to use equal or multiple numbers of blades and vanes. In that case no circle modes (NC) can be excited in the 0 (= n) nodal diameter mode, because the 0 ND mode cannot exist ($yS \neq zM$). Remark that condition (b) is there to emphasise that resonance is at a harmonic related to the number of stationary elements and not to the number of rotating blades.

Example:

Consider the example of a bladed disk with 27 blades and 16 stationary vanes. For the first resonance type, two critical disk speeds should be investigated at the 16^{th} and 32^{nd} EO for respectively the same nodal diameter modes. These EO should also be investigated for the second type of resonance. The $|2S-M| = |2x16-27| = 5$ and $|S-M| = |16-27| = 9$ nodal diameter modes will interact (at certain rotational speed) with respectively the second harmonic (h = 32 EO) and the first harmonic of the vanes (h = 16 EO).

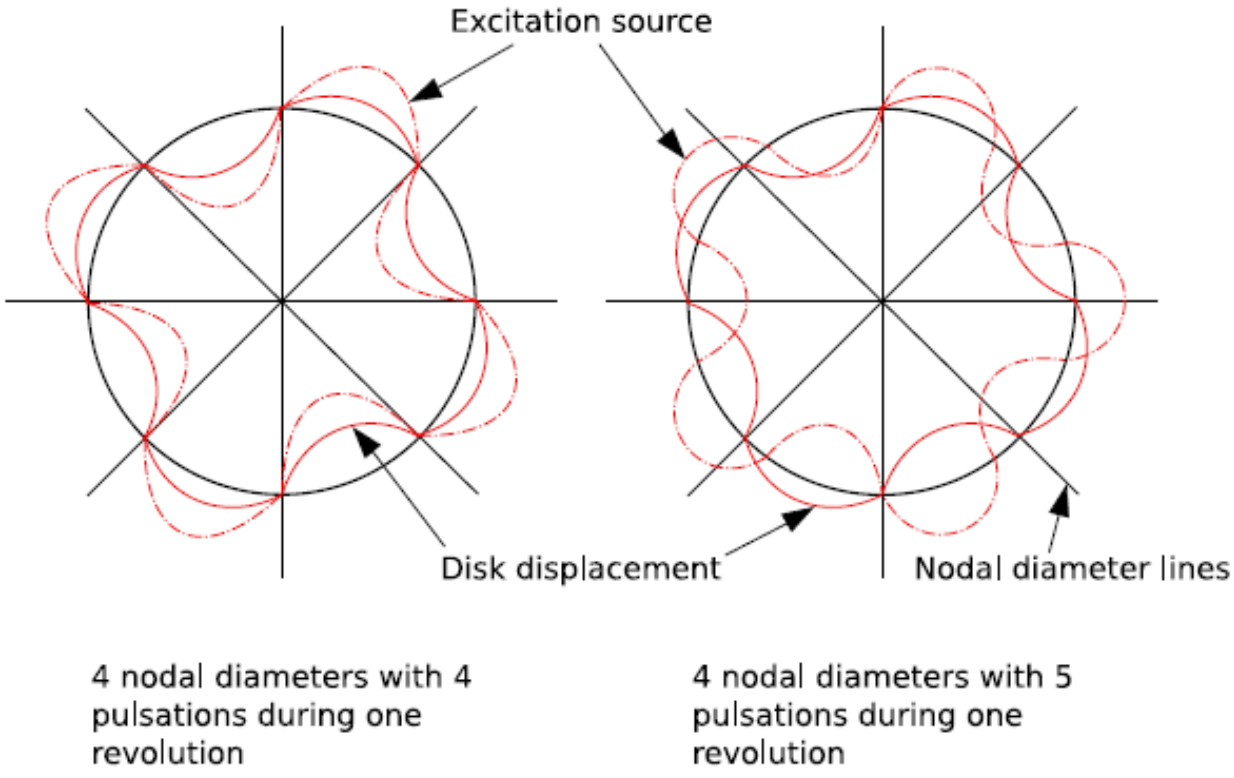

Figure 2.26 Nodal diameters and excitation of the same and not the same EO

2.5.4 Single and double modes

All diametral modes of a bladed disk consist of single and double modes, [49]. The response of a bladed disk at a disk critical speed Ω (rad/s), where the disk resonates in an n diametral mode to an n^{th} EO excitation (n = S), was found to be (formula 2.18):

$$X(\theta,t) = W_{11}\cos(n\theta)\cos(n\Omega t) + W_{21}\sin(n\theta)\sin(n\Omega t) \quad (2.24)$$

Assuming a perfectly tuned system:

$$X_0 = W_{11} = W_{21} \quad (2.25)$$

Thus:

$$X(\theta,t) = X_0\cos(n\theta)\cos(n\Omega t) + X_0\sin(n\theta)\sin(n\Omega t) \quad (2.26)$$

One can consider each of these two terms being the combination of a harmonic excitation at the same frequency and phase of all blades (sin(nΩt)), but with the amplitude depending on the position on the disk in a sinusoidal pattern (X_0 sin(nθ)). Both terms of X(θ, t) represent a standing wave in a rotating reference frame. These standing waves are the double modes of a diametral response. An example of standing waves with 2 nodal diameters from a 12 bladed disk can be seen in figure 2.27. Combining the standing waves results into a travelling wave (or a standing wave in a non-rotating reference frame):

$$X(\theta,t) = X_0\cos(n(\theta - \Omega t)) \quad (2.27)$$

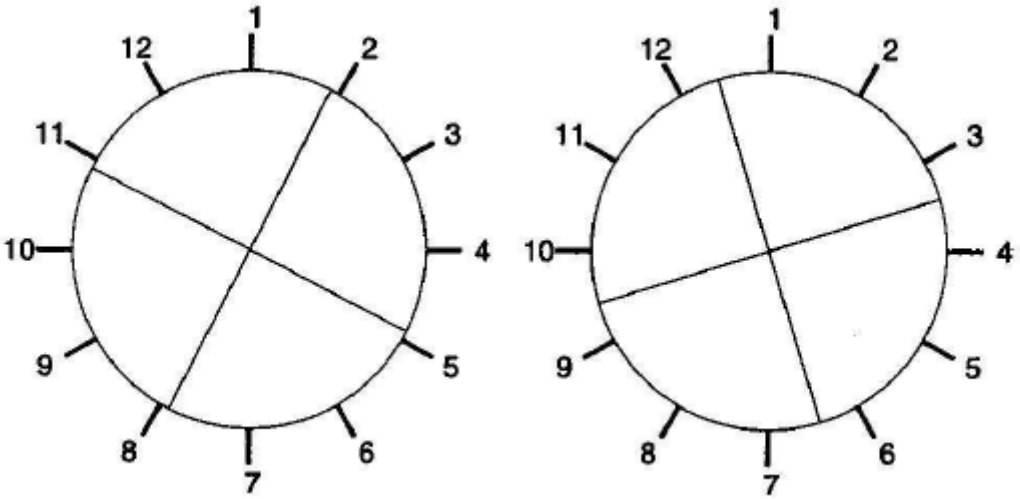

Figure 2.27 Nodal diameters of orthogonal standing waves of a 12 bladed disk

Considering now the zero and N/2 nodal diameter modes of a tuned bladed disk. The zero diametral mode is found from (2.19) with n = M − S = 0 and $X_0 = W_{11}$:

$$X(\theta, t) = X_0 \cos(n\theta - S\Omega t) = X_0 \cos(-S\Omega t) \tag{2.28}$$

There is no phase difference between the responses of the blades and the total response is one standing wave. Thus all blades have the same deflection at each time.

An excitation of an N/2 diametral mode means that the phase difference between adjacent blades is 180°. Suppose that the blades coincide with the nodal points of sin (nθ), then each nodal diameter of cos (nθ) lies in between two adjacent blades. The second term in (2.18) is always zero, such that the response for each blade with blade number n (n = 1 → N) can be written as :

$$X_n = (-1)^{n-1} X_0 \cos(S\Omega t) \tag{2.29}$$

This expression also represents one standing wave.

Both, the zero and N/2 nodal diameter mode, consisting out of one standing wave (in a rotating reference frame) are classified as single modes.

2.6 Campbell diagram

Campbell diagrams are used to find rotational speeds which can lead to dangerous excitations of a bladed disk, [50]. Since a diagram of the latter is quite complicated, it is more appropriate to investigate a diagram of an isolated single rotating blade (no blade coupling possible), see figure 2.28. This diagram has the rotating speed (rpm) as x-coordinate and the frequency on his y-axis. The lines with (1F, 2F, 1T, 3F) represent the eigenfrequencies of the mentioned blade mode shape. Note how the stiffening of the centrifugal force affects the eigenfrequencies. The de-stiffening effect of the temperature is not included. A second type of lines are the EO (=Engine Order) lines. These lines are straight, because 1 EO = 1 pulsation per rotation times the RPM/60, 2 EO = 2 pulsations per rotation times the RPM/60, etc.

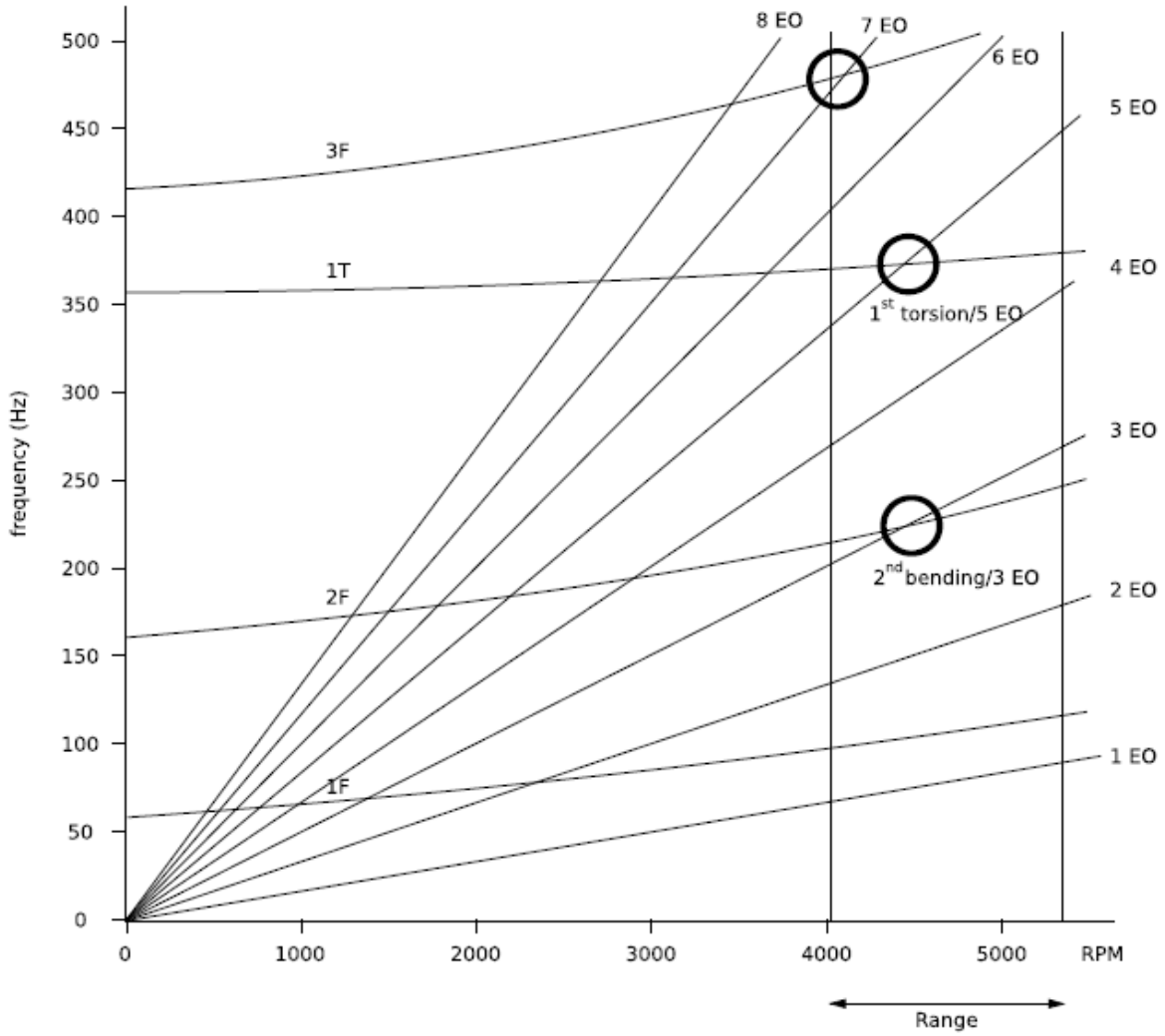

Figure 2.28 Campbell diagram of blade on rotating disk

Intersections of both line types are dangerous operating points, since they stand for equal frequencies of an excitation source and a mode shape. In a reduced operating range starting at 4000 RPM up to 5500 RPM, all (3) intersections are highlighted. Note that, for example, the critical speed of a 2nd bending/3EO intersection requires 3 distortions within one rotation. This Campbell diagram warns to certainly avoid having 3, 5 or 7 distortions during one rotation. For instance, four vanes in front of this rotating disc would give no problems for the blade in this operating range, since there is no intersection of the 4 EO line with an eigenfrequency line.

Everything explained up to now is valid for a single blade, but problems occur when extending this diagram to a bladed disk. For a bladed disk, in addition to the frequency, also the mode shape of the excitation source is very important for resonance. Therefore, the nodal diameters are needed. In figure 2.29 the Campbell diagram is drawn from a 36 (= N) bladed disk. All horizontal lines in this figure represent the eigenfrequencies of one and the same bladed disk mode but each line has a

specific number of nodal diameters going from 0 ND (lowest line) up to N/2 ND (upper line). Thus at every horizontal line the blades are vibrating in, for example, the first flapwise bending mode (1F), but each line has its own specific number of nodal diameters. Note how the upper eigenfrequency lines are lying closer to each other. Since the disk becomes stiffer with increasing number of ND, the eigenfrequency is approaching the blade alone frequency, as explained in section 2.3 with figure 2.21. This means that the upper eigenfrequency line from figure 2.29 corresponds to one of the eigenfrequency lines (in this case the 1F line) in figure 2.28.

Adding the nodal lines to the Campbell diagram leads to crowdy and hard to use diagrams, see for example figure 2.30 which is a combination of figures 2.28, 2.29.

2.7 Interference diagram

A better way to find dangerous rotational speeds of a bladed disk, is by representing the frequency vs. the nodal diameters, [51]. This diagram is called an interference or SAFE (Singhs Advanced Frequency Evaluation) diagram and was already used in figure 2.21 for showing the influence of disk stiffness. A more extended diagram is drawn in figure 2.31 for a 64 bladed disk. Each line represents the eigenfrequency of a bladed disk mode for all possible nodal diameters. The solid lines are bladed disk modes with the blades vibrating in a blade mode, because they converge to a blade alone frequency. The dotted line represents a bladed disk mode which is dominated by a disk mode. For some modes it is harder to achieve a 0 ND mode than the 1 and 2 ND modes. That is why most of the solid lines are characterized by a "fish hook" at low nodal diameters. In figure 2.31 the nodal diameters are drawn up to N/2, but it is also possible to draw higher (indistinguishable, see figure 2.19 in section 2.3) nodal diameters. This is done in figure 2.32 (dotted line) for one family (= one eigenfrequency line from figure 2.31).

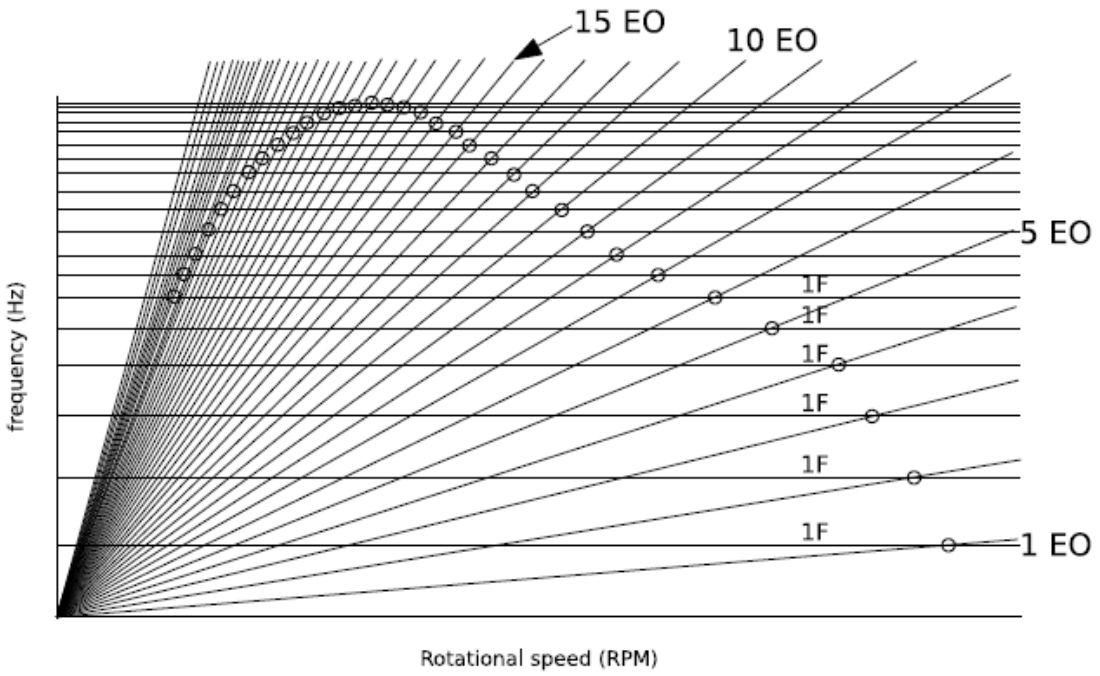

Figure 2.29 Campbell diagram for the first blade flapwise bending mode shape (at all possible nodal diameters) of a 36 bladed disk

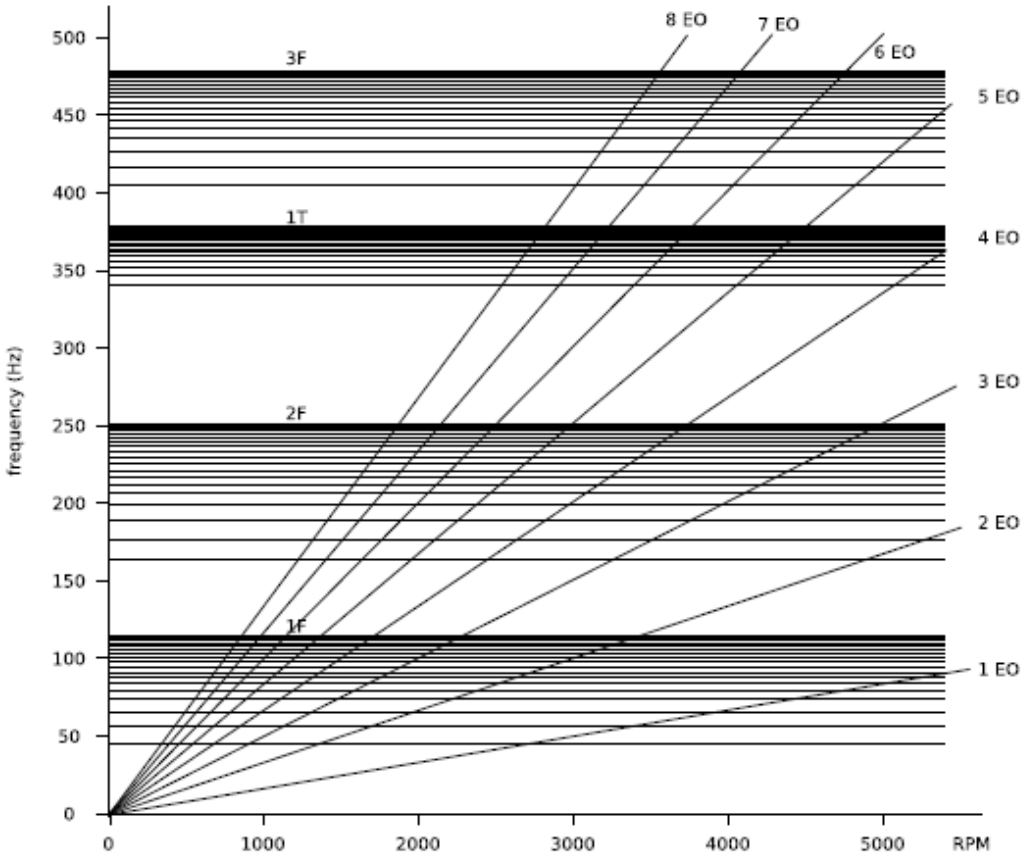

Figure 2.30 Campbell diagram for 4 bladed disk mode shapes (at all possible nodal diameters) of a 36 bladed disk

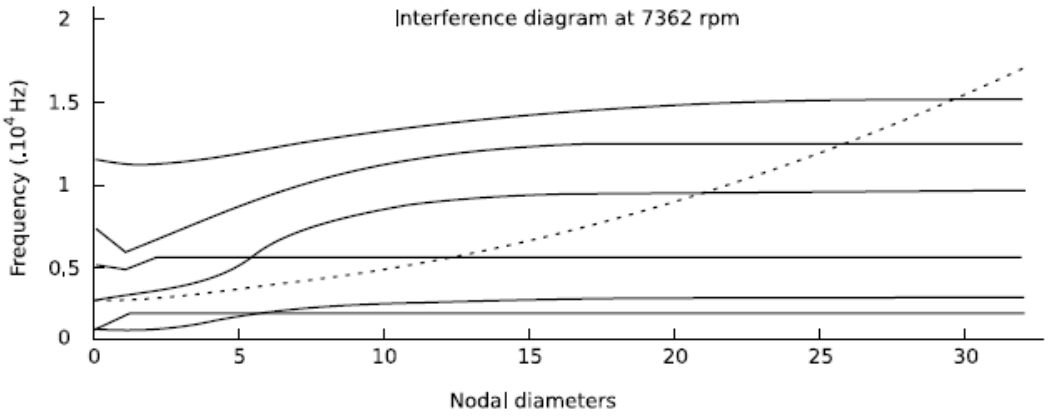

Figure 2.31 Interference diagram for a 64 bladed disk

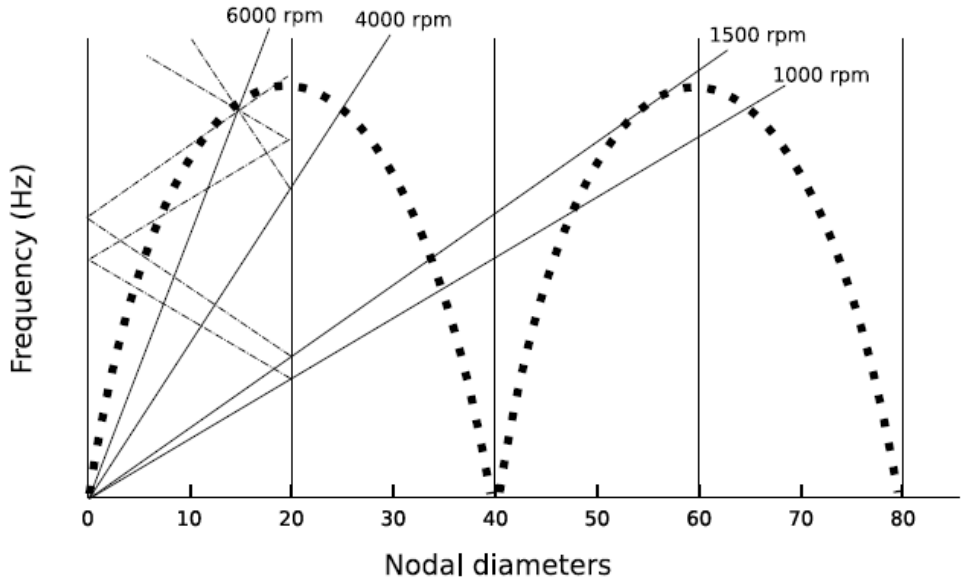

Figure 2.32 Interference diagram for one family mode of a 40 bladed disk

The solid lines, indicated with a rotational speed, in figure 2.32 represent constant speed lines. For these lines the x-coordinate indicates the EO of possible excitation forces. Each point on the constant speed lines is found by multiplying the EO(=ND) times the rotational speed (in rates per second). Each intersection of the constant speed lines with an eigenfrequency line is a dangerous excitation, because the excitation source and the blade disk have equal frequency and mode shape.

This diagram is drawn for 80 ND whereas 20 (= N/2) ND would be sufficient because higher nodal diameter modes (> (N/2) ND) are indistinguishable. The intersections with the constant speed lines can be retrieved by reflecting those lines on the vertical lines through the 0 and N/2 nodal diameter coordinates. The intersections with the reflected speed lines (dash-dotted lines in figure 2.32) occur

at the same frequency as for the nonreflected speed lines, but one only has to calculate the bladed disk modes up to N/2 ND.

It should be mentioned that the bladed disk mode (dotted line) in figure 2.32 is drawn for all rotational speeds, but they lie on top of each other because the temperature and centrifugal (de-)stiffening effects are not included. Including them would make the diagram rather complicated. Since the temperature and centrifugal effects are counteracting each other, it is doubtable to include them.

Next to the interblade coupling, the coupling between different mode shapes can be showed in interference diagrams, see figure 2.33. Mode coupling occurs in zones where two or more eigenfrequency lines of different bladed disk modes are close to each other. In these zones, called veering zones, modes are mostly a combination of, for example veering 2 and 3, in-plane bending mode shapes of the blades and out-of-plane motions of the disk, [49]. Taking a closer look to the veering zones in figure 2.33, one can denote a difference between veering 1 and the other two. Veering 1 has a wider nature (wider in frequency and nodal diameters), which indicates that there is a strong coupling between the blade and the disk motions. The strong coupling between blade and disk also means that the interblade coupling through the disk will be much stronger than at the veering zones 2 and 3.

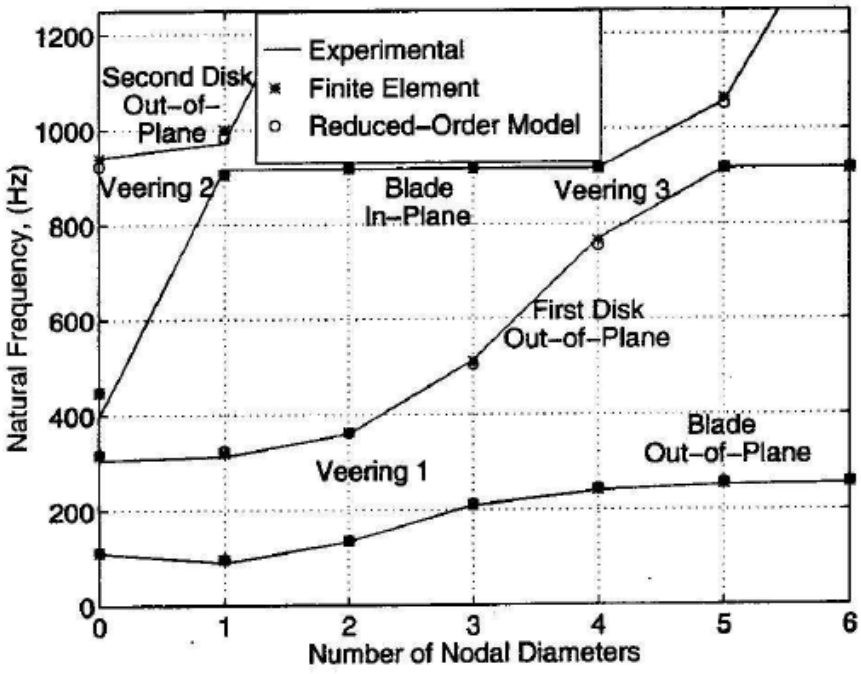

Figure 2.33 Mode coupling in interference diagram of a 12 bladed disk

2.8 Blade tip clearance variations

The accurate control of running gaps between static and rotating components is vital to preserve mechanical integrity and ensure a correct functioning of any compact rotating machinery. In modern aircraft propulsion systems, blade tip clearance plays a major role in the characterization and development of reliable and efficient aero-engines. In current turbine stages, hot leakage jet flows above the rotor airfoil tips (figure 2.34 b) resulting in 30% of the total aerodynamic losses [52]. Moreover, during the machine operation the casing and the bladed disks undergo different dilatations because of different thermal inertia values of the components. This result in blade tip gap variations, as well as the shaft orbiting due to rotor eccentricity (figure 2.34 a). Therefore, the gap between the rotor blade tip and the stationary shroud must be minimized. However, turbine designers commonly set a safe minimum gap to prevent mechanical rubbing between the blade tips and the casing that may result in rotor damage or catastrophic failure. Thus, the selection of an optimum tip clearance results from a trade-off between aerodynamic performance and mechanical integrity. Unfortunately, as a consequence of manufacturing and installation tolerances, vibrations, different expansion rates of blades, rotor disk and casing induced by thermal and speed transients, the rotor tip clearance undergoes large variations during engine service operations [1]. Hence, advanced tip clearance active control concepts must rely on accurate real-time clearance measurement systems to achieve highest engine efficiency with increased safety margins. Additionally, blade tip clearance measurements are routinely used in engine development programs to verify the mechanical design and tune numerical predictions [53].

In aero-engines the most challenging tip clearance measurements are carried out in the high pressure turbine where temperatures, pressures and rotor speeds are the highest. Sensors should thus be capable of withstanding temperatures above 1500 K, have a reduced size and improved working range (0-5 mm), and a high bandwidth to resolve blade passing frequencies of the order of tens of kHz. Tip gap measurements in current gas turbine applications are commonly based on capacitance systems. Similarly to eddy current probes, capacitance-based tip clearance sensors are low cost and rugged devices with the best potential to adapt to harsh working conditions. The technique relies on the measurement of the capacitance between an electrode and a moving metallic target. Different capacitive detection methods have been developed to sense the running tip capacitance. However, no sensors for engine flight have yet been realized [4]. The gas turbine industry therefore has a strong interest for improved tip clearance instrumentation for routine use on in-service engines.

Further technology development is needed to provide measurement systems with enhanced accuracy, increased working range and extended lifetime.

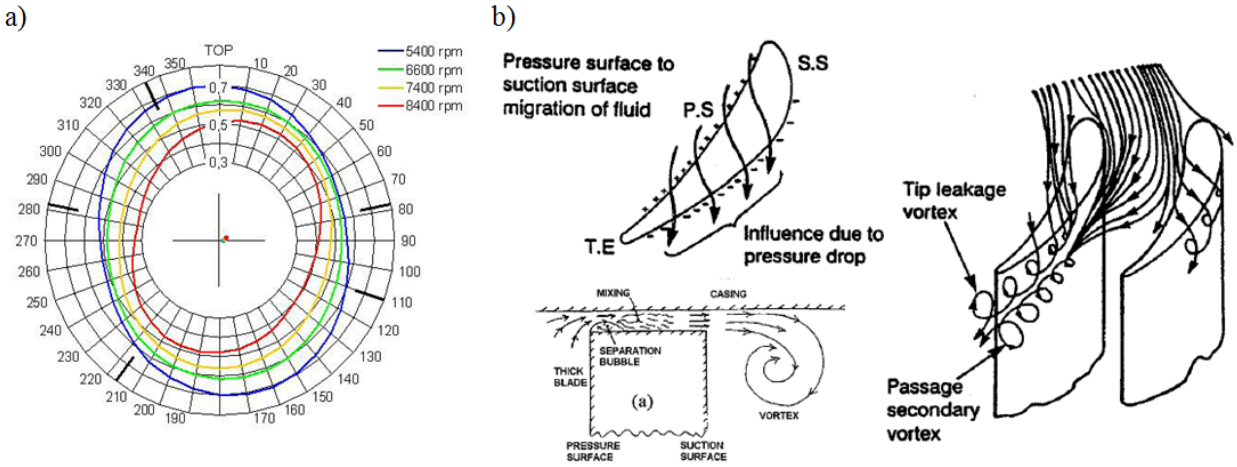

Figure 2.34 a) Example of shaft orbiting b) Tip leakage flow

2.9 Conclusions

The aim of this chapter was to introduce two fundamental phenomena to monitor in turbomachinery: the vibration of the disk and blades and the vatiation of the gap between the blade tip and the casing. It is not trivial to monitor these parameters, especially by a contactless technique and it is even more complicated to mitigate their effects on the machine. A clear understanding of the theory behind vibration problems and clearance variations it is mandatory before analysing measurement results.

3 Blade Tip Clearance and Blade Tip Timing measurement systems

3.1 Introduction

A simultaneous Blade Tip Clearance (BTC) and Blade Tip Timing (BTT) measurement systems is a non-intrusive instrumentation for the measurement of blade tip clearance and blade vibrations. As shown in figure 3.1, it is made of stationary sensors (S_1, S_2, …, S_n) mounted around the casing, connected to dedicated electronics for the signal amplification and filtering, then to a data acquisition system (DAS) and finally to a PC or a data processing and visualization system. BTC and BTT systems are based on the analysis of key parameters of the sensors signals and time intervals.

This chapter illustrates the principles behind the signal analysis of a BTC and BTT measurement system.

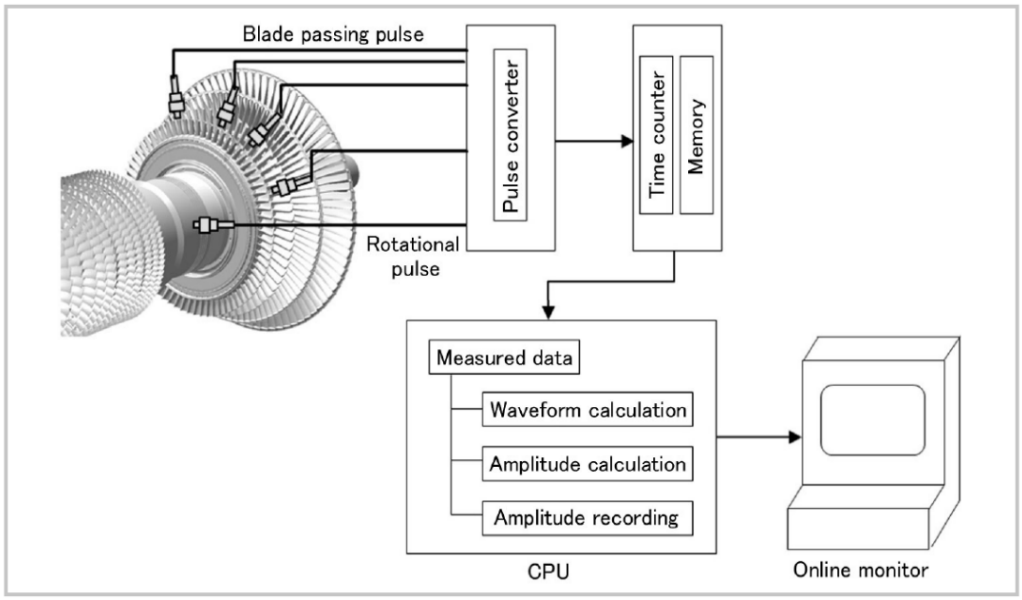

Figure 3.1 Blade tip clearance and blade tip timing measurement system

3.2 The principle for the measurement of blade tip clearance

Whatever the sensor technology is, when a blade passes in front of a stationary probe an output signal is generated. To monitor the clearance, the signal must be sensitive to the variations of the gap between the head of the probe and the blade tip.

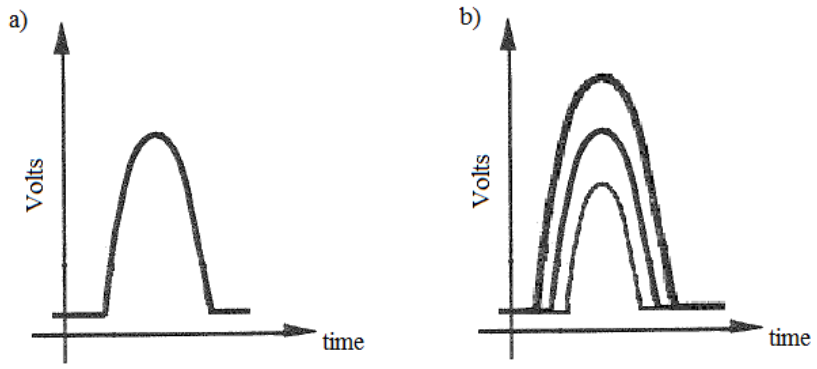

Figure 3.2 a) Typical sensor signal b) Influence of clearance variation

Every sensor type has its working principle and the shape of the output signal generated at the blade passage is usually different. Nevertheless, the system identifies one or more key parameters representative of the current blade tip gap. The key parameters must be robust and repeatable. Typical key parameters used to monitor the clearance and its variation are the peak to peak value of the output signal, the maximum peak value or the minimum. For instance, it can be considered a typical output signal of figure 3.2a. The variation of the blade tip gap, in this case, induces a variation of the signal amplitude, as in figure 3.2b. Hence, the key parameter in this case can be the maximum peak value of the signal.

So far it seems easy. In reality, the key parameter can vary with external disturb like the machine speed variations, different blade material, the temperature, etc.. It is not trivial to identify a key parameter well representative of only the blade tip clearance and is even more difficult to characterize and compensate for all the sources of uncertainties affecting the measurement chain.

Another important aspect to consider in the signal analysis is the speed of the process. Once the key parameter is defined, there is somewhere in the system a signal processor that must extract this parameter for every pulse, per blade, per revolution. Nowadays the DAS are very fast, but the extraction of the parameter and conversion in tip gap (millimeters) must be fast and intelligent, to avoid a bottleneck. Imagine to have a DAS with a sampling frequency of 1MHz per channel, to use 8 sensors around the casing and to have a rotor with 24 blades rotating at 10000 rpm. The system must extract and convert 4000 maximum peaks values per blade, per revolution, per channel, in real-time only for clearance measurements!

This is why, when designing the software to process the data, it is important to develop light routines and intelligent procedure to cut the non-interesting parts of the signals.

3.3 The principle for the measurement of blade vibrations

BTT systems are based on complex processing methods developed for the first time more than 30 years ago from researchers of the Arnold Air Force Base, NASA and Brown Bovery [54-56].

This non-intrusive technique for the measurement of blade vibrations was born as substitute of strain gauges measurements. The latter are intrusive and needs a complex telemetry system to transmit the data. Moreover, BTT ensures the measurements of all the blades at the same time, whereas the strain gauges are reliable and have a consolidate technique but referred only to these blades where the gauge is applied.

The concept behind a BTT system is simple: when a blade is rotating and vibrating, the time of arrival (TOA) of the blade tip in front of a stationary sensor will depend on the rotor speed and on the displacement due to its vibration. Once the rotor speed is known, the theoretical time of arrival can be predicted and the remaining time variations will only depend on blade vibrations. Hence, blade vibrations can be measured by means of time variations.

To better explain this concept it can be considered the blisk of figure 3.3. There are 4 blades and 1 stationary BTT probe. Every time a blade passes in front of the sensor, a typical output signal (as the one in figure 3.2a) is generated. During the first round, there are no vibration and 4 pulses equally spaced in time are acquired. On round II, the blade 3 vibrates, the tip is backward deflected when passes in front of the sensor and the corresponding signal is delayed (+ Δt) with respect to the non-vibrating condition. On round III, the blade 3 vibrates with opposite phase, the tip is forward deflected when facing the sensor and the corresponding pulse is in advance (-Δt) with respect to the non-vibrating condition. By knowing the time variations (± Δt), it is possible to calculate the blade displacements.

In case of no-vibration, the mounting angles of the blades are known ($\Delta\theta$) and the TOA of every blade will depend only on the rotor speed (3.1):

$$\mathrm{TOA} = \frac{\Delta\theta}{\omega} \tag{3.1}$$

The disk speed (ω) is also known from a reference signal (REF), which can be a Once Per Rev (OPR) sensor on the shaft or averaging the blade pulses on one revolution (further detail on chapter 4).

In presence of vibration, the equation 3.1 is still used to calculate the theoretical TOA of every blade per revolution. Nevertheless, in this case the real sensor signal will arrive shifted in time (± Δt) due to the blade vibration. By measuring the time variations (± Δt), it is possible to calculate the blade deflection samples S_i:

$$S_i = v_t \cdot \Delta t \qquad (i: 1\ldots.N) \qquad (3.2)$$

where N is the number of blades and v_t is the tip velocity, calculated as:

$$v_p = \omega \cdot R \qquad (3.3)$$

where *R* is the tip radius.

The motion of the blade tip is the superposition of two contributions: its rotation around the shaft and its vibration. The analytical expression is:

$$s(t) = \omega \cdot R \cdot f_1(t) + A \cdot f_2(t) \qquad (3.4)$$

The first term of (3.4) is the contribution of the rotation, the second is the vibration. The latter represent the generic formulation of the blade vibration to measure:

$$s(t) = A \cdot f_2(t) \qquad (3.5)$$

where $f_2(t)$ is a periodic function of period T, frequency (f = 1/T) and amplitude A.

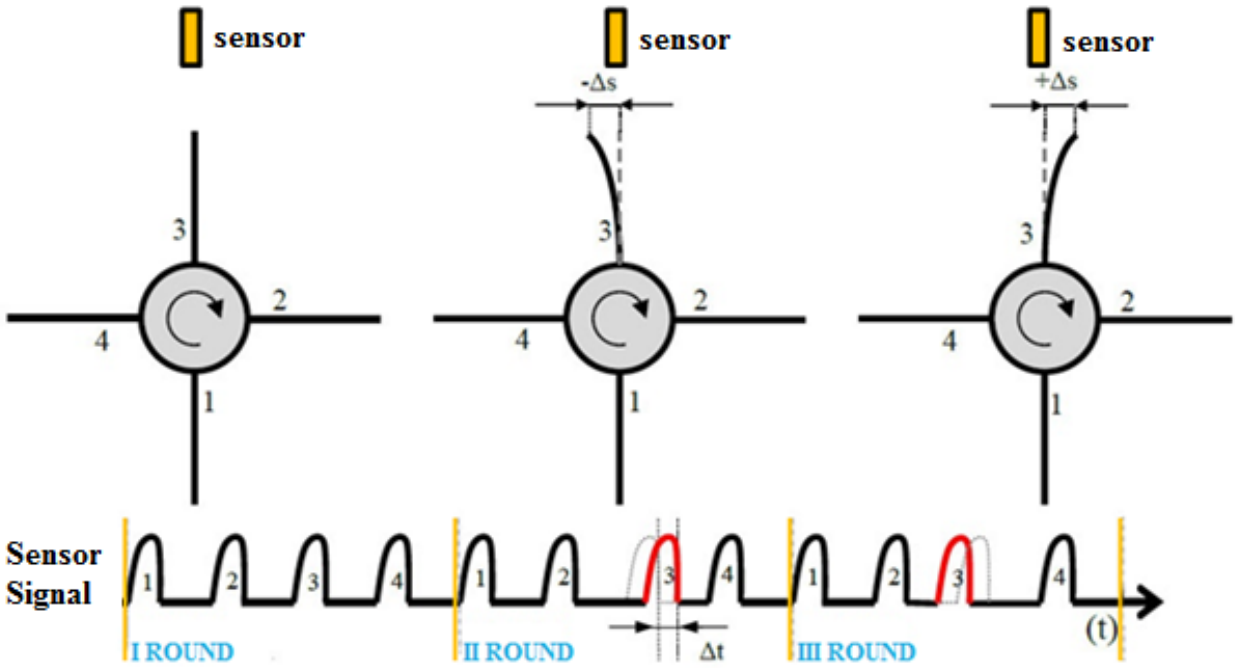

Figure 3.3 The concept of the TOA variations

The idea of the BTT technique is to measure blade vibrations of generic formulation (3.5) from the displacement samples (S_i) of the blade tip measured from the stationary sensors. To do this, complex algorithm calculates the TOAs of every blade from the REF signal, detects the key parameter time variation ($\pm\Delta t$) from the sensor signal for every blade, converts in displacement sample (S_i), finally, manipulates and fits the data with different methods to retrieve the measured vibration. Without going into detail, it can be imagine that more the measured samples, more the fitting points, better the result. Nevertheless, more samples means more sensors, more electronics, more data to process. Hence, the choice is a trade-off, between the costs, the complexity of the system and the needed accuracy. (Further detail on the algorithm are presented on chapter 4).

The BTT systems measure blade vibrations which can be synchronous or asynchronous, depending on the relation between the disk frequency and the blade vibration frequency. Synchronous vibrations have a frequency which is an integer multiple of the rotational frequency. If this condition is not satisfied, the vibration is asynchronous.

In case of a synchronous vibration (figure 3.4b), the measured displacement samples of one blade will be the same at every revolution. It is the so-called “stationary wave”. One can realize that having only one sensor it is not possible to measure vibrations in this condition. (In reality this is not fully true as it will be explained in the following chapters, nevertheless the accuracy of the system is decreasing with the sensors number). Moreover, considering the asynchronous vibration in figure 3.4a, it can be seen that, if the number of sensors is not enough, the fitting points to “rebuild” the vibration are not sufficient and the system is working in aliasing condition.

An innovative approach to reduce the sensors number and improve their positioning around the casing was presented by Rossi and Brouckaert [57]. To avoid aliasing, a minimum of 2 samples per blade vibration period must be taken. Nevertheless, this can be not sufficient to correctly reconstruct the vibration patch. Figure 3.5a shows a BTT system with 4 sensors every 90°. The black curve represents the real blade vibration and the red dots the measured samples. In this first case, all the sensors “see” a zero displacement because they are placed in a wrong position, where the tip is not moving. The work presented in [57] suggests to mount the sensors around the casing in a non-equally spaced way, as in figure 3.5b. It is clear from the graph of the measured displacements that, the samples now are well representative of the vibration patch. Finally, by having the sensor not-equally spaced, it is possible to correctly reconstruct vibration patches at different frequencies (figure 3.5c).

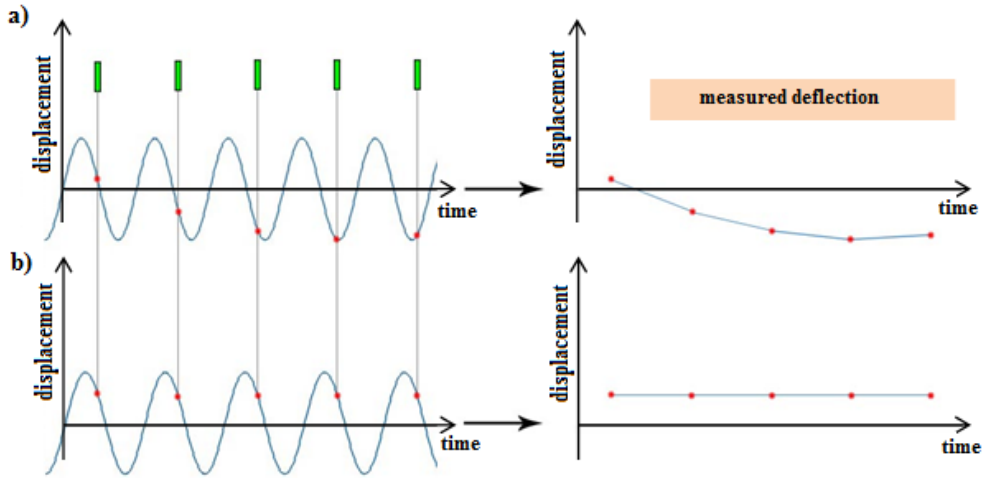

Figure 3.4 Example of a) asynchronous and b) synchronous vibration

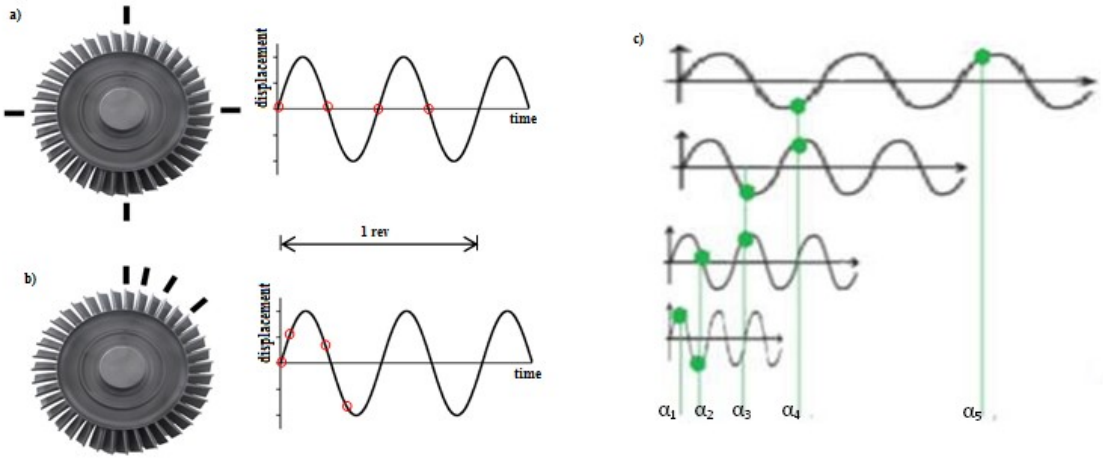

Figure 3.5 a) Equally spaced sensors b) Non-equally spaced sensors c) Sampling of different frequencies with non-equally spaced sensors

3.4 Conclusions

This chapter has introduced the basic principles behind a tip-timing and tip-clearance measurement system. Although it seems easy, it requires very complex data processing algorithms and powerful acquisition systems.

The aim of this research project was to investigate on the possibilities of using the magnetoresistive effect on BTT and BTC systems. Hence, the basic principle here described were considered and implemented in this project. Nevertheless, the system to develop in this phase could be based on only one sensor and one channel processing method. Multichannels routines and dedicated acquisition systems are already commercially available, therefore the innovation and the research project is focused on developing a new sensor

4 Design of the hardware and the software of the measurement system

4.1 Introduction

This chapter illustrates step by step all the phases of the design and realization of the hardware and software components of the measurement system.First the magnetoresistive elements are presented. Then numerical and experimental tests for the sensor development are summarized. The third part regards the first sensor prototype: the final assembly of the first prototype of the probe is reported. Subsequently, the dedicated electronic for the signal amplification and filtering is described. Finally, this chapter ends with the description of the universal calibration bench realized and the fundamentals of BTT and BTC data processing.

4.2 The magnetoresistive sensing element

In 1857, William Thomson (alternatively known as Lord Kelvin) discovered that the resistance of the iron changes under magnetization. The property of a metal to change resistance with the variation of an applied magnetic field is the magnetoresistive effect. At that time, one common application of magnetic devices was the realization of power transformer. Some ferromagnetic materials, under the influence of an applied magnetic field, present compression or expansion with generation or loose of heat. This phenomenon is called magnetostrictivity. Around 1910 it was discover a special alloy of nickel-iron (Ni81Fe19) with almost zero magnetostriction: the permalloy. It is consider a soft magnetic material, in the sense that its magnetization can be easily modified by external magnetic fields. Nowadays, magnetoresistive sensing elements are realized with very thin film of permalloy on silicon wafers. The permalloy is an anisotropic material: its magnetoresistivity depends on the direction of the applied magnetic field. In particular it has two main axis: the Easy Axis (EA) which is the principal magnetic axis of the film and the Hard Axis (HA), perpendicular to the previous one. Considering the film of permalloy of figure 4.1, its resistance R can be calculate as follows [58]:

$$R = \rho_{vol} \frac{L}{w \cdot t} \quad [Ohm] \tag{4.1}$$

where ρ_{vol} is the resistivity of the material.

To better highlight the change of resistance with respect to its mean value, it is often used the parameter percentage of variation of resistance, defined as:

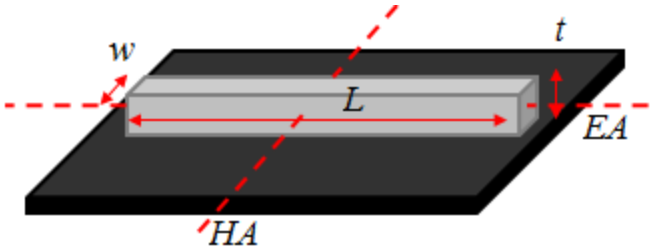

Figure 4.1 Film of permalloy

$$R_{\%} = \Delta R / R_{max} \cdot 100 \qquad (4.2)$$

In this project, the magnetoresistive sensing element Honeywell "HMC1501" was used to build the sensor. The Voltage supply of the sensing element is is 5 V, the angle of measure is from -45 to 45 deg, the sensitivity is 2 mV/deg, the measure resolution is 0.07 deg and the operating temperature range is from -40 to 125 °C.

The HMC1501 is made of a saturated-mode Wheatstone bridge. The output voltage of the bridge is function of the direction (θ) of the magnetic induction over the sensing element surface. The change of the output signal with theta is presented in Figure 4.3; (further information in [58 – 60] and in the appendix).

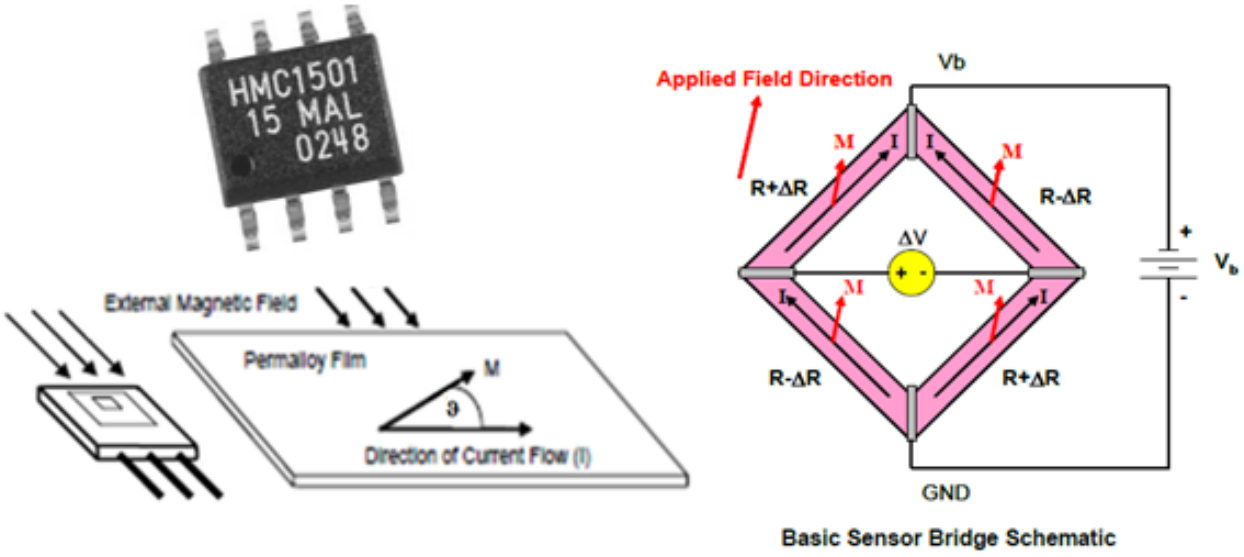

Figure 4.2 The Honeywell HMC 1501

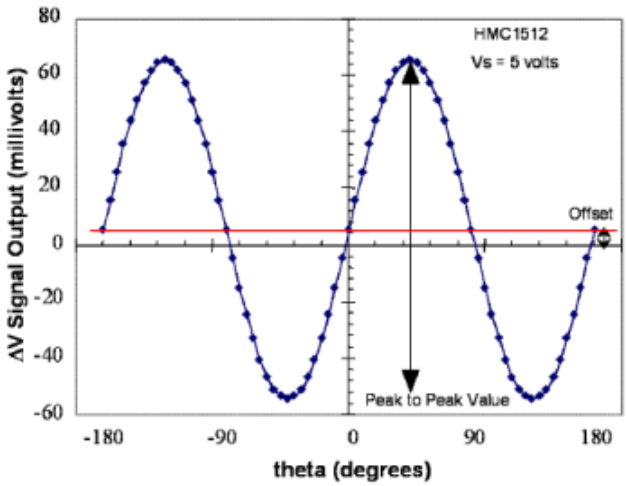

Figure 4.3 HMC1501 Signal output in function of theta

By placing the sensing element beside a permanent magnet and having a ferromagnetic object (like a blade) passing in front of it, there will be a distortion of the magnetic field. This result in a change of Theta, therefore in the sensor output. This concept is schematized in figure 4.4 and it was already verified by Pavel Procházka [61]. In fact, figure 4.5 reports the output signals of a magnetoresistive sensing element at the blade passage (figure 4.5 left) and in case of clearance variation (z) between the blade tip and the sensor head (figure 4.5 right).

This is the only reference that has been found so far using Magnetoresistive sensors. He reported blade tip clearance and blade tip vibration measurements performed in a steam turbine. Starting from the state of the art on magnetoresistive probes, this project had the aim to further investigate on the capabilities and the limits of the magnetoresistive elements in turbomachinery application. The purpose was to better understand how to build a magnetoresistive probe for accurate and repeatable measurements, improve its performance and realize a simultaneous real-time BTT and BTC measurement system.

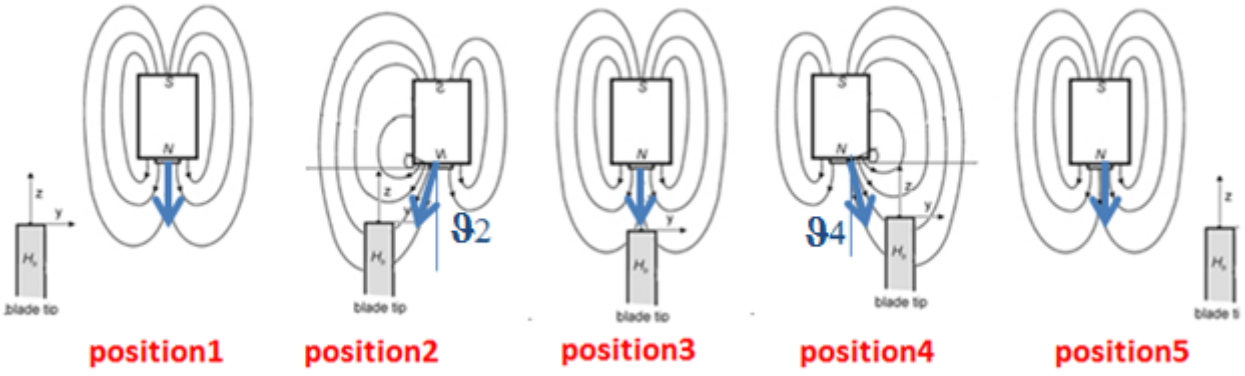

Figure 4.4 The sensor working principle

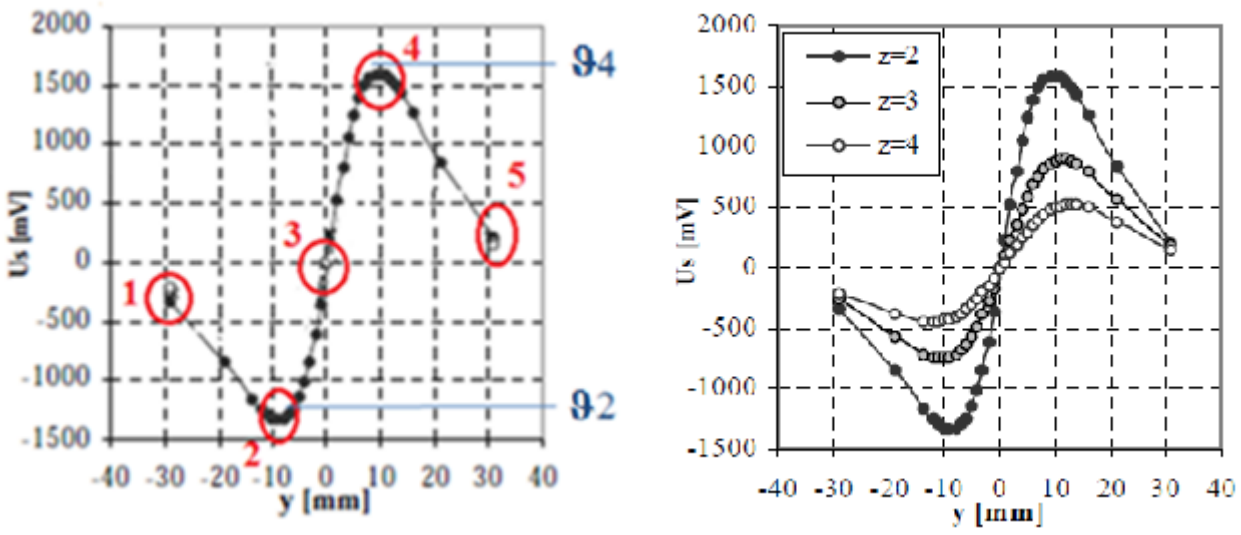

Figure 4.5 Left: Typical output value experimentally observed; Right: Sensor signal change with the clearance [41]

The basic configuration to realize a magnetoresistive sensor is made of the sensing element and a permanent magnet. Anyway, moving the magnet around the sensing element, the output signal changes. Moreover, using stronger magnet or placing the magnet with different polarization directions, the output signal, for the same blade passing condition, vary as well. This is normal because, modifying the magnet position and strength, the change in the direction of the magnetic field seen by the sensing element is different.

These aspects gave reasons to realize an optimization of the sensor components layout. A simple test bench was realized and the result are reported below. In the appendix F all the specifications are collected.

4.3 Design of the sensor

To find the best layout of the components of the probe a test bench (figure 4.6) was realized. It has a two blades rotor driven by an electric motor. A magnetoresistive sensing element HMC1501 was placed on a fixed support in central position, facing the rotating blades. Behind, an x-y sliding system was realized with two micrometric linear sliders OWIS MT 60-UM. It was used to place different magnets in different positions around the sensing element. Test were conducted with two magnets: “S-04-25-N” (cylindrical shape) and “W-05-G” (cubic shape).

For every position of the magnet, the signal corresponding to a blade passage was acquired. The optimum layout is the one corresponding to the output signal with the highest amplitude.

The micrometric slider adopted are made of a non-metallic material, in order to do not affect the magnetic field of the magnet. For the same reason, all the other components used are also made of aluminium or plastic materials. Two sliders were used, mounted at 90° respect each others, to move the permanent magnet on several points of a 2D investigation area. The grid of measurement points is illustrated in Figure 4.7. The signals were stored with the Picoscope 4424 (4 channels, 12 bits resolution, 20 MS/s, 32 MS buffer memory).

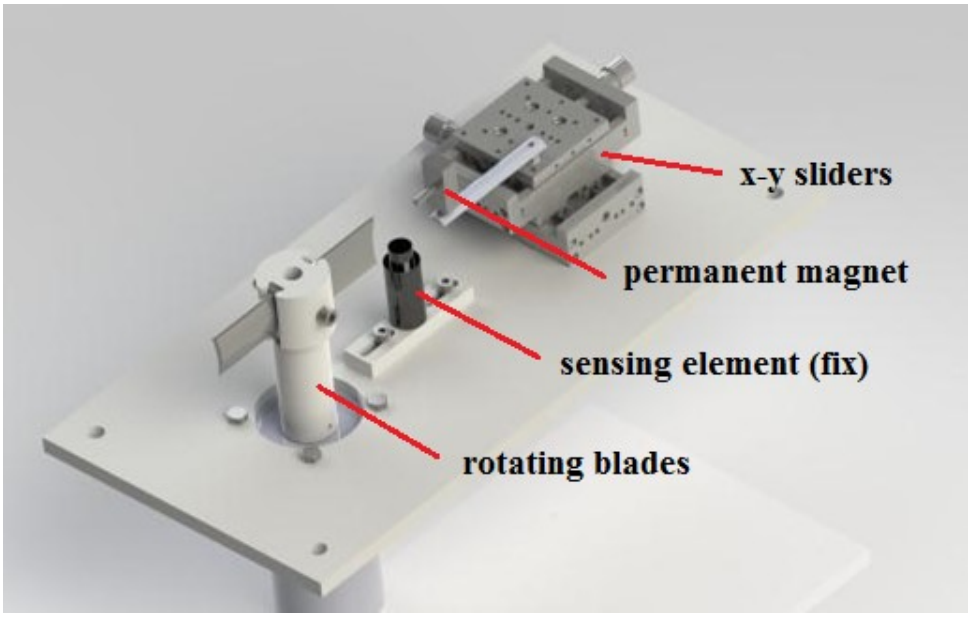

Figure 4.6 Test bench for the optimization of the sensor components layout

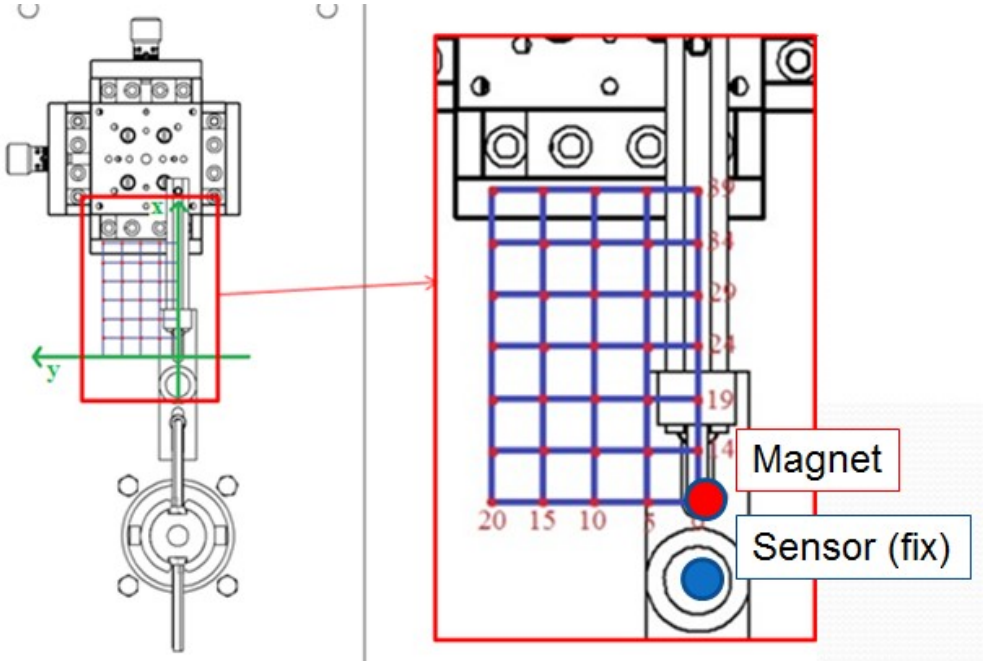

Figure 4.7 Top view of the bench and measurement grid

Measurements with the cylindrical magnet “S-04-25-N”

Table 4.1 lists all the peak to peak values (Voltage in [mV]) of the signals acquired at various magnet positions. The coordinate system is the one displayed on the measurement grid of figure 4.7. The x axis corresponds to a vertical displacement and the y axis to the horizontal direction. The sensing element was placed at the coordinate (x;y) = (0;0) mm and the first measurement point was taken with the magnet at (x;y) = (9;0) mm. Figure 4.8 shows all the peak to peak values in a contour plot.

		y axis				
	position [mm]	**20**	**15**	**10**	**5**	**0**
x axis	**39**	39,50	39,25	35,32	32,25	30,28
	34	39,80	39,70	37,15	34,02	32,30
	29	37,24	37,03	35,82	34,19	33,45
	24	20,08	28,43	30,33	31,08	31,75
	19	14,34	14,60	20,69	24,77	27,00
	14	23,75	8,80	9,38	16,50	19,95
	9	34,95	22,42	5,09	7,76	11,02

Table 4.1 Peak to peak output signal values

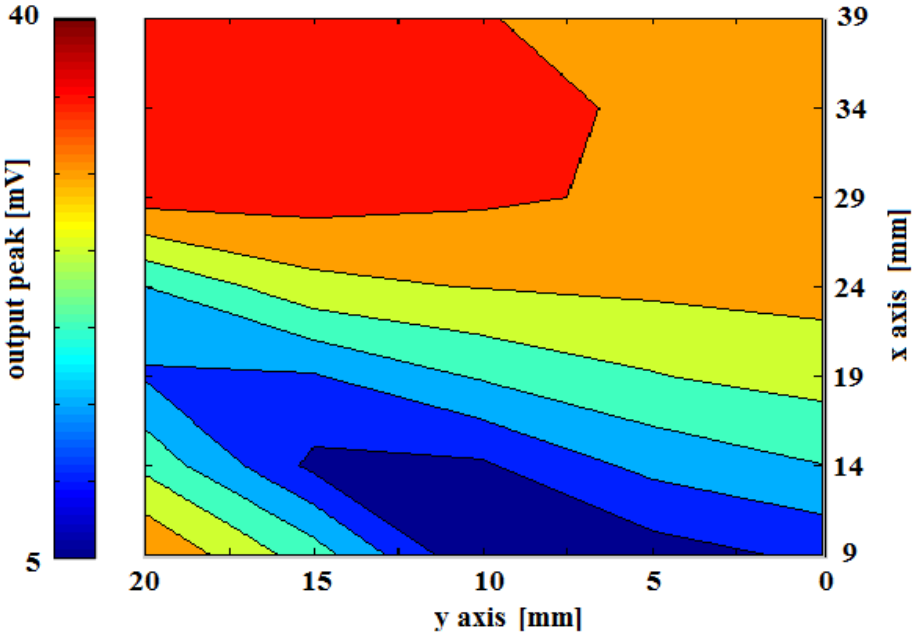

Figure 4.8 Peak to peak output signal values

The maximum output amplitude was obtained at the position (34,20) mm with a peak to peak value of 39.8 mV. The data stored in Table 4.1 are displayed in three different colors because a change on the signal shape has been also observed and details are reported in the appendix, part F.

Measurements with the cubic magnet "W-05-G"

All the measures were repeated with the second magnet. The output values have shown only small changes. The maximum amplitude was obtained at position (18, 20) mm with a peak to peak value of 36.1 mV.

4.4 The first sensor prototype

According to the results of paragraph 4.3, the best layout to realize the sensor is the one with the cylindrical magnet "S-04-25-N" placed at x = 34 mm and y = 20 mm from the sensing element. To reduce the size of the probe, it was decided to have a symmetric layout with all the components on the same axis y = 0. Therefore, the first magnetoresitive sensor prototype (figure 4.9) was built with the cylindrical magnet "S-04-25-N" placed at x = 29 mm from the sensing element.

It is made of an 8 mm outer diameter brass pipe, with the sensing element placed inside, at the top, as it is possible to see from the image below. At 29 mm follows a permanent magnet connected with a screw. The latter allows to change the relative distance between the magnet and the sensing element, in case of necessity.

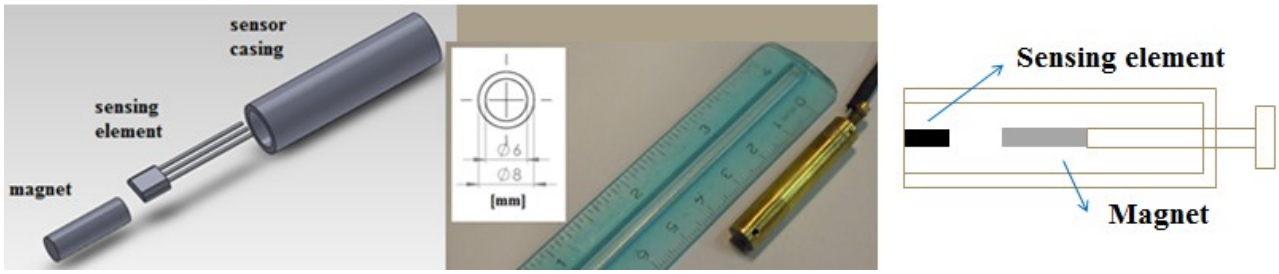

Figure 4.9 The first magnetoresistive sensor prototype

4.5 The mathematical model of the sensor

During the sensor design phase several tests were performed to find the best probe configuration. Hence a large number of experimental data was collected. Therefore, it was developed a mathematical model of the probe and validated with the experimental results. The big advantage of

a FEM model is to have a reference when trying to develop new sensor configurations or investigate on new applications.

The magnetic field is generated by the NdFeB permanent magnet in shape of a rod having diameter 4 mm, height 12,5 mm, weight 1,2 g, Curie temperature 310 °C, magnetic remanence from 1.29 to 1.32 T, coercive magnetic field strength from 860 to 955 kA/m. The direction of the magnetic induction changes when the position of the ferromagnetic iron blades changes. If the sensor bridge is placed in a position where the change of the angle of the magnetic induction is relevant, it gives a sensitive output variation and small noise, resulting in high Signal to Noise ratio.

The FEM analysis of the prototype was performed using the numerical code Ansys Maxwell Rel 14.5. It was modeled the 3D geometry of the compressor blade mounted on the test bench shown in figure 4.6, and the permanent magnet described above. These objects are included in an air cube where the boundary conditions have been imposed along its outer part. In particular it was imposed the parallel flux condition. The air cube edge is ten times longer than the length of the blade. It was seen that for larger boundary region the numerical results do not change anymore. The problem geometry has been discretized using about 18,000 tetrahedral elements. In figure 4.10 is shown a particular of the blade tips volumes designed to take into account the different blade positions respect to the permanent magnet position. For each blade position the corresponding volume is defined as steel, while the others volumes are defined as air. The average relative magnetic permeability of the blade steel has been assumed equal to 120. This value has been deduced by static measurements performed in laboratory [62-64]. In the volume of the permanent magnets the material parameters used were the residual magnetic induction and the coercive magnetic field. The permanent magnet has been paced at d = 29 mm respect to the blade tip as schematized in figure 4.10. The magnetoresistive sensors can be placed at different positions between the compressor blade and the permanent magnet. In order to optimize the sensors number and their positions it was computed the three components of the magnetic induction in 1000 points along the distance d. This simulation has been repeated for 21 values of the blade angle ϑ from -20 degrees to +20 degrees with a step of 2 degrees. In this way we have generated a map of the magnetic induction change when the blade moves, rotating in front of the permanent magnet. This map is shown in the figure 4.11. The magnetic induction change is represented by the so called magnetic induction deflection, that is the variation of the angle of the magnetic induction vector M during the blade rotation. This deflection is related to the x-y plane, and the deflection respect the z axis is negligible. The results presented in the figures confirm that the higher sensitivity can be obtained using a sensor positioned

in proximity of the blade tip when it faces the permanent magnet. More precisely, in figure 4.11 left is reported a comparison between experimental and numerical data of the magnetic distortion at the blade passage.

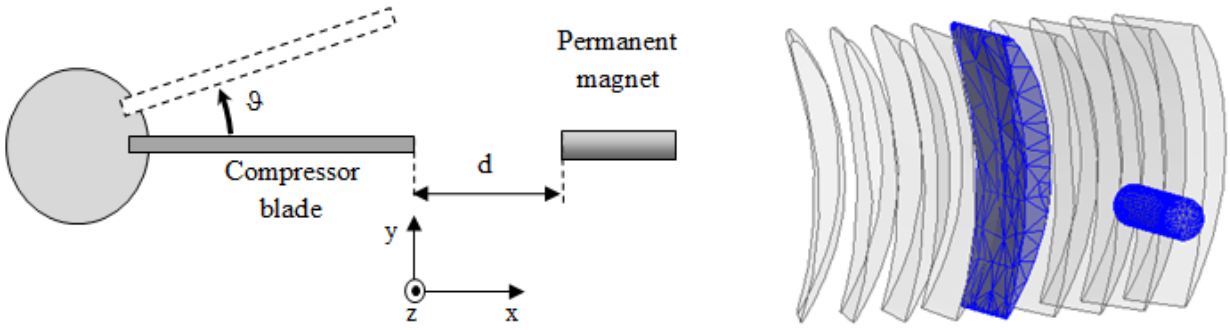

Figure 4.10 Typical modelling FEM mesh at different blade positions

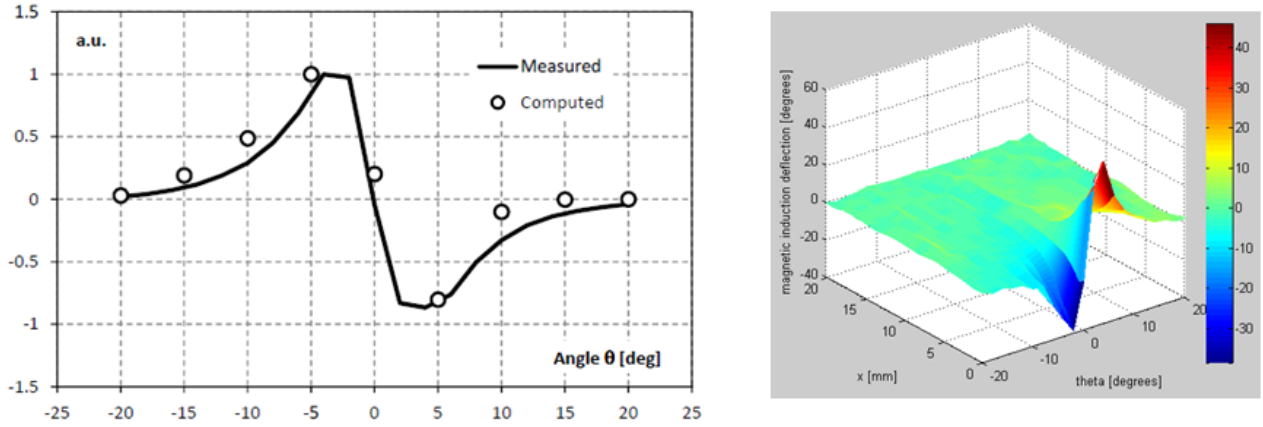

Figure 4.11 The magnetic induction change at the blade passage

4.6 The basic electronic board

A preliminary electronic board was developed following the electronic circuit suggested by Honeywell in the datasheet [60], as in figure 4.13.

It correctly works for static measurements and low dynamic conditions. Nevertheless, when trying to use magnetoresistive sensors in high speed turbomachines with high blade passing frequency, it is highly recommended to develop a dedicated electronic.

In this work several modifications were made to the basic electronic board in order to avoid bandwith limitations and add amplification, filtering and signal conditioning stages.

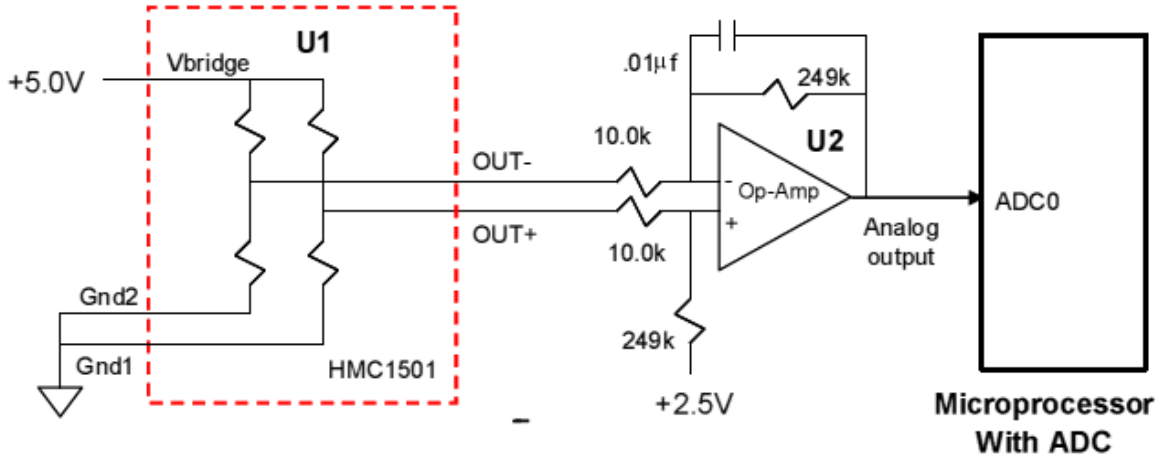

Figure 4.12 Basic electronic circuit for static measurements

4.7 The Universal Calibration Bench for BTT & BTC systems

A light and handy test bench was manufactured by the University of Perugia for the characterization of sensors for rotating components [67]. As it is possible to see in figure 4.13 it is composed of an electric motor that drive a rotating disk of diameter 100 mm having four small plates of steel (thickness 1 mm) every 90°. It is used to simulate the blades passages up to 25000 rpm. Around the disk there is an alluminium casing for safety reason. On the top of the casing, the sensor housing is installed on a vertical linear slider fixed to the frame. In this way, it is possible to vary the gap between the sensor head and the tip of the thin steel plate.

The first version of the test bench was upgraded according to the idea of the blade motion decomposition published in [57]. It was recently reported by Tomassini et al [68]. Instead of having fixed casing sensors and vibrating blades, the innovative approach consist in letting the sensor vibrate while non-vibrating blades are kept in rotation. The biggest advantages of this system are the possibility to know the expected measured vibrations and the flexibility in changing the test conditions. It represent a Universal Calibration Bench for any type of sensors used in BTC & BTT systems.

First of all, a new disk was designed. The latter is provided of 24 symmetrically distributed holes to mount properly shaped and “rigid - blades”, fixed at the disk with screws (figure 4.14).

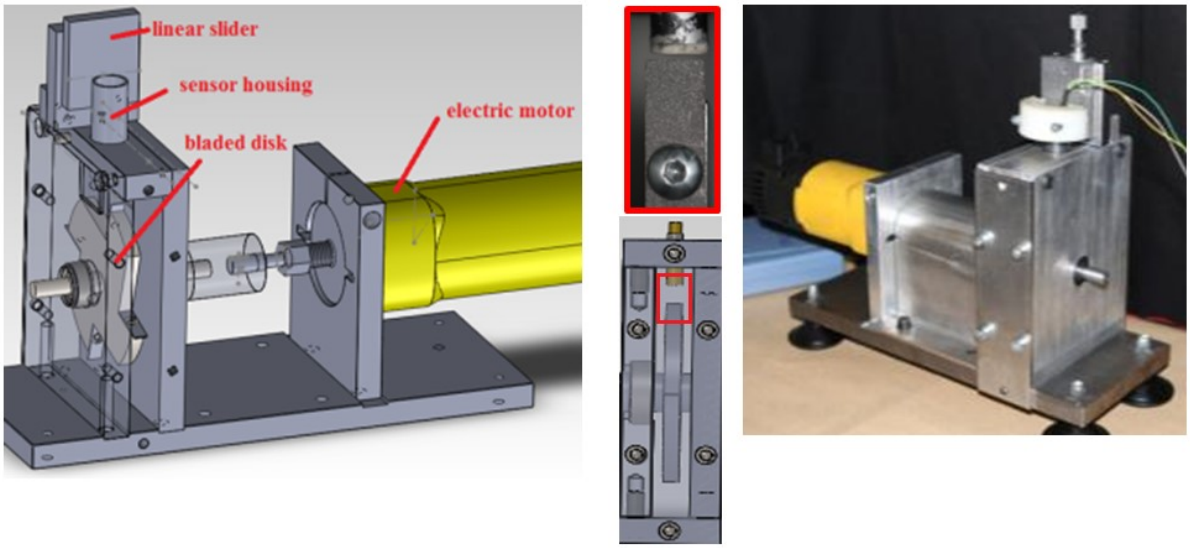

Figure 4.13 The test bench for the sensor characterization – version 1

Figure 4.14 The new disk and the little blade

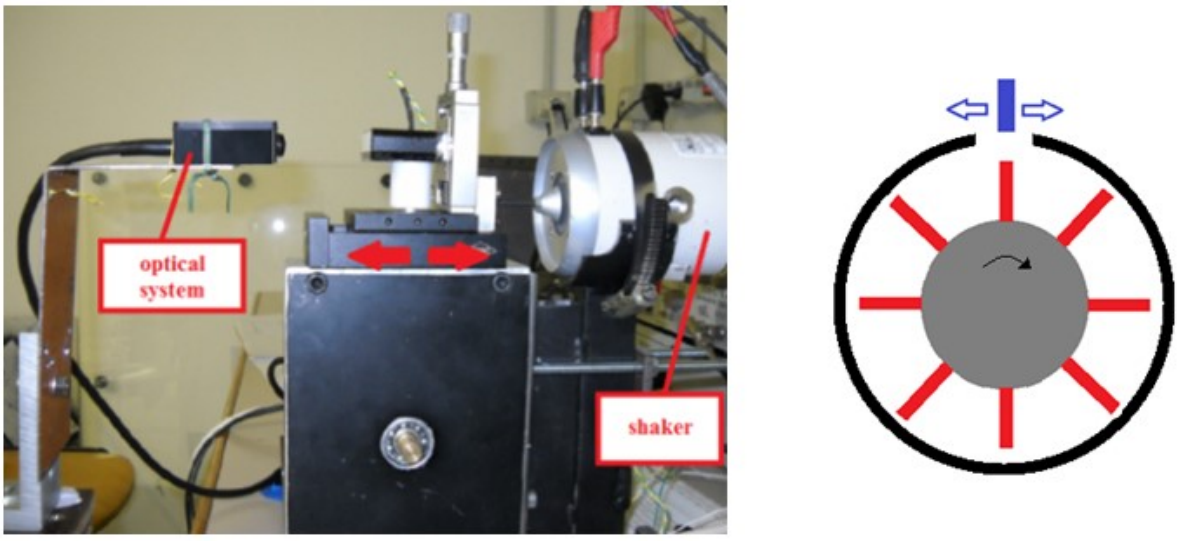

Figure 4.15 The bench equipped with a sensor shaking system

Subsequently, in spite of having a vibrating blade and a fix sensor to acquire the blade passing pulse, the idea is to let the sensor vibrate at a known frequency and amplitude, meanwhile the rotor with the little blades, supposed to do not vibrate, is spinning. To impose a known vibration to the probe, the test bench was equipped with a shaker, as in figure 4.15. The linear slider where the sensor is mounted is connected to the shaker and a signal generator makes it possible to impose a vibration of a certain frequency and amplitude. The maximum achievable displacement at different frequencies has been experimentally obtained by means of an optical displacement measurement system (Appendix E, Figure E1). The vibrating system can achieve a maximum displacement of about 2.3mm up to 30Hz, than the mass of the moving parts become relevant and the system response decrease with the square of the frequency.

All the components were grouped together with a compact frame, resulting in a Universal Calibration Bench for any type of sensor for BTC & BTT systems. As shown in figure 4.16 and 4.17, the facility is made of: a data acquisition system (DAS), the electronic board, a signal generator connected to the amplifier of the shaker, the latter fixed to the moving sensor housing placed at the top of the test bench.

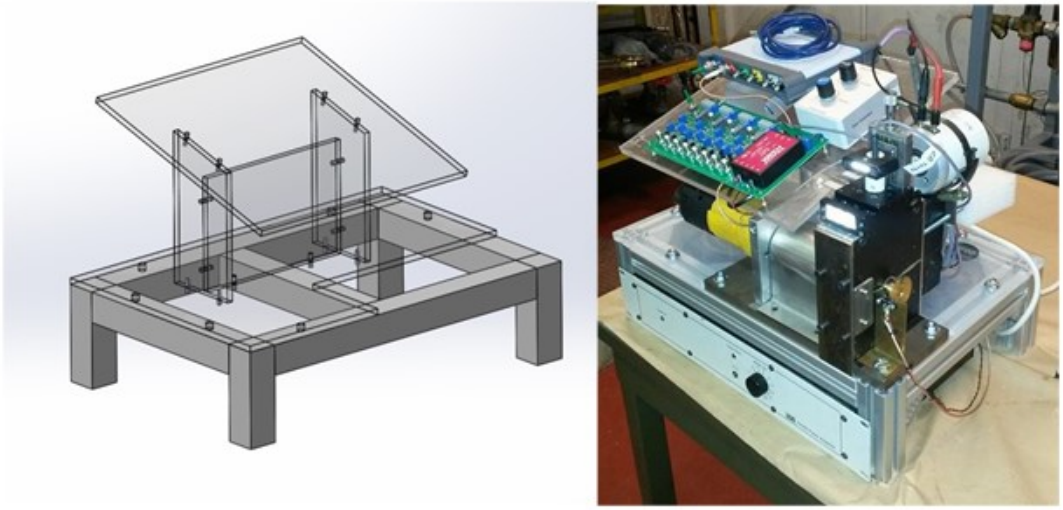

Figure 4.16 Left: the frame. Right: the assembly of the universal calibration bench

The displacement of the sensor under calibration is monitored by a displacement probe with high resolution mounted on the fixed frame. It was calibrated with an external optical system (figure 4.15) with a resolution of 3 µm.

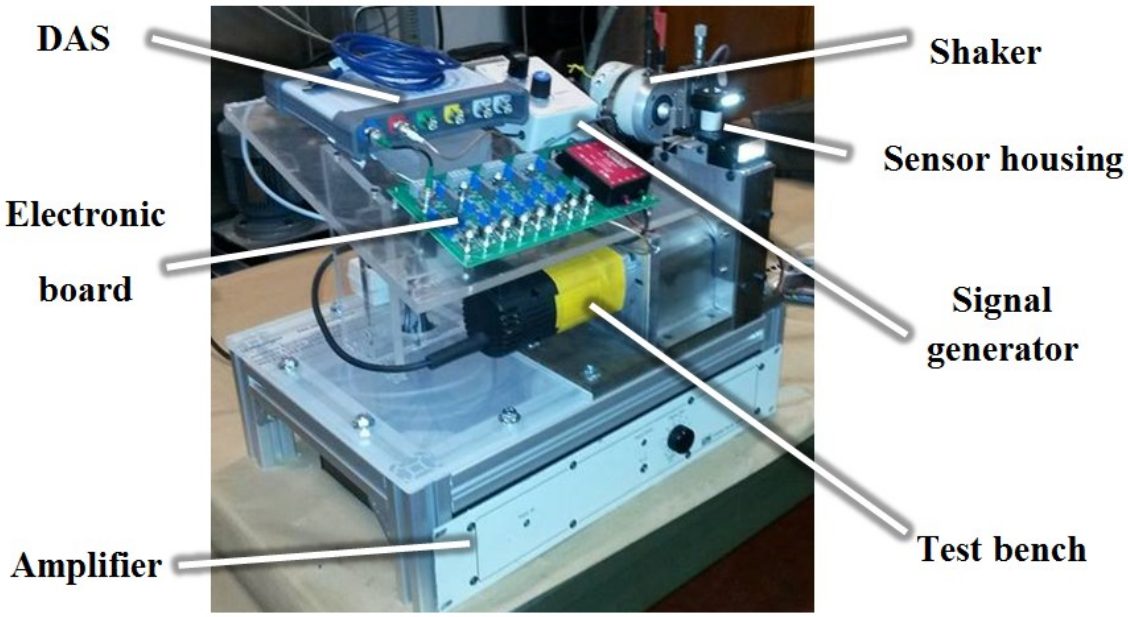

Figure 4.17 The Universal Calibration Bench for BTC & BTT systems

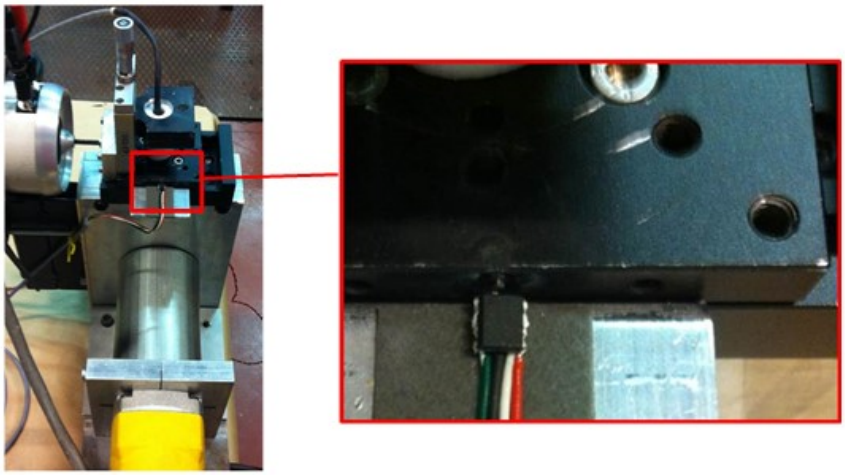

Figure 4.18 The displacement monitoring sensor of the shaking system

4.8 Design of the post-processing software

As presented in chapter 3, a BTC & BTT software must extract the key parameters from the sensor signals to give information on the current blade tip gap and the presence of blade vibrations. These routines already exist and are commercially available. The data processing in tip-timing is complex, is directly affecting the results and is very difficult to find references because every company has its method and it keeps it secret. Nevertheless, this aspect can still be improved developing new methods of data processing.

In the frame of this research project, it was developed a post-processing software in Matlab for the analysis of the magnetoresistive signal. It should be considered that the aim was not to improve the existing professional and real-time routines, but to have a robust data processor to evaluate the performance of the innovative magnetoresistive sensors for turbomachinery testing. Therefore, below the main phases of the algorithm developed are only summarized to give an insight to the readers.

The algorithm is divided in three main parts: reading, calibration and processing.

The first phase opens the signal, subdivides it in revolutions, acquires the settings of fundamental parameters like the sampling frequency, the rotor radius, the number of blades, etc.. The calibration routines check if the signal has errors. In fact, it happens that there is a missing blade, the signal is noisy and requires a smoothing procedure, etc.. Finally, the processing routines are the core of the software.

The processing procedure is divided in seven sub-routines:

- Calculation of the maximum peak values
- Calculation of the zeros
- Interpolation
- Integration
- Extrapolation of the TTOAs
- Calculation of the blade displacement samples
- Plotting of the results

1.Calculation of the maximum peak values

A typical output signal corresponding to a blade passage was shown in figure 4.5. Concerning the clearance measurements, the software extracts a key parameter (in this case the maximum peak value) for every pulse generated by every blade passage during the acquisition. Figure 4.19 shows a typical signal collected in the lathe and representing few rotations of a gear at low speed (blue line). Sometime there is also a reference signal, one per revolution (1/Rev or OPR), here represented by the red line.

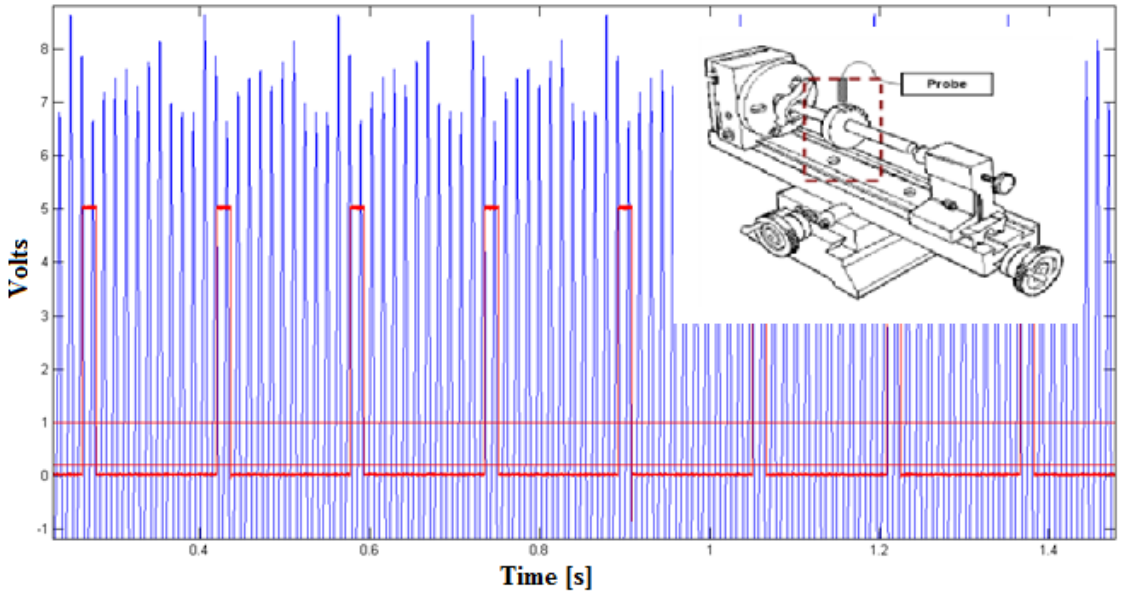

Figure 4.19 Typical signal collected with the sensor prorotype and a gear rotating in the lathe

Once a threshold has been defined by the user, the program split the whole signal in the upper and the lower part. At that time, it retrieves each max value, for every peak of every blade, as in figure 4.20. When the calibration curve of the sensor is known, is possible to convert the measured volts in millimiters of blade tip gap.

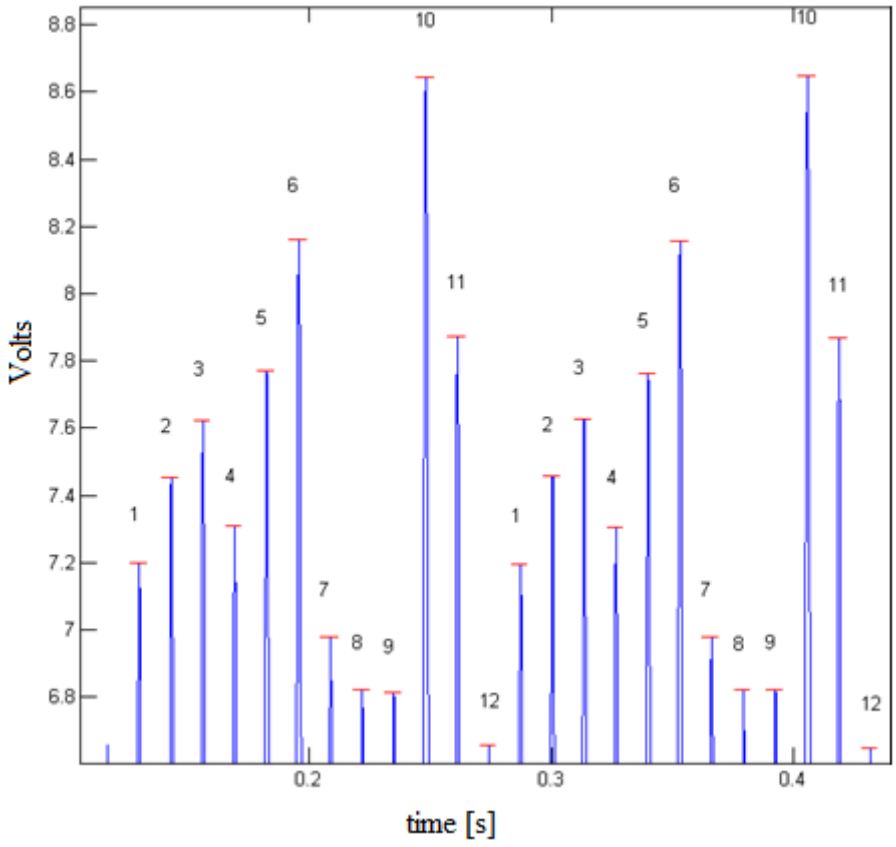

Figure 4.20 Detail of the calculated maximum peak values

2.Calculation of the zeros

As introduced in chapter 3, the fundamental parameter to extract from a tip-timing signal, is the blade time of arrival (TOA). Having signals as figure 4.5 right, it can be noticed that, whatever is the clearance, all the pulses passes through the zero voltage point. This point is not affected by clearance variations and it is a good representative of the TOA. Figure 4.21 illustrates a typical raw signal and the relative TOA for every blade. The signal around the zero voltage value is reconstructed by a fitting curve to avoid the noise and to increase the calculation accuracy.

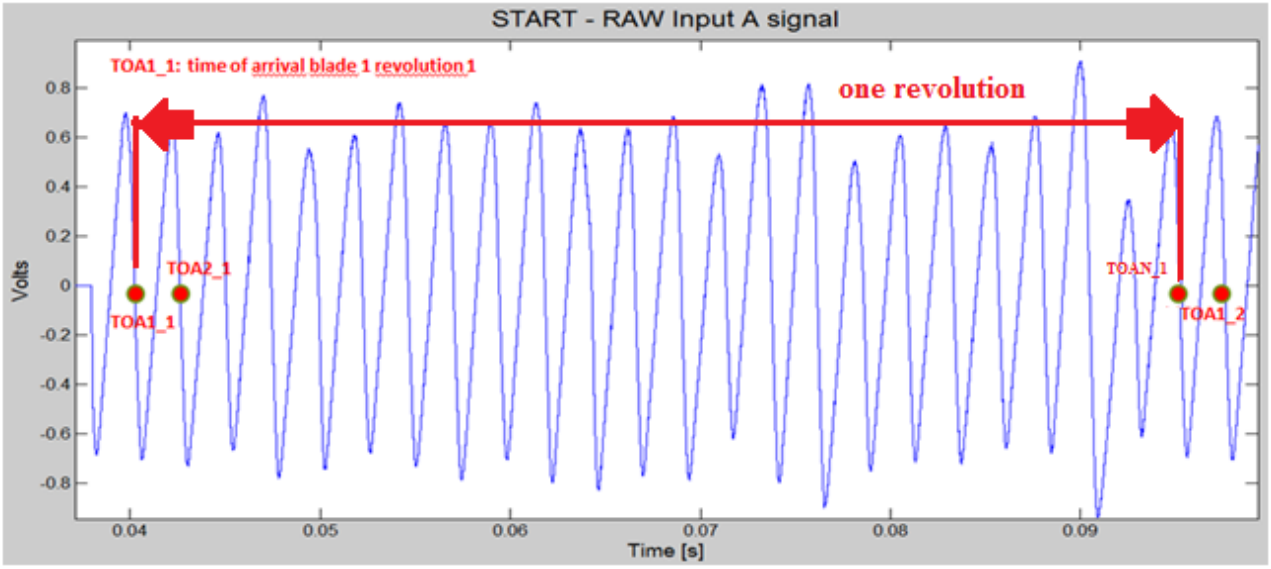

Figure 4.21 Example of TOA calculation

3.Interpolation

Once the TOAs of one revolution are known, the next step is the calculation of the Δt between each TOA. The values Δt_i in one revolution and the mounting angles of the blades $\Delta\theta_i$ are used to calculate the samples of the angular velocity (ω_i) over one revolution, as follows:

$$\omega_i = \frac{\Delta\theta_i}{\Delta t_i} \qquad i = 1 \ldots N \qquad \text{(where N is the number of blades)} \qquad (4.2)$$

The Δt_i and the ω_i are fitted with a weighted polynomial, to know the trend of ω in function of the time (ω(t)).

4.Integration

The function ω(t) is integrated over the period of one revolution to obtain the angular position of the blades in function of the time: θ(t).

5.Extrapolation of the TTOA

At this point, it is possible to extrapolate the theoretical time of arrival (TTOA) of the incoming blade. For instance, TTOA1_2 will be the expected time of arrival of blade 1 at the revolution 2.

6.Calculation of the blade displacement sample (S_i)

The incoming blade is expected to arrive at the TTOA extrapolated. Its real TOA will be calculated and equal to the time corresponding to the zero crossing voltage. Then, the blade displacement sample S_i will be:

$$S_i = \begin{cases} S_i = 0 & \text{(in case of no vibration } \rightarrow \text{ TTOA } = \text{ TOA)} \\ S_i = (\text{TTOA} - \text{TOA}) \cdot \omega \cdot \text{R} & \text{(in case of vibration } \rightarrow \text{TTOA} \neq \text{TOA)} \end{cases}$$

(4.3)

For every incoming blade signal, the ω(t) is upgraded of one point, it is newly integrated, the new TTOA is extrapolated and the next blade displacement sample S_i is calculated. This iteration is schematized in figure 4.22. It stops at the end of the acquisition. Finally the results are plotted.

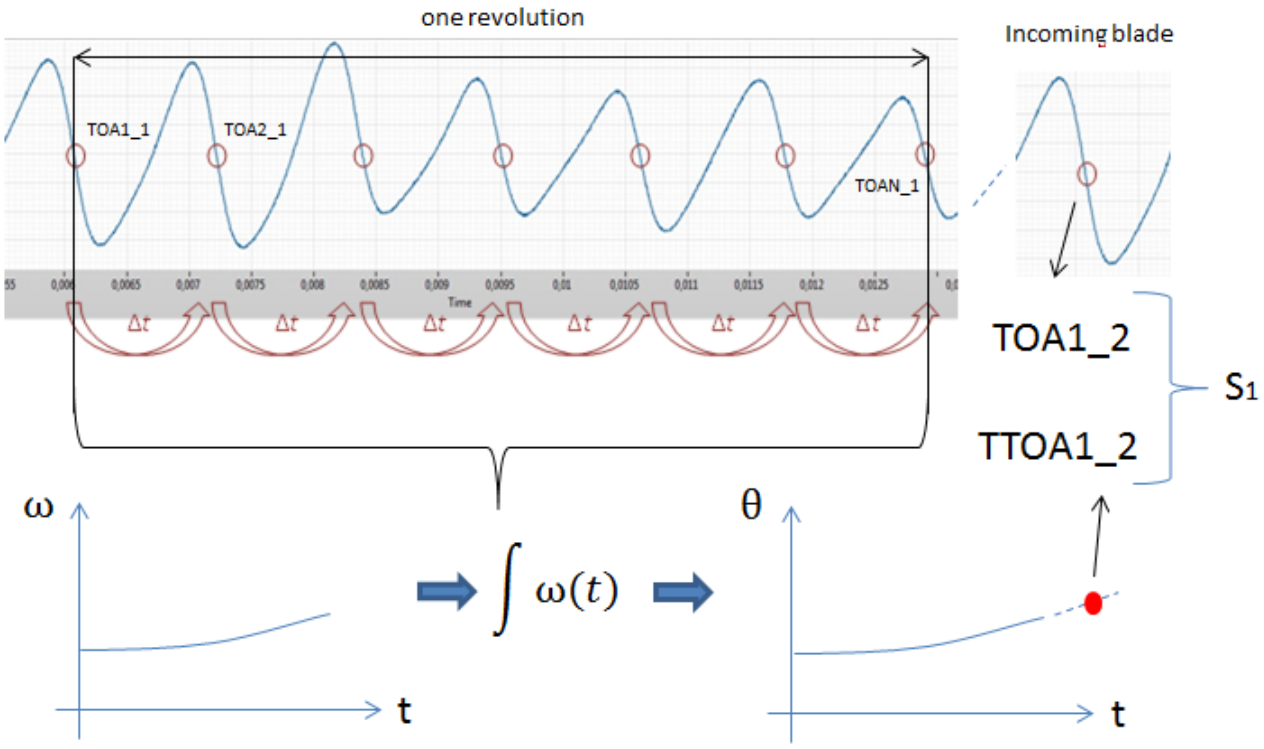

Figure 4.22 Scheme of the TTOA and TOA calculation

7. Plotting of the results

The last part of the algorithm regards the plotting of the results. The software plots the individual blade displacement measured for every blade and the waterfall, which is an ensemble plot of the displacement of every blade. Figure 4.23 and 4.24 shows two example of plotting of results which will be explained in the following chapters.

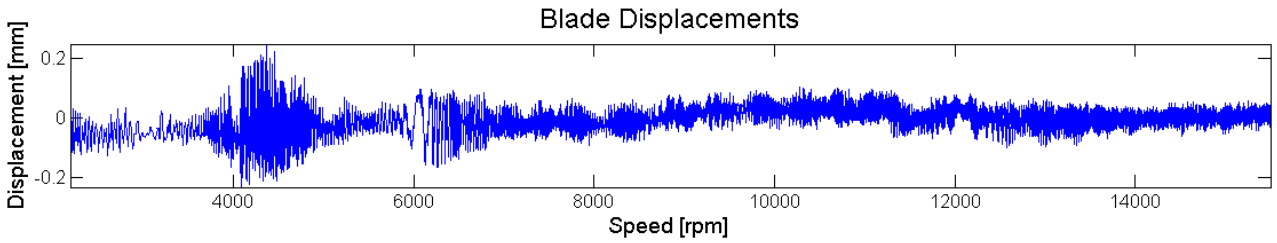

Figure 4.23 Example of measured blade displacements

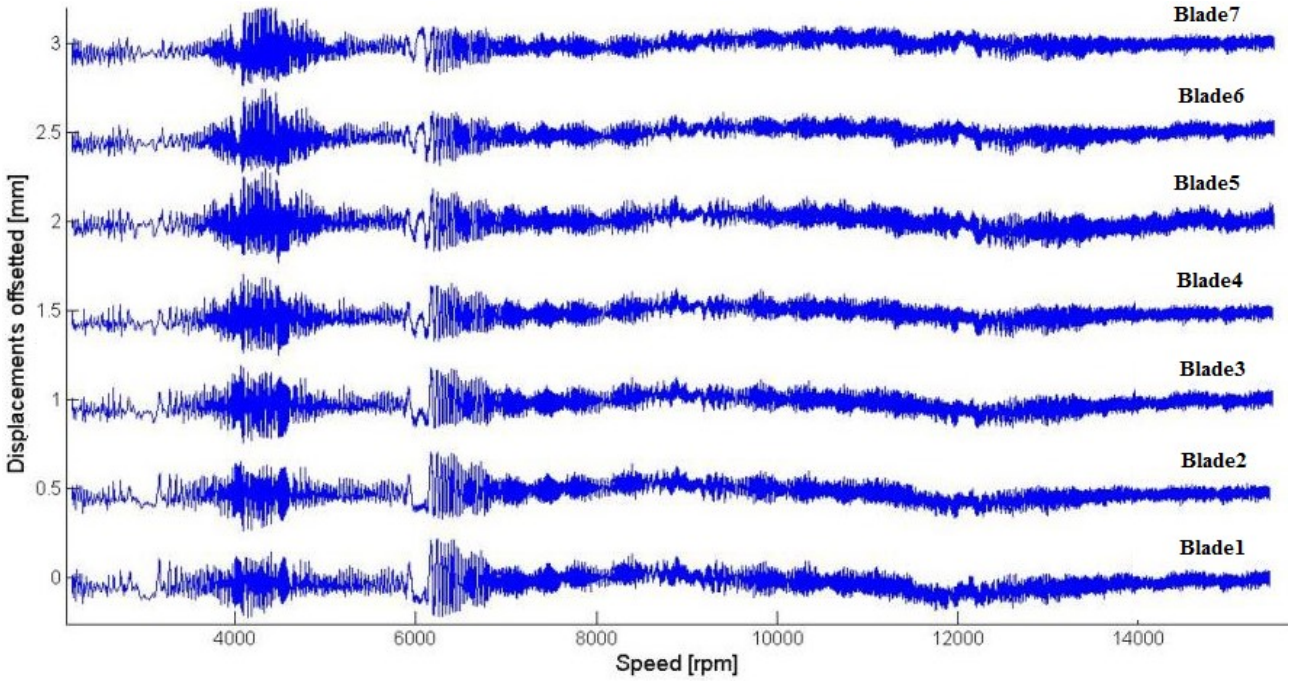

Figure 4.24 Example of waterfall of the measured blades displacements

4.9 Conclusions

Several problems were fixed while developing and testing the system. This chapter summarized the design phase of the different components of the system and the following conclusions can be drawn:

- The experimental investigations have shown that, by changing the magnet position, big variation results both in the signal shape and in the peak to peak value. A database of different possible configurations was stored. Varying the magnet strength instead, the output signal do not change so much.
- Concerning the dedicated electronics, to avoid bandwidth limitations it is important to find the right compromise for the gain of the system.

5 Blade tip clearance measurements

5.1 Introduction

The importance of monitoring the blade tip gaps and the fundamental parameters involved were described in chapter 2 and 3. In this chapter the characterization of the magnetoresistive sensor and its calibration curve for clearance measurements are reported. The performance of the probe were evaluated on a static test at the blade passage, then a preliminary test was performed in a lathe using a gear. Finally, the calibration curve of the magnetoresistive sensor for clearance measurements was obtained in the Von Karman R2 compressor rig.

5.2 Characterization of the magnetoresistive sensor at the blade passage

5.2.1 Test setup and methodology

The passage of a blade in front of the sensor at different gaps was studied in a static test. A shaft with two compressor blades was mounted in a rotary slider with a resolution of 1°, facing the magnetoresistive sensor installed in a linear slider with a resolution of 10 µm. The sensor axis was aligned with the blade axis at 0° on the rotary slider. A scheme is illustrated in Figure 5.1 left. The blade passage was discretized and studied in the angular range [-20 + 20]° with an angular step of 2°. The measurements were repeated for different gaps (sensor head – blade tip): [0.5, 1, 1.5] mm. At every fixed position, the output DC signal was acquired and represents one point of the resulting fitting curves of Figure 5.1 right.

5.2.2 Results

Figure 5.1 shows the typical pulses observed at the blade passage at different gaps. The variation of the clearance results in a signal amplitude variation: the bigger the gap, the smaller the signal amplitude. Therefore, the clearance between a passing blade tip and the sensor head can be monitored by the maximum peak value or the peak to peak value of the output signal. The latter is not symmetric, most probably because of asymmetries in the sensor prototype or in the blade shape. Nevertheless the peak to peak value can be used to measure the blade tip clearance and the asymmetries in the sensor can be avoided with a product engineering.

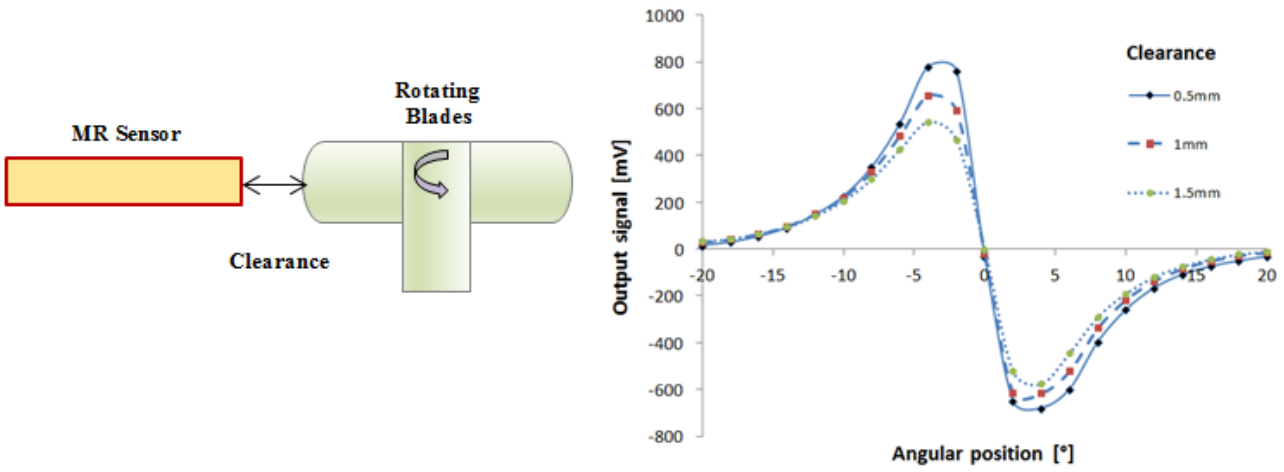

Figure 5.1 Left: scheme of the clearance test. Right: blade passage pulse at different clearances

5.3 Preliminary clearance test with a gear

5.3.1 Test setup and methodology

A preliminary test was performed using a metallic gear, with 12 teeth mounted in the lathe. The aim of the experimental investigation was to verify the repeatability of the measurements at different velocities. The magnetoresistive sensor (S1, in Figure 5.2) was placed in the moving tower of the machine and a second sensor (S2), used as OPR signal. The signals of one revolution were acquired at three different gaps between the sensor head and the tooth tip and at different velocities. In particular, the acquisitions were performed at: gap 0.1mm at 45rpm, gap 0.3mm at 500rpm and gap 0.5mm at 1000 rpm. A comparator was used as displacement monitoring system (resolution of 0.01mm). The DAS used was The Picoscope 4424 (4 channels, 12 bits resolution, 20 MS/s, 32 MS buffer memory).

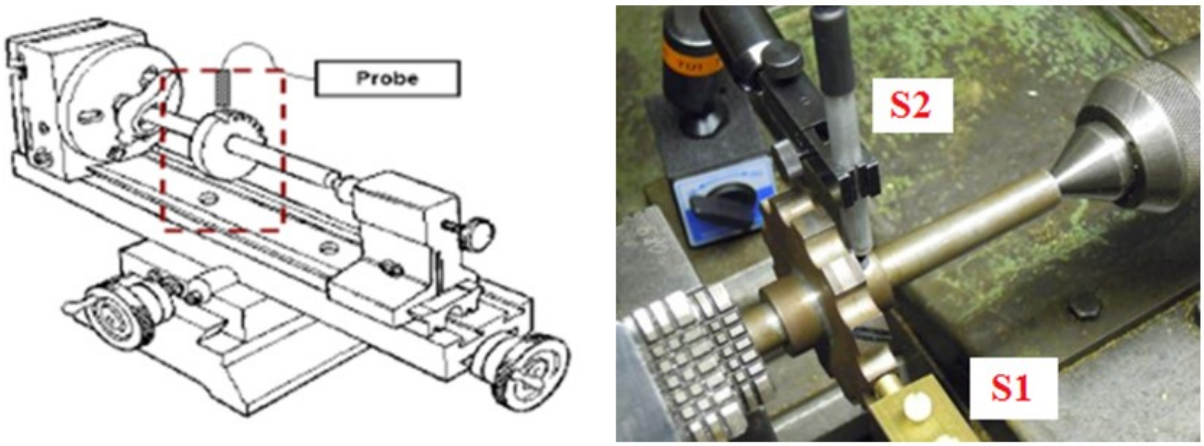

Figure 5.2 Setup of the preliminary clearance test

5.3.2 Results

In figure 5.3, there are all the 12 pulses of one revolution plotted together at the different gaps and velocities. First of all, to note that every blade gives a different output amplitude, most probably because of its magnetization feature. Nevertheless, the variation of the maximum peak values with the gap, listed in table 5.1 and plotted in figure 5.5, is almost the same despite different absolute values. Moreover there was no significant variation of the output signal with the velocity, in the speed range of the test.

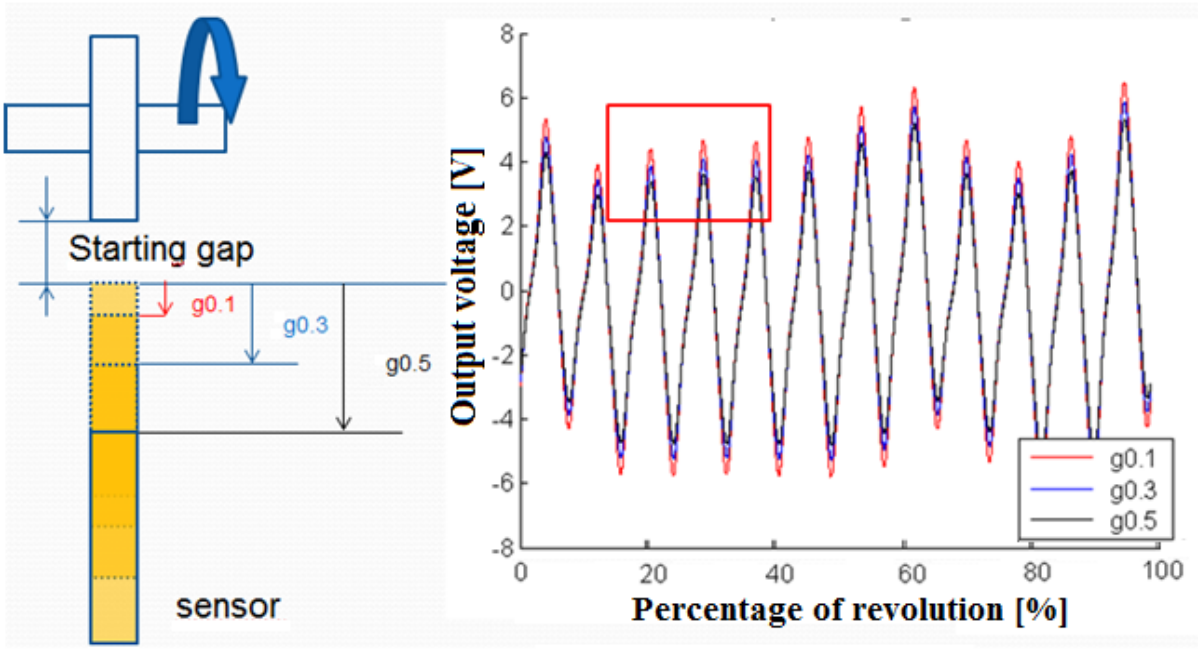

Figure 5.3 Acquired signals at different gaps and velocities

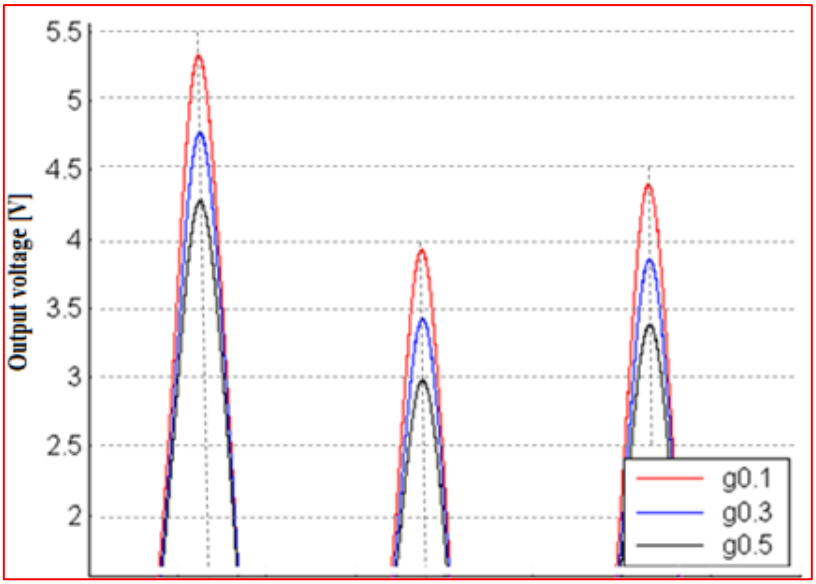

Figure 5.4 Detail of the peaks of tooth 3, 4 and 5

max peak values			
	Gap 0.1mm	Gap 0.3mm	Gap 0.5mm
Peak 3	5.26	4.7	4.23
Peak 4	3.95	3.44	2.98
Peak 5	4.39	3.81	3.31

Table 5.1 Maximum peak values variation

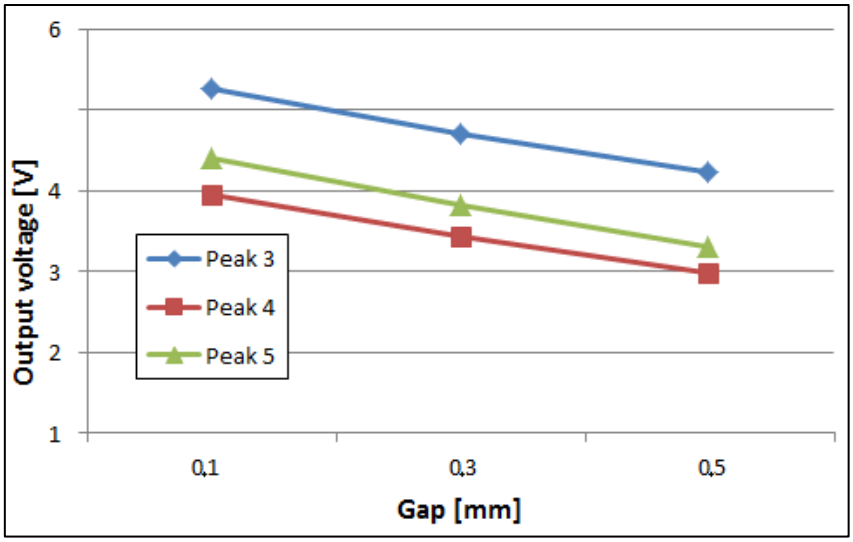

Figure 5.5 Maximum peak values variation

5.4 Clearance test in the VKI R2 compressor rig

5.4.1 Test setup and methodology

Considering that the final application of the sensor objective of this research project are clearance and vibration measurements in aero engines, the probe was finally tested and calibrated in a real turbomachine at the von Karman Institute in the VKI R2 test rig (figure 5.6). It is an high speed compressor driven by a 185kW DC motor. The rotational speed can vary up to 10000 rpm. It is a single stage axial compressor with a 400 mm diameter test section. The rotor is composed of 24 subsonic blades of the NACA 65 family with the hub radius of 100 mm and the tip radius of 200 mm. The stator is composed of 30 blades. Four circumferential locations, every 90°, allow the insertion of probes. Further details of the facility can be found in the appendix A.

The magnetoresistive sensor was installed in the calibration tower of Figure 5.7. It is equipped with a comparator to monitor the displacement of the sensor (resolution 0,01mm) and it is mounted in

one of the four instrumentation access windows of the compressor casing. The passage of one of the 24 rotor blades was extracted and studied for three velocities v = [1000 - 3000 - 5000] rpm and for different gaps in the range g = [1 – 1.5] mm with a step of 0.1mm. The gaps were changed moving the calibration tower. For every combination velocity-gap (v,g), the machine was kept at fixed speed, the sensor held at the desired gap and 30 revolutions were acquired.

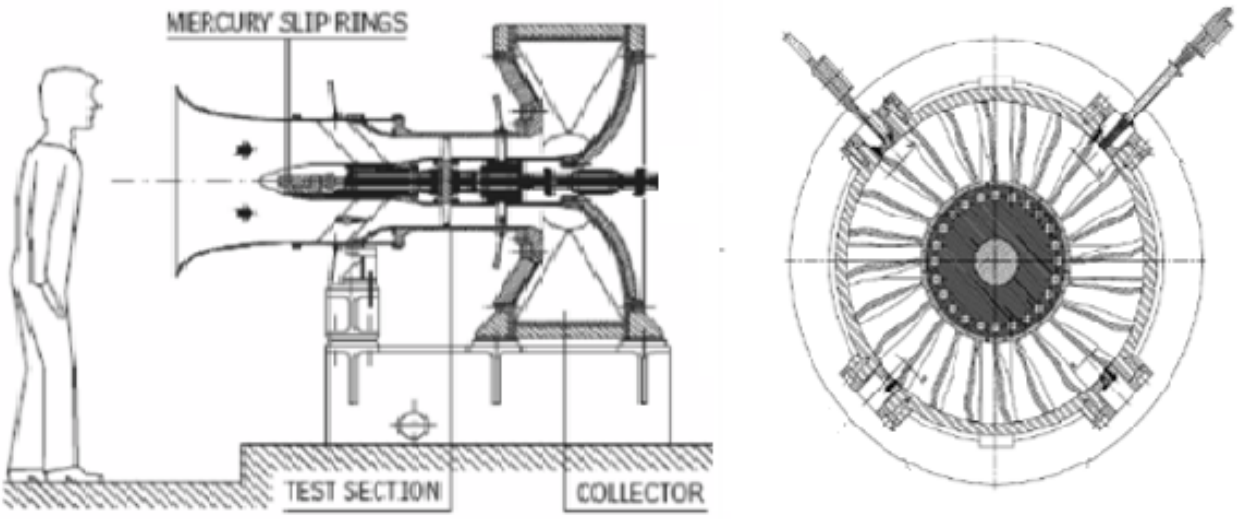

Figure 5.6 The VKI R2 compressor rig

5.4.2 The calibration curve of the magnetoresistive sensor for clearance measurements

The mean value among the 30 maximum blade signals was extracted and it corresponds to "$V_{max}(v,g)$". For instance, $V_{max}(1000,1.2)$ is the mean maximum peak value acquired at 1000 rpm and 1.2 mm clearance. The V_{max} values were normalized according to (5.1). The resulting points were plotted together and fitted with a linear function. Hence, in figure 5.8 is shown the calibration curve of the sensor for clearance measurements. As example, it also shows the 30 maximum peak values acquired at 1000 rpm and 1.2mm gap.

$$\boldsymbol{VNorm = \frac{V_{max}(v,g) - V_{min}}{V_{max} - V_{min}}} \tag{5.1}$$

Where:

$V_{max}(v,g)$ = the maximum peak value, for the combination velocity-gap (v,g);

V_{max} = the maximum among all the values $V_{max}(v,g)$;

V_{min} = the minimum among all the values $V_{max}(v,g)$;

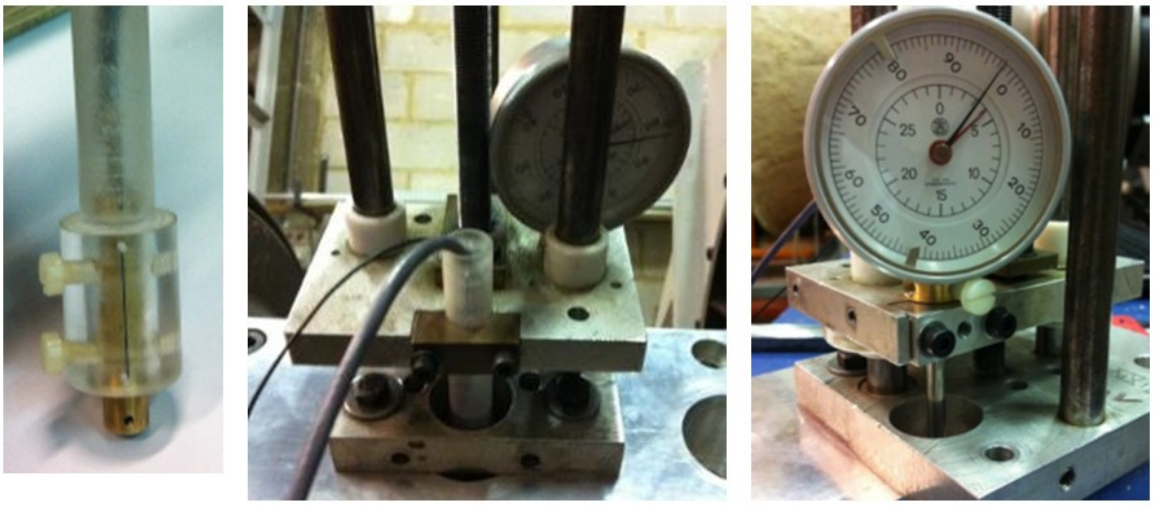

Figure 5.7 The calibration tower of the R2 compressor

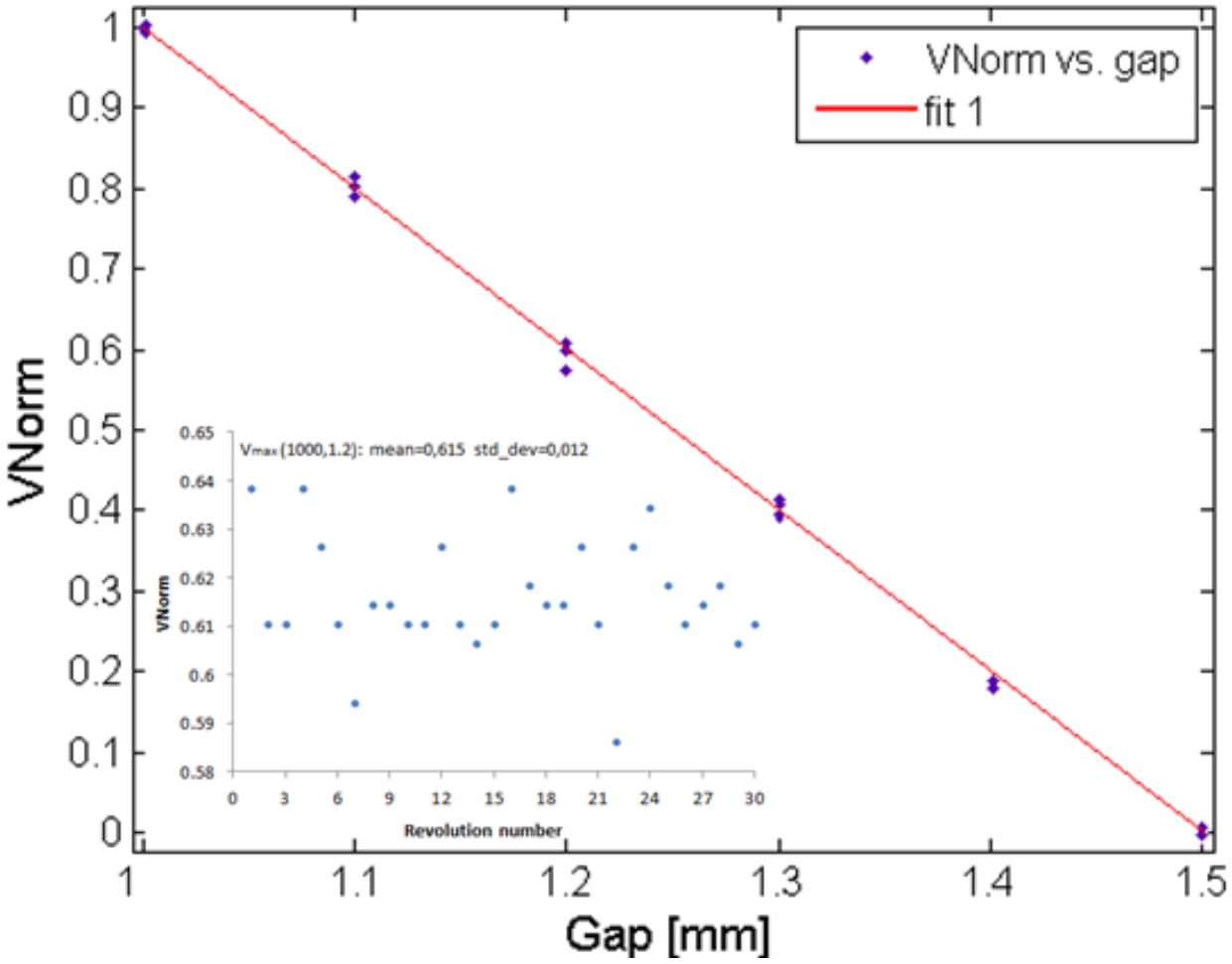

Figure 5.8 The calibration curve of the magnetoresistive sensor for clearance measurements

5.4.3 Uncertainty analysis

The expanded uncertainty U_{95} is defined as (for further details see [69] and appendix D):

$$\boldsymbol{U_{95} = \pm 2\left[b^2 + S_X{}^2\right]^{1/2}} \tag{5.2}$$

Where:

b = the systematic component of the uncertainty;

S_X = the standard deviation of the calibration data, defined as (3) – [S_X = 0.0096 mm];

$$\boldsymbol{S_X = \left[\frac{\sum_{i=1}^{N}(X_i - \bar{X})^2}{N-K}\right]^{1/2}} \tag{5.3}$$

Where:

X_i = the *i*th data point used to calculate the calibration line fit;

$\boldsymbol{\bar{X}}$ = the average of the calibration data;

N = the number of data points used to calculate S_X - [6 gaps, 3 velocities = 18 points];

K = the number of curve fit coefficients [K=1];

In this case, the systematic component of the uncertainty was given a uniform distribution. Therefore, the value of b was taken as the comparator resolution (0.01mm) divided by the root mean square of 3 [70]. The resulting expanded uncertainty is: U_{95} = ± 22 µm (20:1) within the range [1 ÷ 1.5] mm of gap range.

5.4.4 Results

A good repeatability was seen in the static and dynamic tests reported. The blade tip clearance can be measured by means of the maximum value of the sensor signal peak. No significant dynamic effects were observed. Moreover, the accuracy of the new magnetoresistive probe is in line with the main types of sensors often used in BTC systems [71].

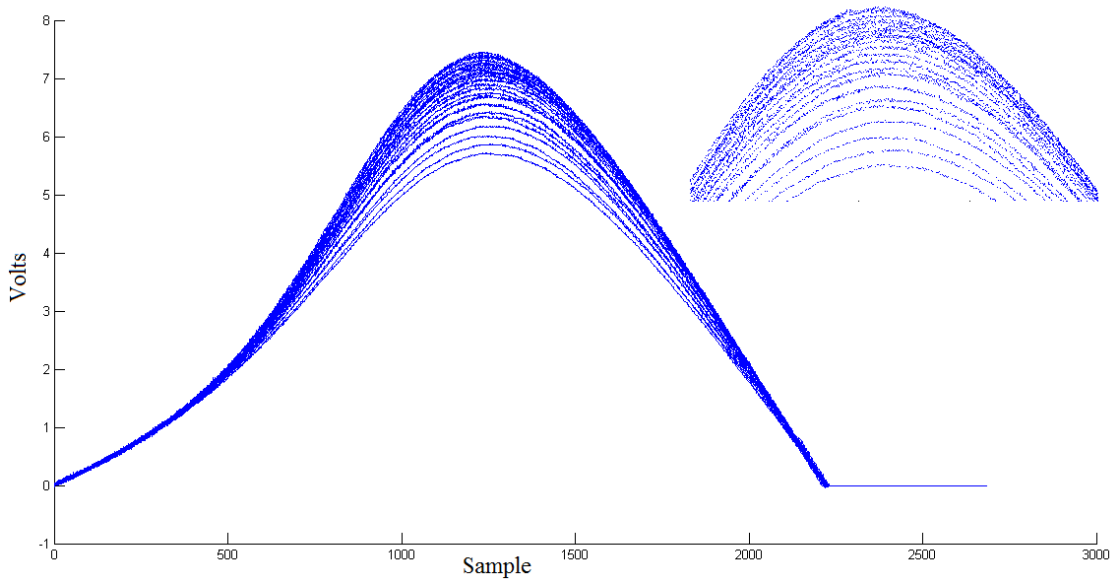

Figure 5.9 Detail of blade signals at different gaps

5.5 Conclusions

In the speed range tested so far, there was no signal change with the speed. Instead, what is important to consider is the change of the signal amplitude with different blades. Measurements of clearance are possible, but the peak to peak value of the signal depends on the blade and a normalization is needed. This limitation can be avoided introducing a new configuration of the sensor, as it will be described in chapter 7.

Accurate clearance measurement are possible with an uncertainty of ±22 μm within the range [1 ÷ 1.5] mm of gap variation. The accuracy is very similar of what is possible to obtain with capacitive probes. This point out very promising performance for the application in BTC systems.

6 Blade tip timing measurements

6.1 Introduction

This chapter focuses on the most relevant tip-timing test performed during this project. First, a simulation of synchronous and asynchronous vibration in the universal calibration bench is reported. Subsequently, two external collaboration with Fogale Nanotec (Nimes, France) and the ITWL (Warsaw, Poland) has given an important contribution in improving the instrumentation. Results of the external tests are illustrated. Finally, the optimized measurement system was installed in the VKI R2 compressor rig.

6.2 Simulations of synchronous and asynchronous vibrations

The components of the measurement system (sensors, electronics and software) were realized during the on-going collaboration between VKI and the Italian Universities of Perugia and Padova. A large part of the development process was performed in the innovative universal calibration bench (paragraph 4.7). The most significant test performed in this facility regards a simulation of an asynchronous and a synchronous resonance.

6.2.1 Test setup and methodology

Tip-Timing signals have been acquired along a speed transient from 2000 rpm up to 15000 rpm. The frequency of the imposed vibration to the sensor (by means of the shaker) was kept fixed at 100Hz, from the beginning to the end of the test. The amplitude was kept constant at 0.1 mm up to 13000 rpm, where it was decreased to about 0.05 mm. Moreover, two excitations were simulated increasing the amplitude of the excitation up to 0.2mm. The first simulated resonance was at 4000 rpm, the second at 6000 rpm. The Campbell diagram of the test is shown in Figure 6.1: the fixed excitation at 100Hz is represented by the red line. At 4000 rpm it does not cross any engine order lines (EO), the excitation is not an integer multiple of the revolution frequency and it represents an asynchronous vibration. At 6000 rpm, the red line crosses the 1EO line, in fact, the frequency of the imposed vibration is 1 time the revolution frequency and it correspond to a synchronous vibration.

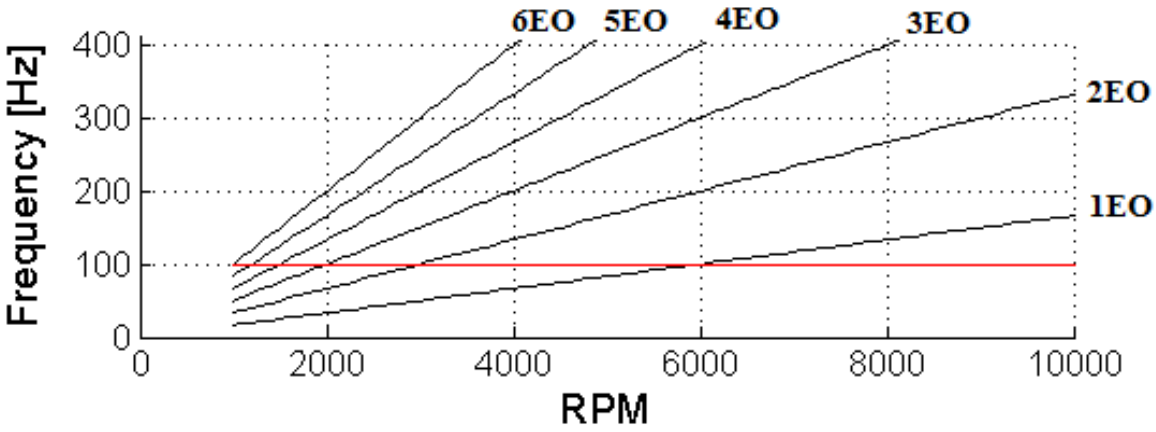

Figure 6.1 The Campbell diagram of the test

6.2.2 Results

Figure 6.2 shows the waterfall of the measured displacements for the first seven blades. The two resonances at 4000 rpm and 6000 rpm are clearly visible. At 6000 rpm the measured displacements show a change in the DC component of the signal, as typical for synchronous vibrations. The presence of the two simulated resonances is evident, even though the constant vibration level at 0.1mm is always present up to 13000 rpm.

From the waterfall, the Individual Measured Displacements (IMD) of blade 1 (Figure 6.3), were processed further. A window of 200 samples was defined and successive Fast Fourier Transforms (FFTs) were performed, with a step of 10 samples. The 3D individual blade spectrogram of Figure 6.4 was obtained. Having only one vibrating sensor, one blade displacement sample per revolution is measured. In this way, the sampling frequency (SF) of the IMD is the revolution frequency and it is changing with the speed during the transient. Therefore, the vibration at 100 Hz measured in the IMD is aliased up to 12000 rpm and it is folded at different frequencies, depending on the SF (to note that SF = speed). This results in a zig-zag patch in the spectrogram [72], up to 12000rpm. As expected, there are visible peaks around 4000rpm and 6000rpm. Finally, the spectrogram of Figure 6.4 shows the zig-zag patches of the harmonics of 100Hz and electric noise at 50Hz. These results are even clearer in Figure 6.5, which represents the 3D spectrogram seen from the top, with the amplitudes in color: the so-called Zplot.

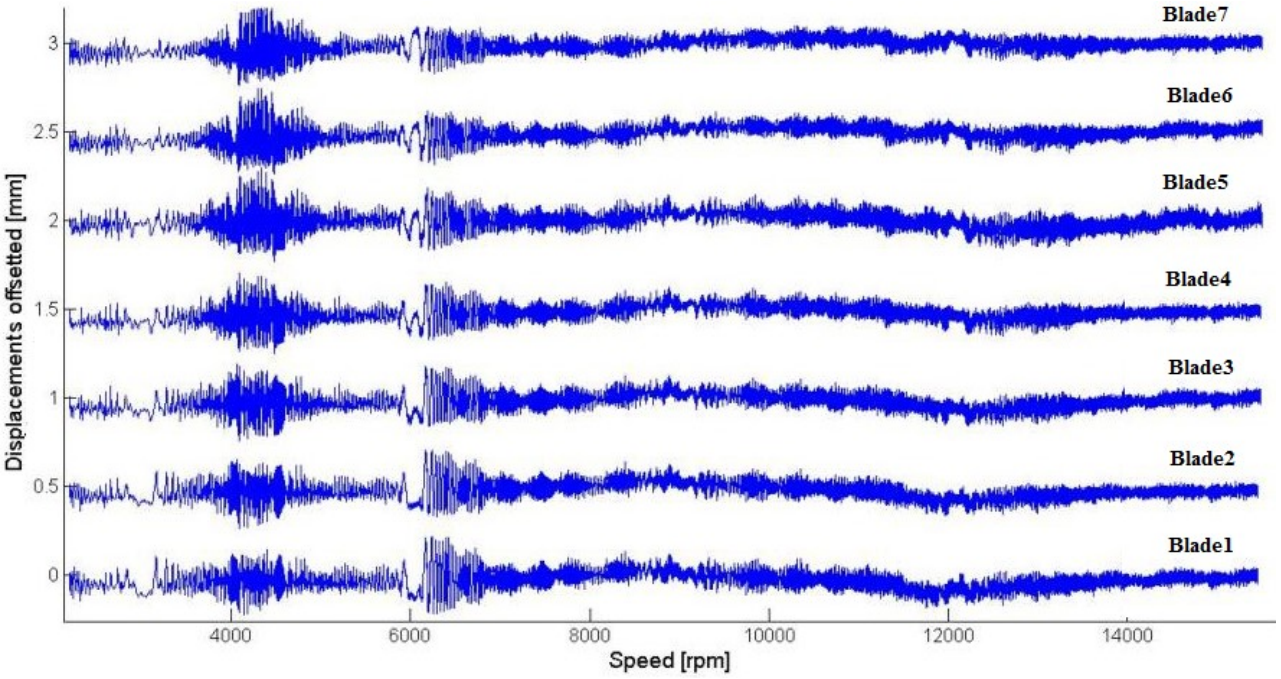

Figure 6.2 The waterfall of the measured displacements of the first seven blades

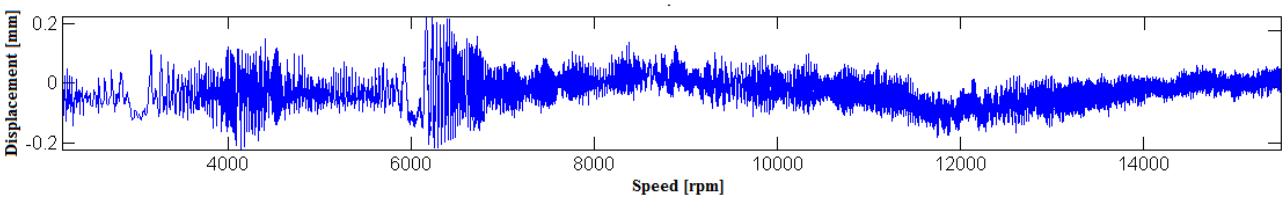

Figure 6.3 Individual measured displacements of blade1

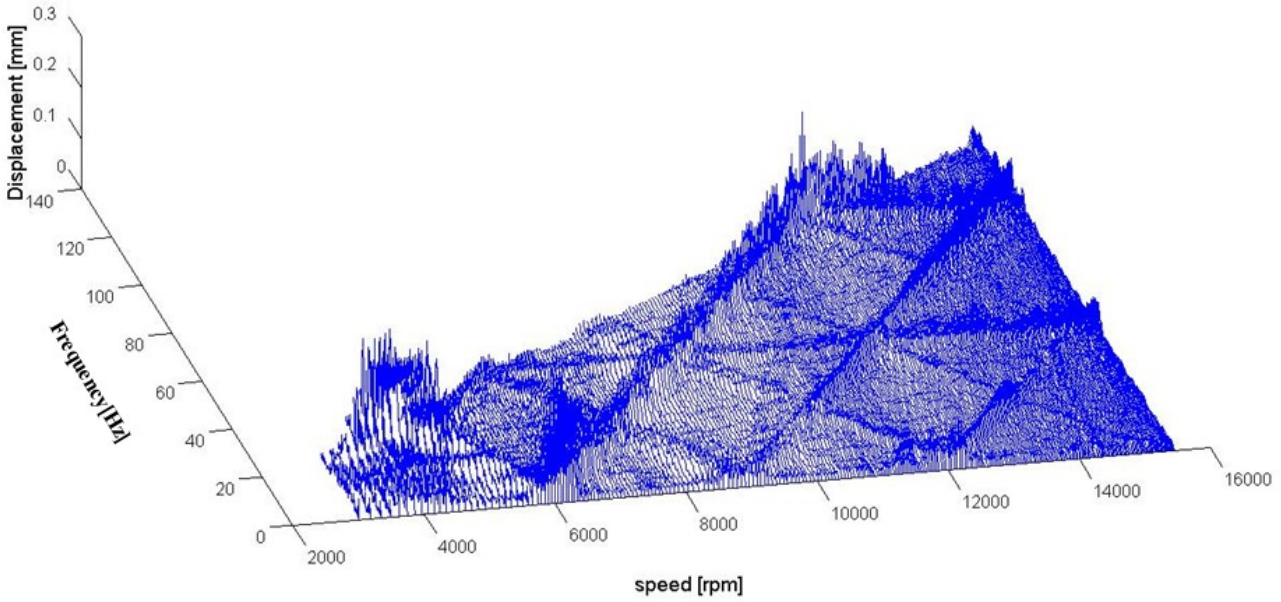

Figure 6.4 3D Spectrogram of the individual measured displacements of blade1

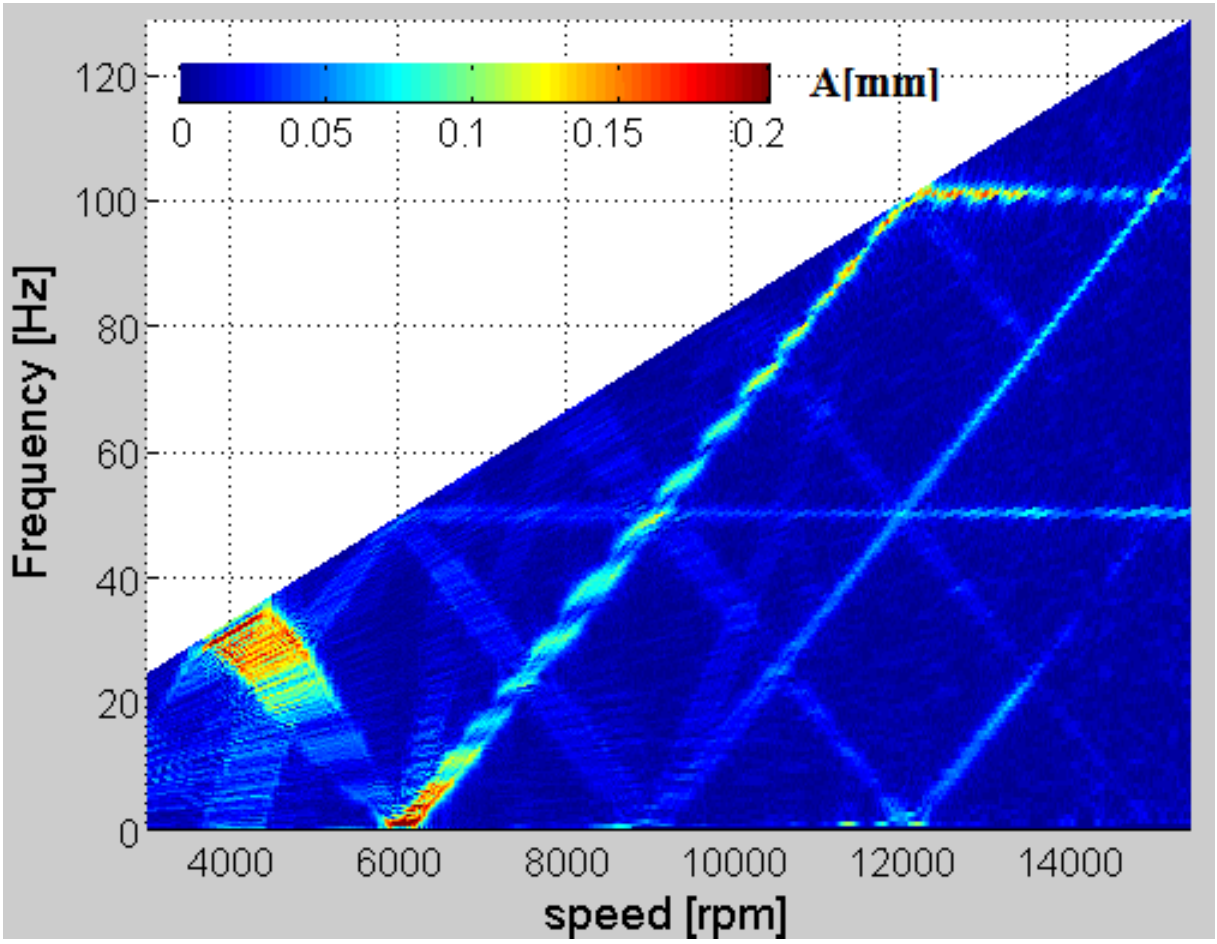

Figure 6.5 The Zplot of the measured displacements of blade 1

6.3 External validation test at Fogale Nanotech

Fogale nanotech is a manufacturer of BTC and BTT systems based on capacitive probes. It has 30 years of expertise in the field of capacitive metrology. During this research project an external test of the developed instrumentation was performed at Fogale aiming at validating and improving the system.

6.3.1 Test setup and methodology

Six Fogale capacitive probes and two magnetoresistive sensors were installed in the test bench of Fogale (figure 6.6). Simultaneous tip-timing measurements of the rotating wheel were acquired and processed with the Fogale software. The details of the test bench and the acquisition system are confidential.

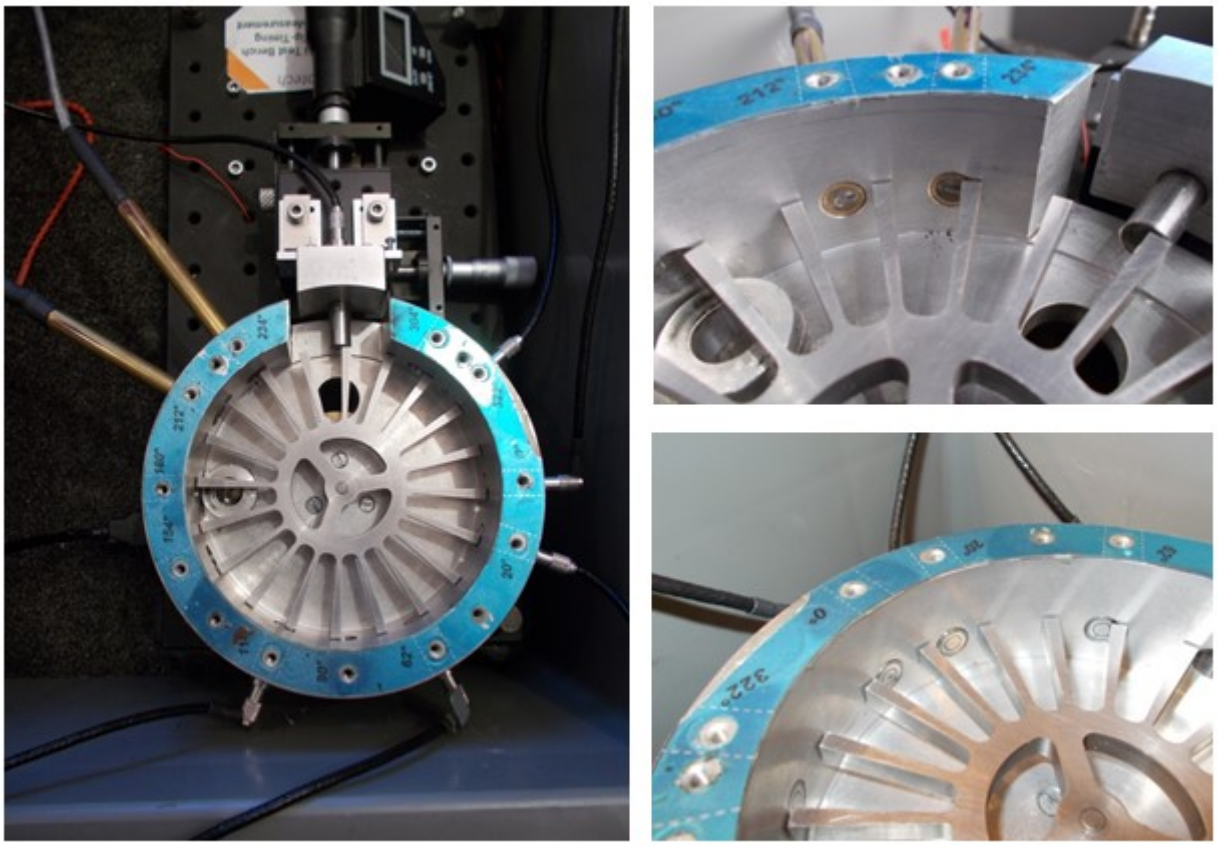

Figure 6.6 The Fogale test bench

6.3.2 Results

The results of the data processing with the two different type of sensors are in strong agreement and the resonances were correctly measured. No problems or missing blades were encountered. The magnetoresistive signal was compatible with the processing system and the whole instrumentation developed was successfully validated. The acquired signals with both the sensors were very useful as test case to improve the dedicated software developed so far. Below some real-time results were saved during the acquisition. Figure 6.7 and 6.8 shows the waterfall of the measured displacements. It can be seen, from the change in the DC component of the signals, that both the sensors were measuring a resonance around 8000rpm. Finally, figure 6.9 and 6.10 reports the Zplot obtained at the end of the test. At that time a FEM analysis of the rotating wheel was not available. Hence, the folded frequencies in the spectrum are unknown, but it can be seen that the zig-zag patches strongly agree meaning the measurement of the same phenomena. Quantitative comparison were not possible, but the signals acquired helped in fixing software bugs.

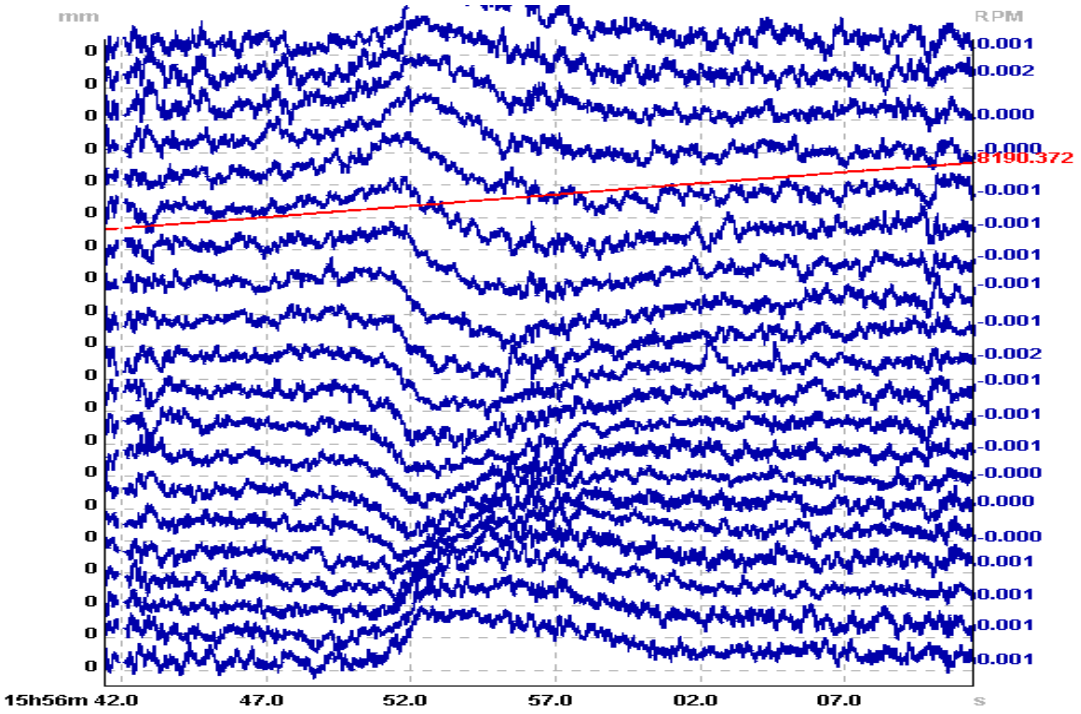

Figure 6.7 A detail of the waterfall of the measured displacements with the capacitive sensors at Fogale

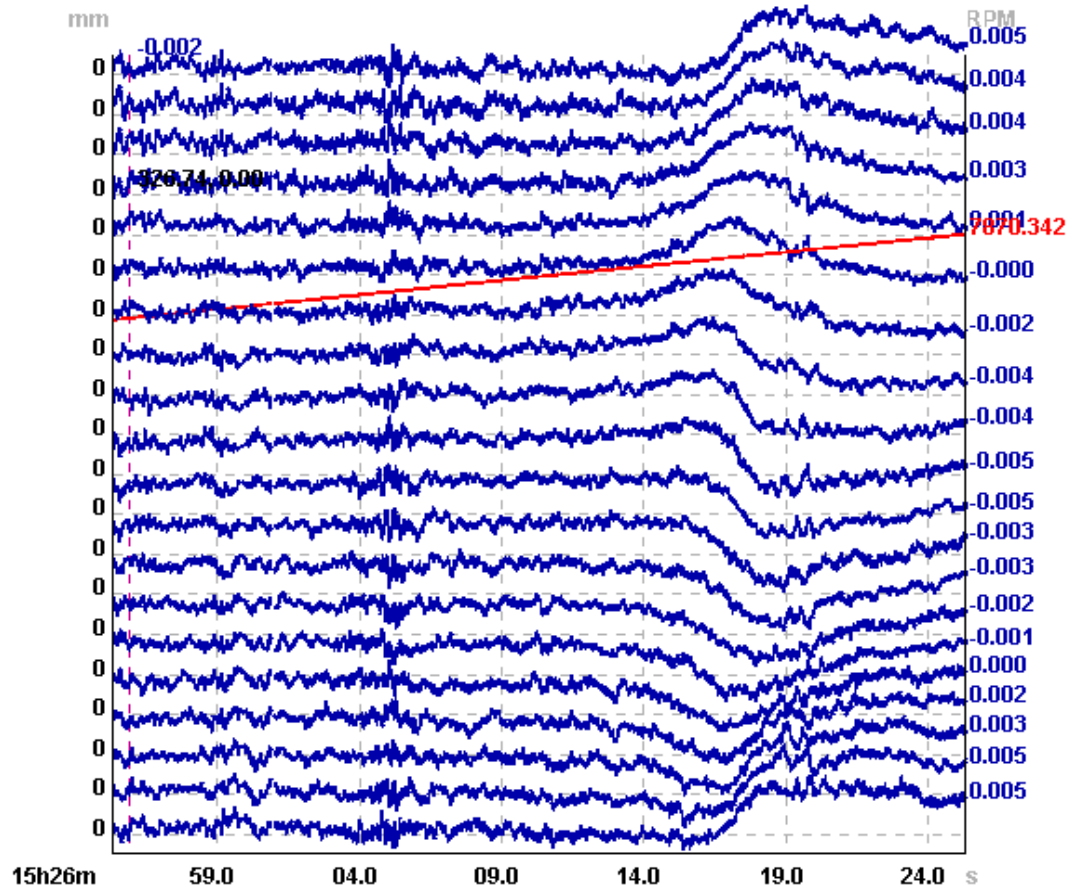

Figure 6.8 A detail of the waterfall of the measured displacements with the magnetoresistive sensors at Fogale

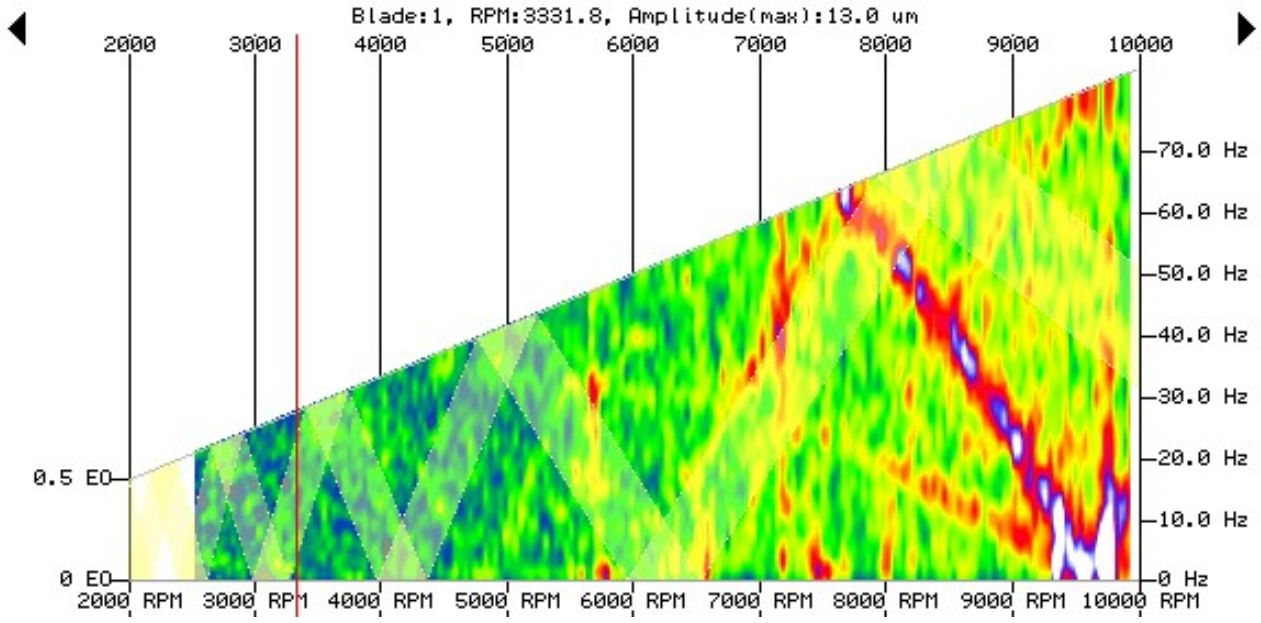

Figure 6.9 The Zplot from the measured displacements with the capacitive sensors at Fogale

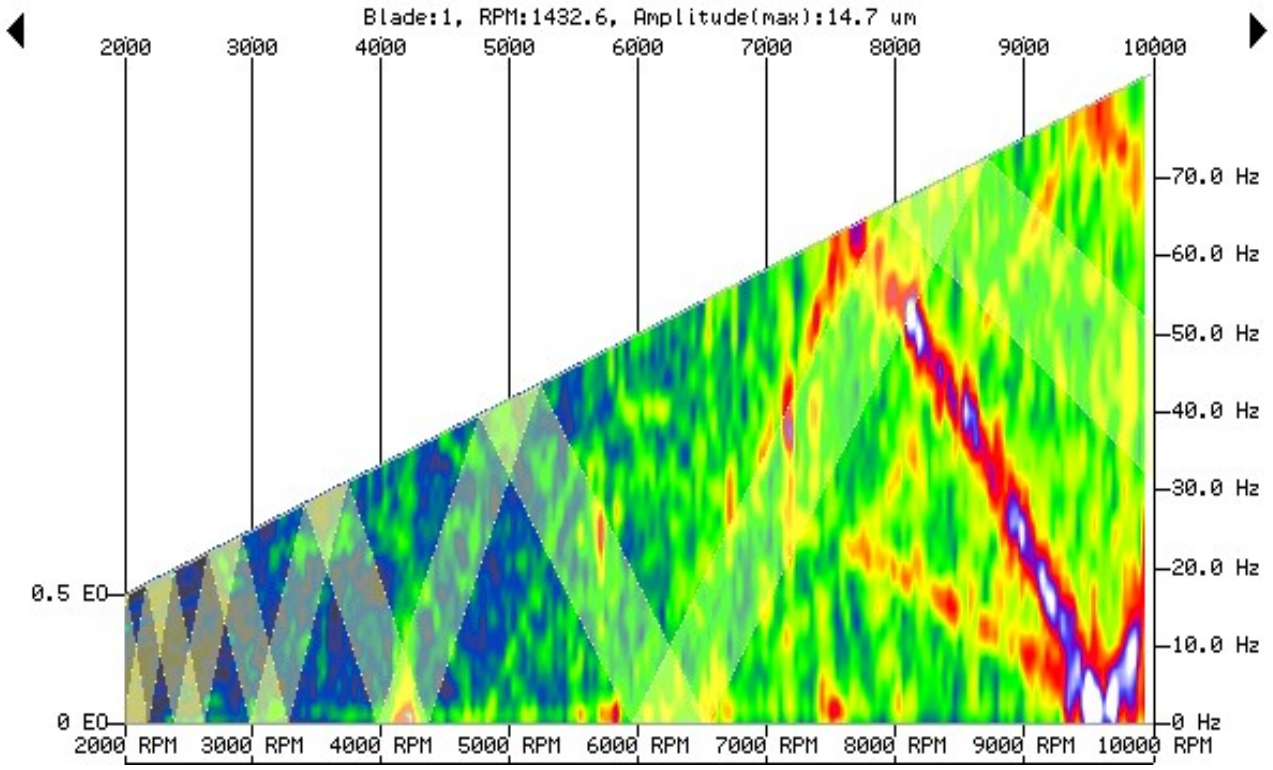

Figure 6.10 The Zplot from the measured displacements with the magnetoresistive sensors at Fogale

6.4 External validation test at ITWL

The ITWL in Warsaw, Poland, is a military research institute of technology working with real aeroengines and developing its own instrumentation. This second external test was performed to try the magnetoresistive sensors on a real aeroengine, in order to have a real test case as reference and to compare the results with a different measurement system.

6.4.1 Test setup and methodology

The magnetoresistive sensors were mounted in the military SO-3 turbojet engine of Figure 6.11. Four sensors were installed in slots prepared in the upper compressor casing in the plane of the second rotor stage of the compressor (Figure 6.11c). The rotor has 41 blades and a tip radius of 207 mm. Tip-timing data were acquired during a speed transient up to 16000 rpm. A piece of felt was attached to the Inlet Guided Vanes (IGVs) to excite the resonances. Previous tests performed at ITWL showed two blade resonances around 8000 rpm and 12000 rpm. The objective of the test was to repeat the experiment to validate the diagnostic system based on magnetoresistive elements and collect reference data.

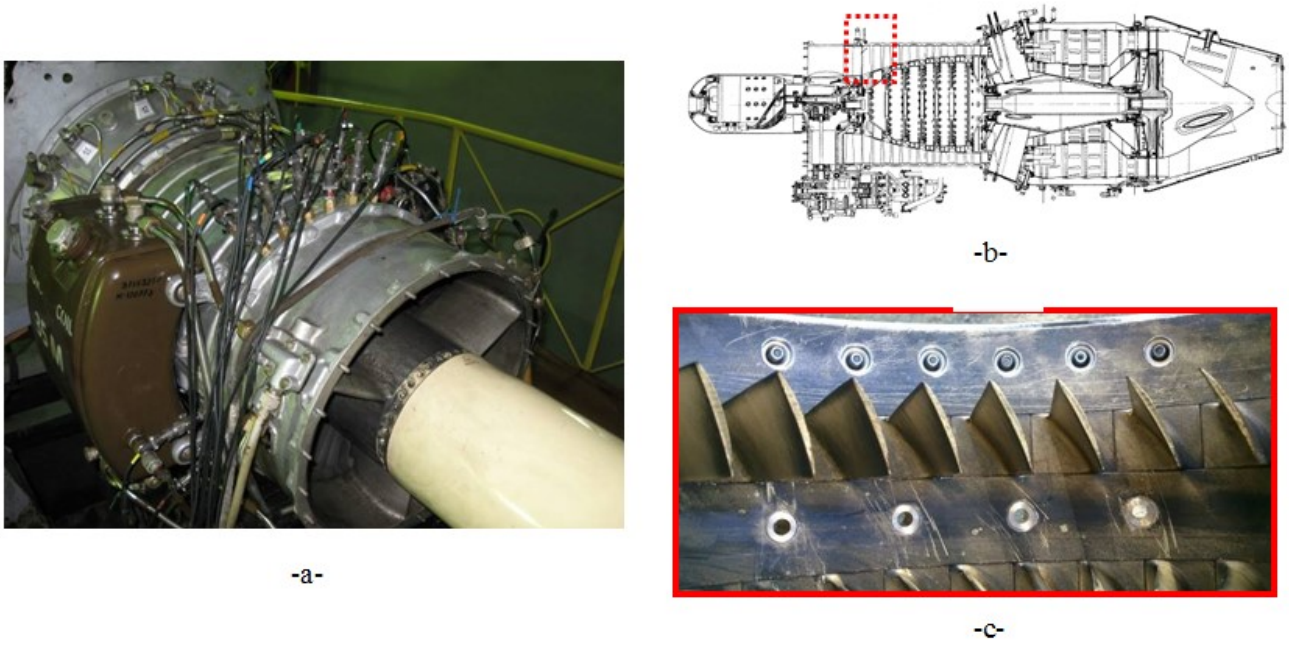

Figure 6.11 (a-b) The SO-3 turbojet engine – ITWL, (c) The 4 slots in the casing to install the sensors

6.4.2 Results

The magnetoresistive signals were recorded and processed by the ITWL Tip-Timing software. The waterfall of the measured displacements for the first 15 blades are shown in figure 6.12 for the ITWL eddy current sensors and in figure 6.13 for the magnetoresistive sensors. Both the waterfalls show the two expected resonances around 8000 rpm and 12000 rpm. Some blades were exited at slightly different rpm, which can be due to mistuning. From the FEM analysis on the blade geometry performed at ITWL, two blade resonances were expected around 8000 rpm and 12000

rpm. In particular, the first mode is excited by the EO3 at 12000 rpm and by the EO4 around 8000 rpm. The data could not be processed further to have an estimate of the measured vibration frequencies. Anyway, it is possible to compare the results at the stage of the measured displacements. Figure 6.14 focuses on the measured displacements around 12000 rpm. Figure 6.15 and 6.17 are obtained by overlapping the measured displacements with the different sensors around the second resonance, for blade 1 and blade 6. The peaks of the measured resonances in the two tests are in strong agreement, both in amplitude and with respect to the speed. The expected resonances were measured correctly and this confirm the possibility of performing tip-timing measurements with the novel magnetoresistive probes. To notice that the measurements performed with the magnetoresistive sensors show a drift. There might be several reasons. Further investigations on the single components of the measurement chain will improve the system, anyway the drift did not compromise the results. Finally, the whole instrumentation chain was successfully working in a real engine for the first time. The magnetoresistive sensors were compatible with the ITWL acquisition system and processing software. No damage was reported. The dedicated electronic boards developed at VKI were successfully working up to 11 kHz blade passing frequency and no particular noise problems were observed.

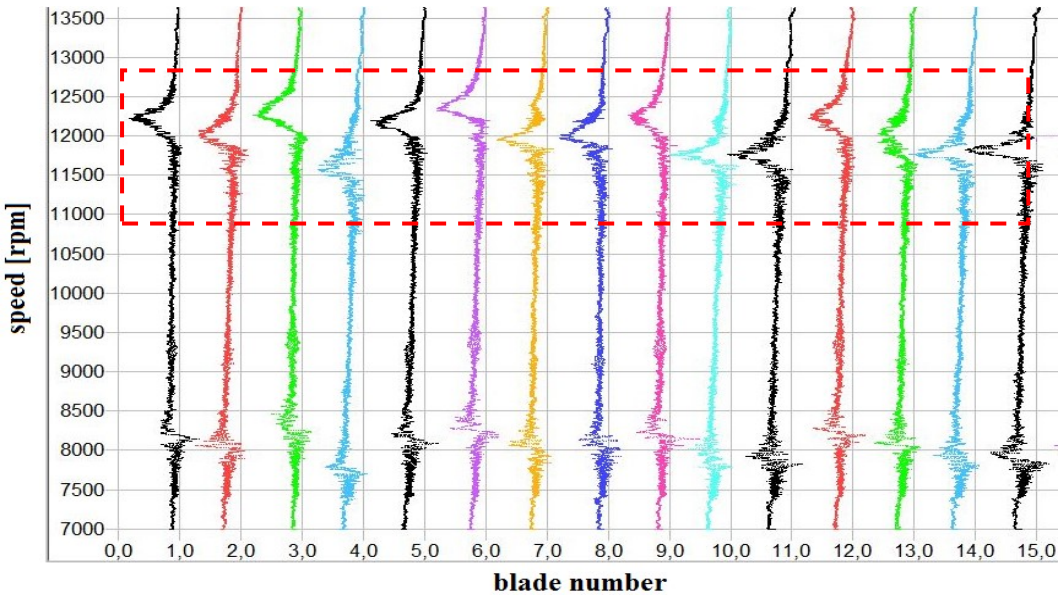

Figure 6.12 The waterfall of the measured displacements of the first 15 blades, ITWL sensors

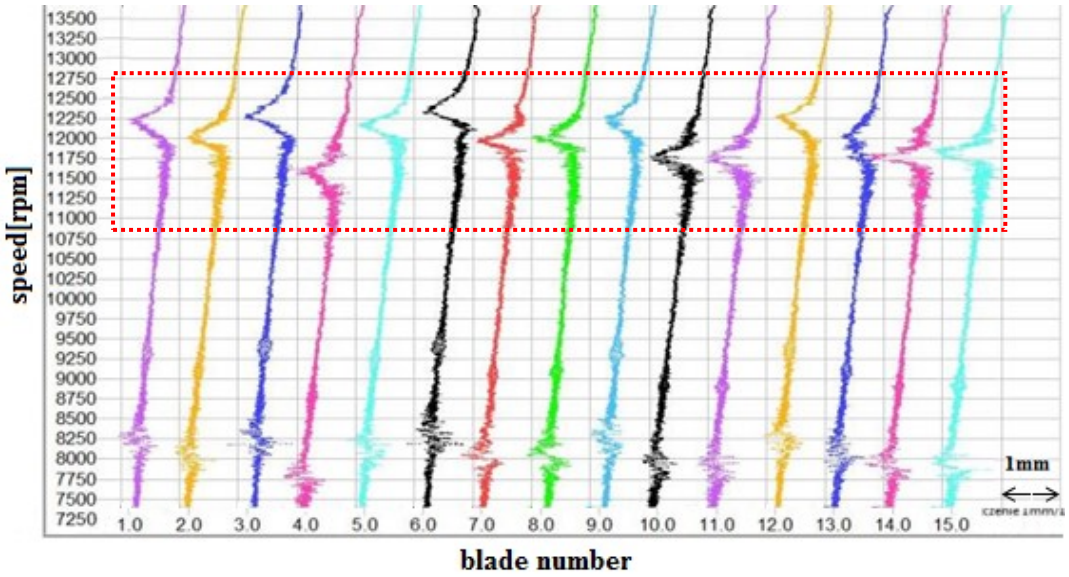

Figure 6.13 The waterfall of the measured displacements of the first 15 blades, magnetoresistive sensors

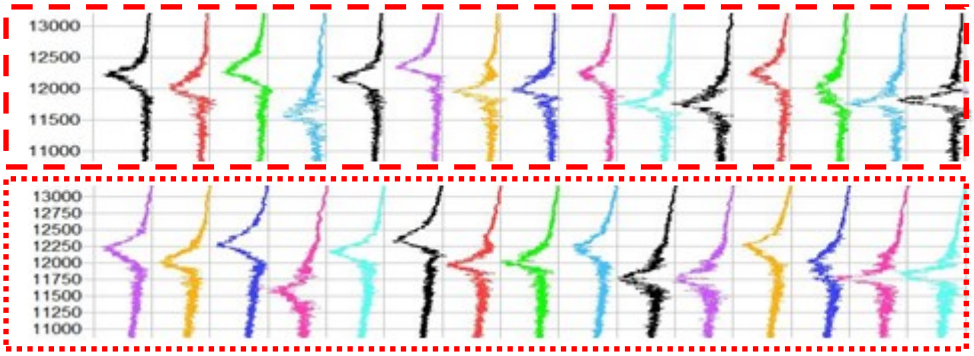

Figure 6.14 Comparison of the measured displacements around 12000 rpm

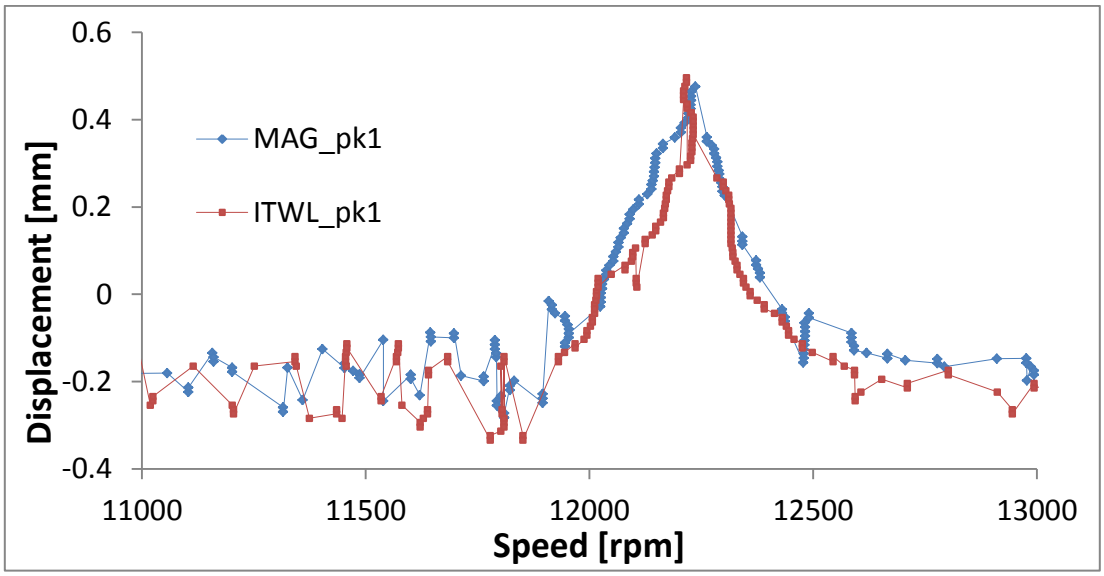

Figure 6.15 Comparison of the measured displacements around 12000 rpm, blade 1

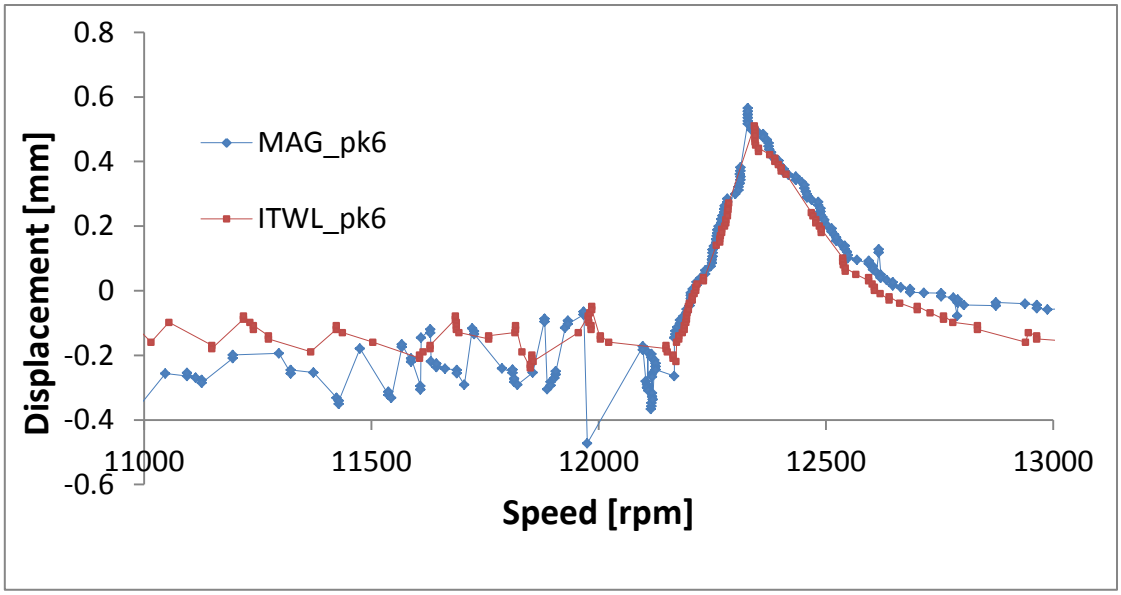

Figure 6.16 Comparison of the measured displacements around 12000 rpm, blade 6

6.5 The VKI R2 compressor

The validated and improved instrumentation was installed in the VKI R2 compressor (see paragraph 5.4.1) to acquire tip-timing signals during an acceleration transient. There are no FEM models or references on the modal analysis of the rotor. Therefore, the characterization of the blades was performed experimentally.

6.5.1 Test setup and methodology

Three sensors were mounted in the casing at [0 90 180]°. Tip-timing signals were acquired along a speed transient from 2000 rpm up to 5500 rpm, with a sampling frequency of 1 MHz per channel. No information was available regarding the expected blade vibration modes and frequencies. For this reason, the hammer test with an accelerometer was performed on the blades to have an estimate of the first bending frequency. It was assessed to be around 480Hz. Considering this and the speed range of the test, it is possible to get the Campbell diagram of figure 6.17. The red line represents the first bending frequency of the blades. It should account for the contribution of the centrifugal force at different rpm, which increases the blade resonance frequency with the speed, but it could not be estimated at this stage. The Engine Order lines (EO) indicate the multiple integers of the rotor rotational frequency. For instance, the 2EO is the line fitting all the points equal to 2 times the rotational frequency. When a line representing a blade vibration mode crosses an EO line, a synchronous resonance can be excited at the crossing speed. Therefore, during this test, synchronous blade resonances may appear around 2800, 3200, 3600, 4200, 4800 rpm. To let the

compressor works in off-design condition, a distortion grid was mounted at the rotor inlet (Figure 6.17 right). Moreover, an air injection system at the blade tip was installed to excite asynchronous resonances. Four bent pipes were installed in the casing, two at 0° and two at 180° (figure 6.17 right). Compressed air at 5 bar was blown against the blade tips at about 3500 and 5400 rpm.

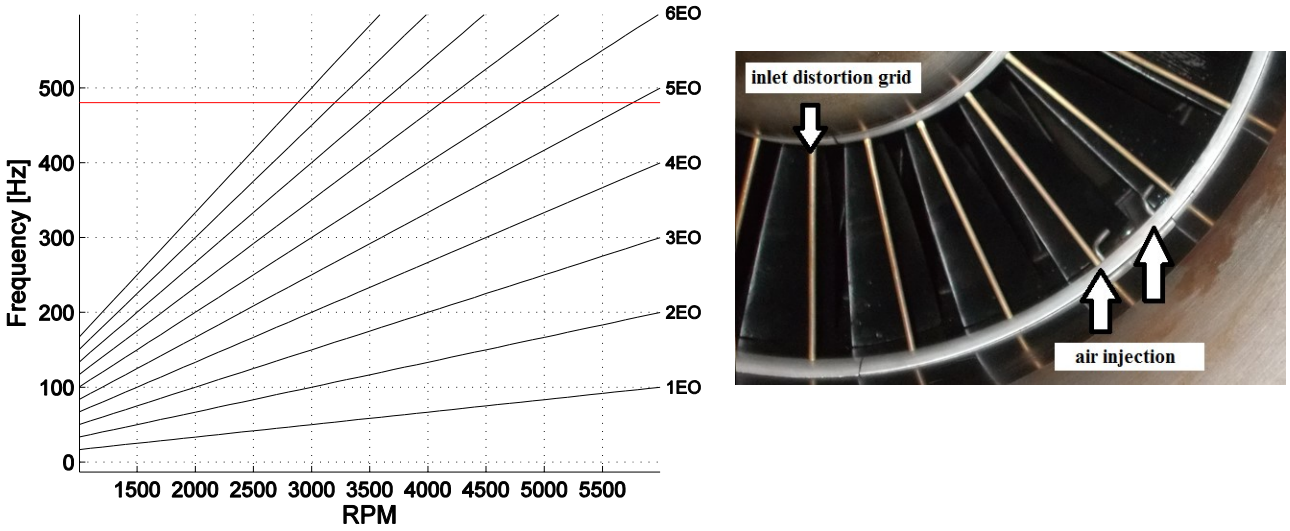

Figure 6.17 Left: the VKI R2 Campbell diagram. Right: the compressor inlet

6.5.2 Results

The clearance variation during the test was negligible; nevertheless the magnetic distortion induced by the blades of the R2 compressor was significant, resulting in high signal to noise ratio. Concerning the measurement of the vibrations, figure 6.18 and 6.19 show the waterfall of the measured displacements of the first 4 blades. The measured displacements of blade 2, 3 and 4 were shifted (by adding a DC constant value) to have an ensemble graph. The synchronous blade resonances appear in the waterfall as a change in the DC component and the maximum peak value of this change is taken as representative of the vibration amplitude. The asynchronous blade resonances appear as a change of frequency with respect to the base frequency of the noise of the system and the maximum peak value of this change is taken as representative of the vibration amplitude. As shown in Figure 6.18, a synchronous resonance was measured around 3650 rpm and an asynchronous resonance around 3450 rpm, as expected. Nevertheless, the measured amplitudes are moderate. More evident is the synchronous resonance measured around 4900 rpm (Figure 6.19). The latter was expected to be around 4800 rpm, but the effect of the centrifugal force was not considered. Finally, the asynchronous resonance around 5400 rpm is also present.

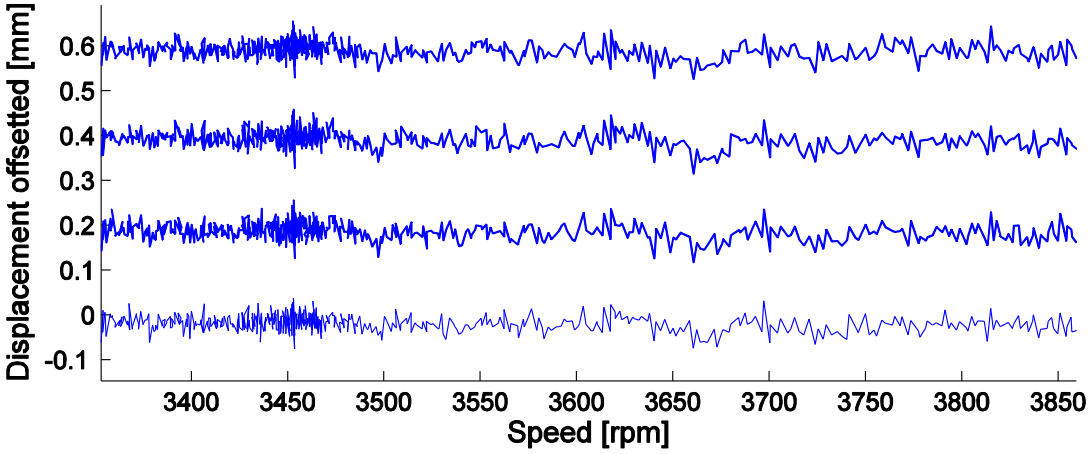

Figure 6.18 The measured displacements in the R2 compressor, part 1

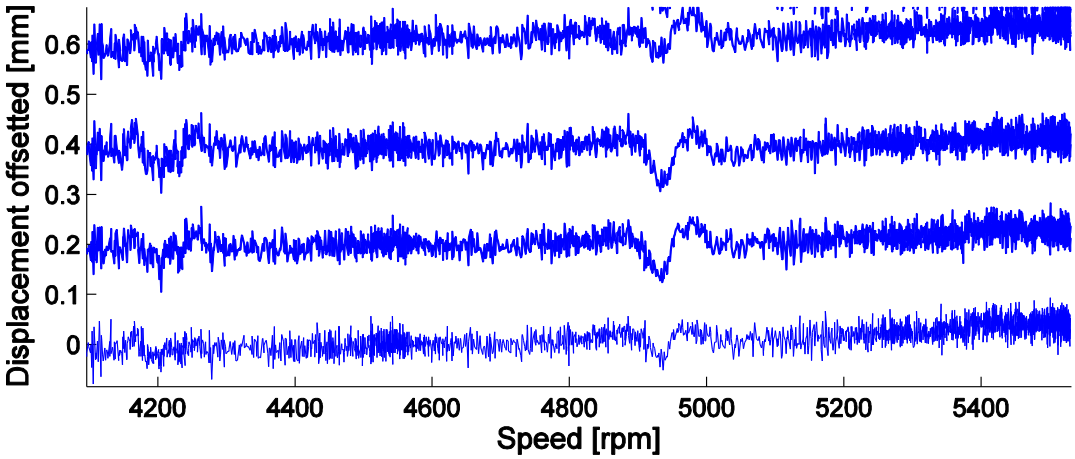

Figure 6.19 The measured displacements in the R2 compressor, part 2

6.6 Conclusions

Measurements of blade vibrations were carried out on test benches and real turbomachines with very satisfactory results.The universal calibration bench realized was very important for the development of the whole instrumentation. There are still margin of improvement, but comparisons with different sensors and simulations of vibration resonances can be easily handled. Performance of the magnetoresistive BTT and BTC systems were improved step by step in different test cases. The developed instrumentation always resulted successful and very promising. No missing resonances were observed and the dedicated components always worked well.

One aspect to further investigate regards the drift on the sensor signal appeared on the measurements in the real jet-engine. It is not compromising the results, but further studies can avoid this disturb.

7 Developments

7.1 Introduction

During this research project the whole instrumentation developed had several improvements. Bugs and errors were corrected in the software, bandwidth limitation avoided in the electronics and different sensor configurations were tested. This chapter reports the main developments achieved so far. First, a real time software based on the post-processing routines described in paragraph 4.8, was realized. Then, a differential sensor which avoid the calibration process, is illustrated. Finally, preliminary test were performed in realizing an anti-aliasing software for tip timing data.

7.2 The real-time software

The algorithm described in paragraph 4.8 was developed and improved during the 3 years of this research project. From the first configurations, several bugs and errors were corrected and it becomes a robust software. Nevertheless, it is a post-processing algorithm which means that the signals are processed after the acquisition and the results came after the processing procedures. Hence, it was re-designed in GCode in Labview to implement the same logic but in a real-time processing environment. Parts of the calculation routines developed in Matlab were re-used and the measured displacements are always the same. This paragraph illustrates the acquisition system used and some details of the GCode in Labview.

7.2.1 Tip-Timing and Tip Clearance data acquisition in streaming

The realization of a real-time software for BTC and BTT data analysing requires very powerful acquisition systems, with high sampling frequency and several channels. In other words: performing and expensive components.

In this project, only one channel was used in all the acquisitions. The routines developed are not at multichannel level, therefore the real – time algorithm could be implemented with a USB Picoscope 5444B. It is a USB acquisition board with:

- 4 channels;
- Resolution 8/16 bit;
- Bandwidth up to 200 Mhz;

- 512 MS of buffer;
- PC interface USB 2.0 high-speed;
- Internal signal generator.

In real-time processing, the acquisition hardware can work in **streaming** or in **block mode**. The first one allow the continuous acquisition of the signals from the channels and the communication with the software of processing. The block mode is a faster communication, but it has a time dedicated to the acquisition and a time dedicated to the transfer of data to the pc in which the system is blind for the signal.

In this case, it is not acceptable to interrupt the signal acquisition and to lose data, therefore the Picoscope was configured for streaming mode. The maximum sampling rate achievable in this mode is 200 KS/s, with 8 bit of resolution. The hardware needs special setting to configure prior of the acquisition. The manufacturer, on the website, provides the library at this scope:

- **ps5000Open** to open the communication between the software and the Pico;
- **ps5000Settings** to setup the channels and other parameters;
- **ps5000stream** to setup the streaming of data;
- **ps5000getStream** to get a packet of data;
- **ps5000close** to close the communication.

In figure 7.1 the block diagram realized to setup the communication with the libraries. The processing program is composed of the sub-routines described in chapter 4. Figure 7.2 shows the block diagram of the core of the software with the call to the sub-routines. Finally, figure 7.3 is the front panel of the program. In other words it is the graphical interface for the user, where it is possible to setup all the parameters and the results (like the waterfall of the displacements) appear in real-time.

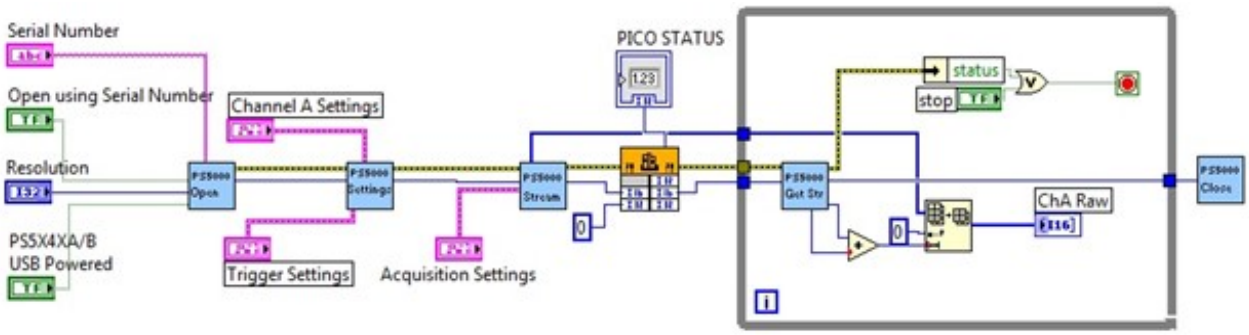

Figure 7.1 The block diagram for the configuration of the streaming of data

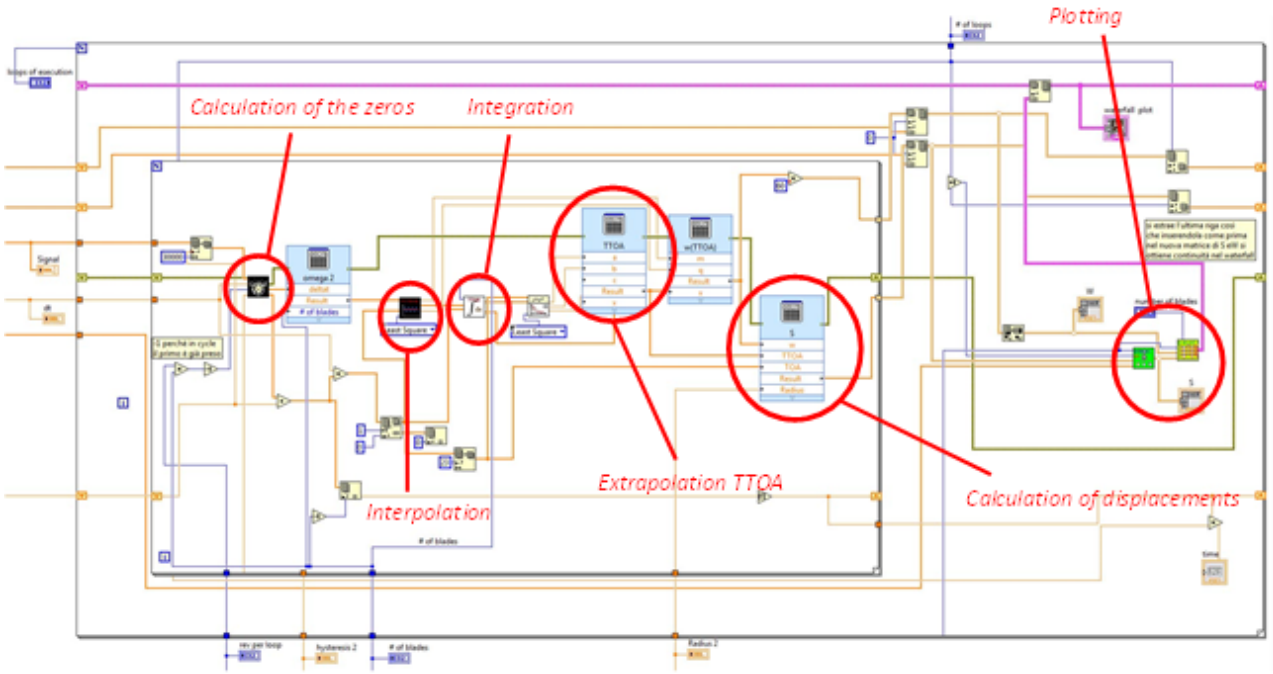

Figure 7.2 The main block diagram

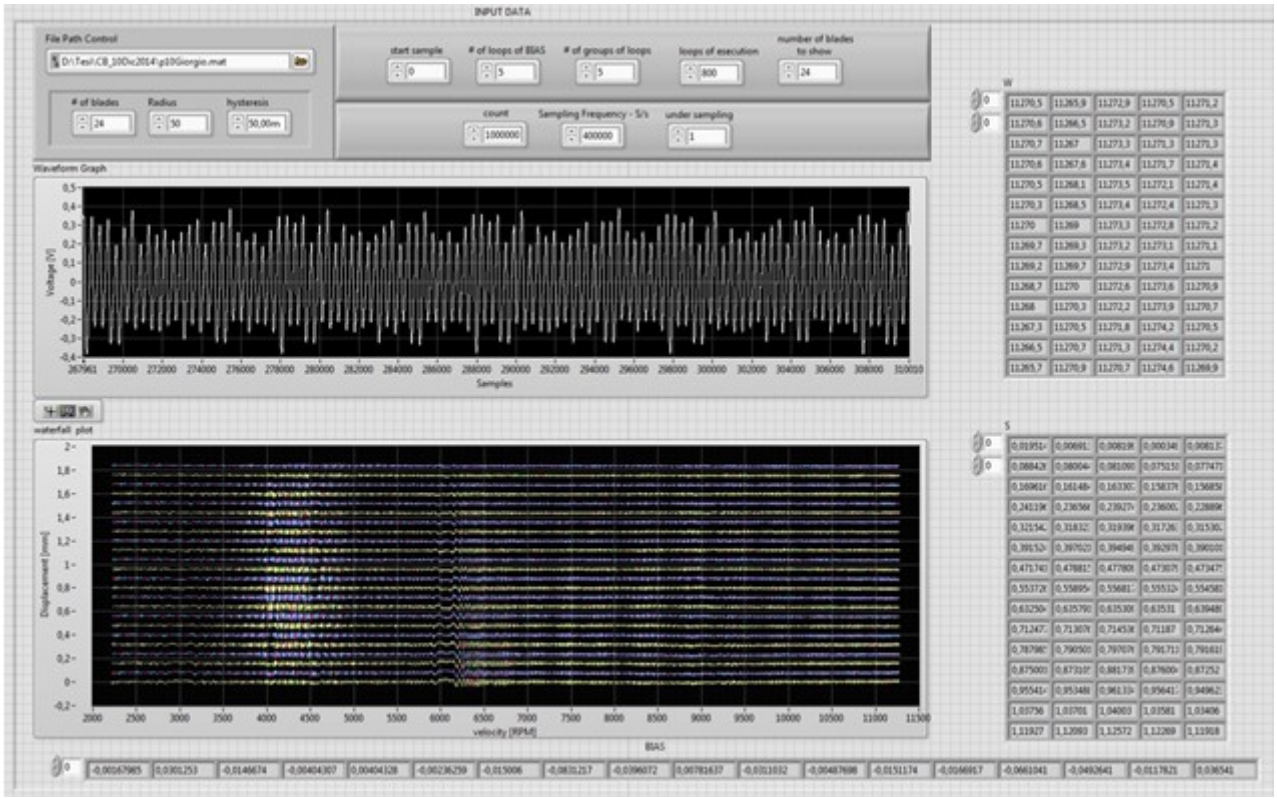

Figure 7.3 The front panel of the software

7.3 The differential sensor

Concerning the developments on the sensor components layout and design improvements, an experimental campaign was focused on two main aspects. On one hand, it were studied the different possibilities to detect and to measure the position and the displacement of an object (like a blade), through different shielding materials (like Aluminium), without making holes on them. This is possible thanks to the different magnetic permeabilities of the materials. For instance, the magnetoresistive probes can detect the blade passage through an Aluminium layer, up to 10 mm thickness with a SNR reduction of about 50%, but still good for the measurements. The advantage is not only on avoiding to make holes in the casing to mount the sensors, but also on the possibilities to use shielding material at the sensor's top for applications in hot environments.

On the other hand, developments were focused on improving the repeatability when using different materials. Passages of blades of different ferromagnetic materials at the same distance sensor-blade tip, often results in different maximum voltage levels because of different polarization. This aspect needs a normalization, then the calibration curve can be calculated. To avoid this, it was realized a new configuration: the differential sensor of figure 7.4. Basically, two sensing elements are mounted inside the sensor casing, shifted of a known quantity (i.e. 1 mm). In this way, at every blade passage the probe generates two output signals, as reported in figure 7.5. The blue signal is negated respect to the typical output because the sensor is mounted upsidedown. It is possible to take the two absolute maximum peak values (the dots in blue and green) then report in a graph respect to the distance. At this point, there is only one linear curve passing through the two points and this will be the calibration curve of the differential sensor (figure 7.6 left). Respect to the normal sensor, the differential probe avoids the calibration procedure, at the cost of a less accurate calibration curve because it is fitted on two points. Figure 7.6 right reports a comparison of the calibration curves between a normal sensor calibrated in the range of [0.5 – 2.5] mm of blade tip gap and the differential sensor mounted at 1 mm from the blade tip and its immediate calibration curve extended to this range. The choice depends on several parameters, but where the accuracy do not need to be very high, the differential sensor facilitates the classical procedures.

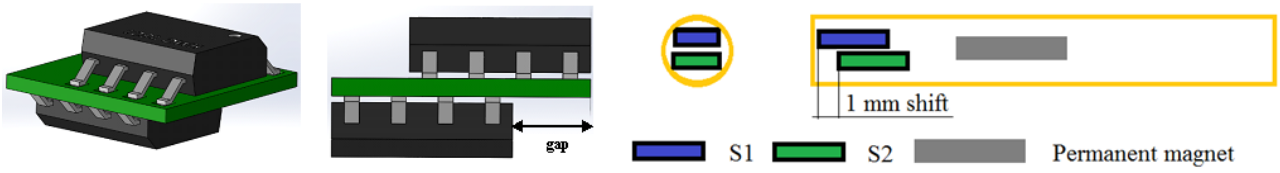

Figure 7.4 The differential magnetoresistive sensor

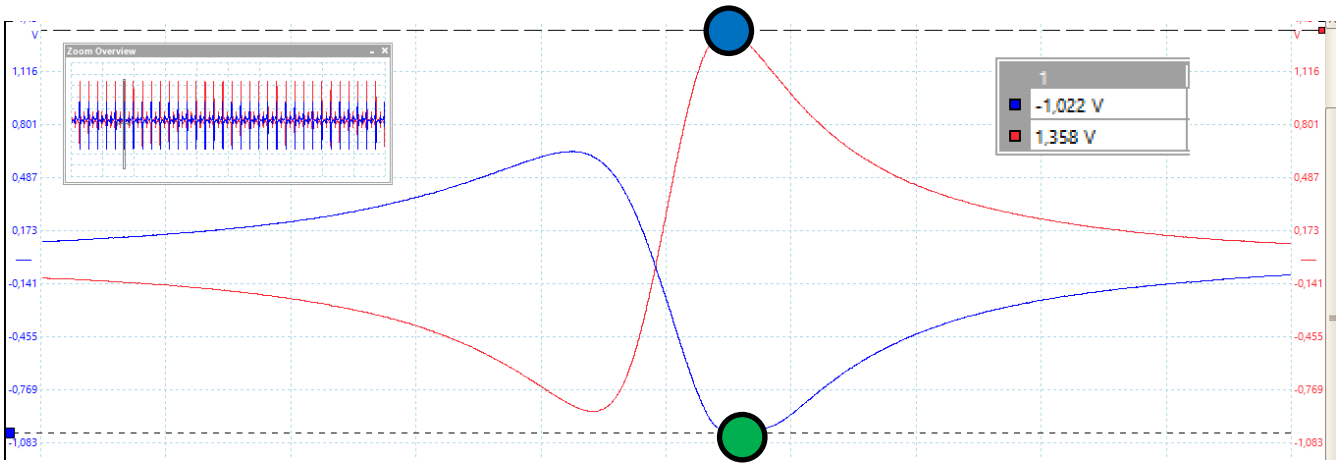

Figure 7.5 The two signals from the differential sensor

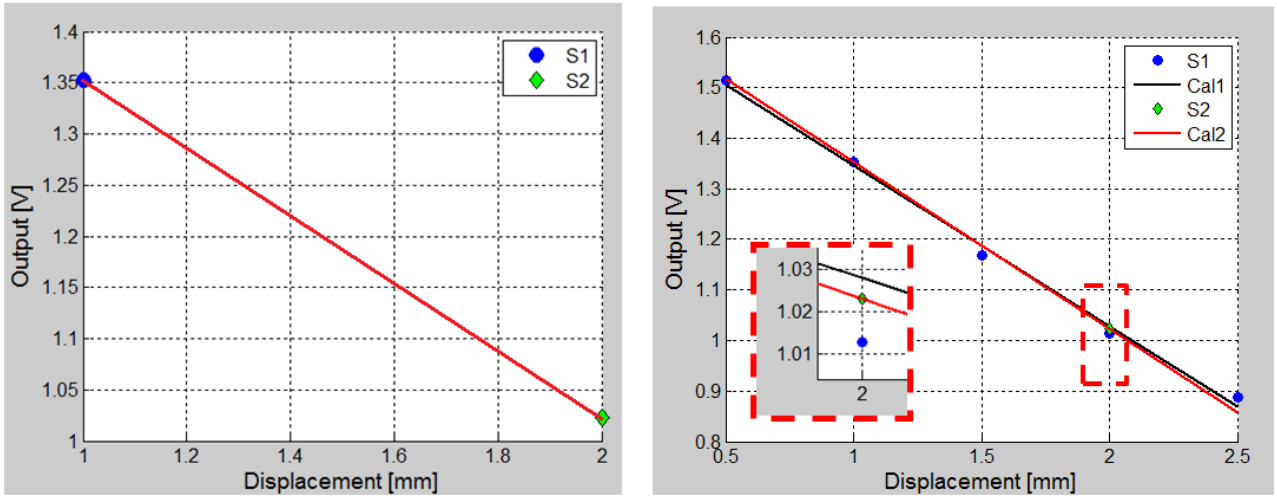

Figure 7.6 Comparison of the calibration curves

7.4 The Anti-Aliasing algorithm for tip-timing data

Finally, a new processing methodology to better analyze folded frequencies from BTT data was studied. Figure 7.7 shows the measured displacements of the blade 1 of the SO-3 jet-engine calculated with the algorithm developed in the frame of this project. By computing successive FFTs with a window of 200 samples, it is possible to have the so-called Z-Plot of Figure 7.8. The blade resonance around 9000 rpm appears in red. Moreover, there is a zig-zag patch that represents a blade vibration mode presents up to about 12000 rpm. Its frequency is unknown because BTT data is usually aliased due to the fact that it is possible to record only few blade vibration samples per revolution and the Nyquist theorem is not satisfied. This results in a zig-zag patch. One way to avoid the aliasing is to use several BTT sensors, which make the measurement chain expensive and

complex. A better way can be implemented from the software side, by considering the multiples of the folded frequencies. An algorithm calculates the first N multiples of the measured folded frequency (Figure 7.9) and selects among them the most probable true real frequency of vibration. The selection procedure is a combination of methods, still under development. A preliminary result on the data from the SO-3 Jet-Engine is shown in Figure 7.10. The "cleaned" Zplot has only the calculated real frequency of the vibration around 550 Hz, which is in good agreement with the FEM Analysis of the Polish Institute.

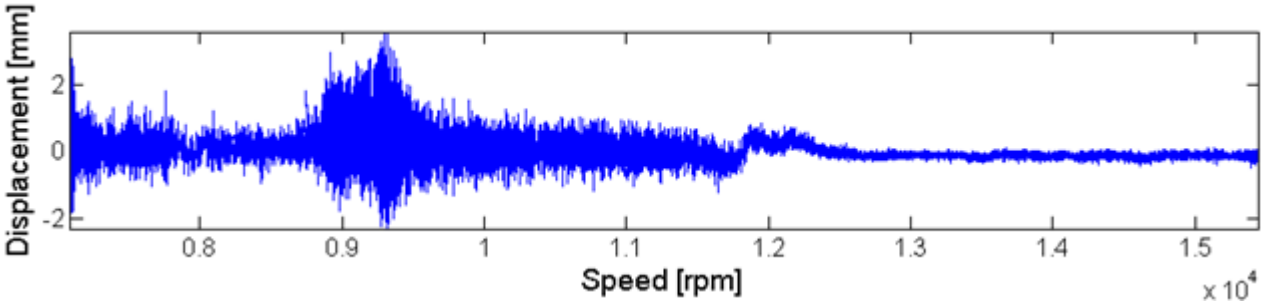

Figure 7.7 Raw measured displacements calculated with the matlab software

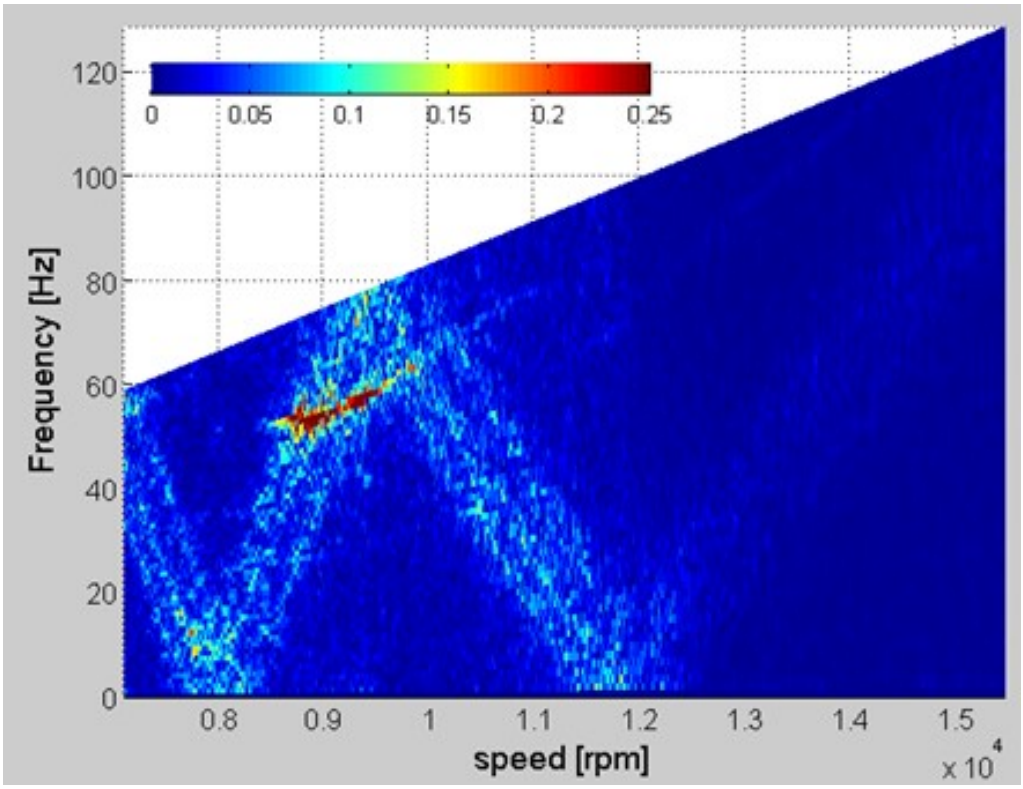

Figure 7.8 The Zplot of an aliased frequency

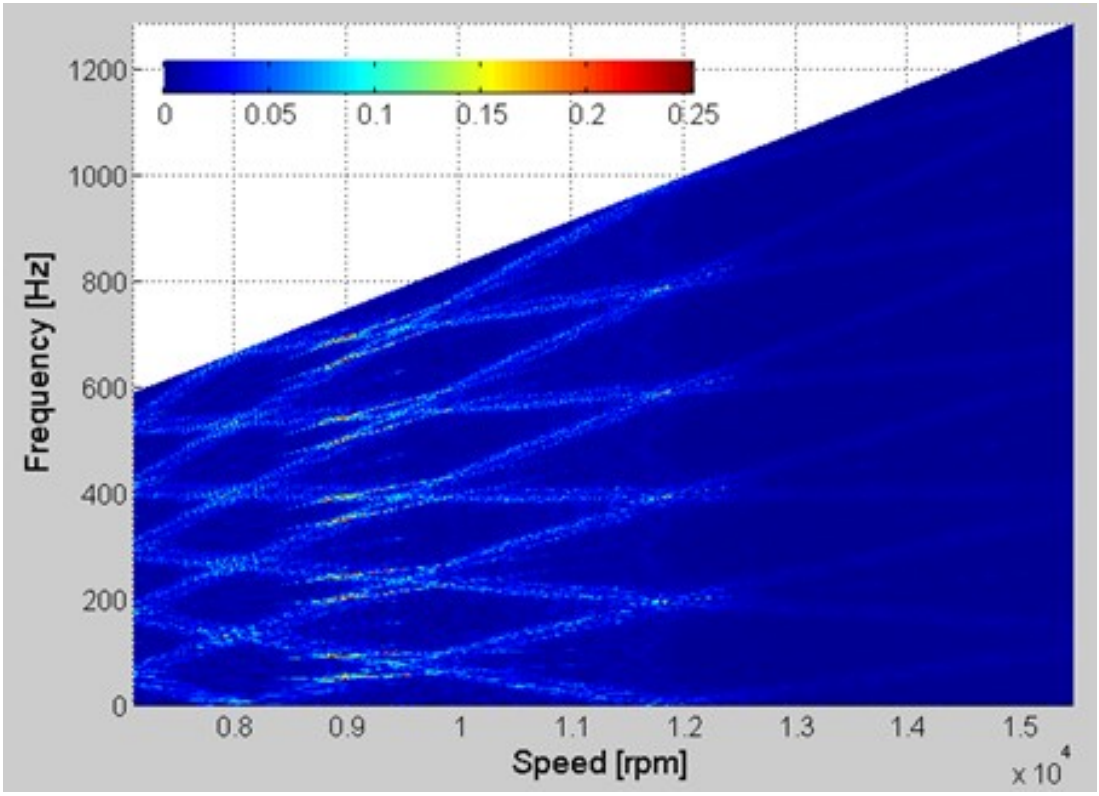

Figure 7.9 The Zplot of the multiples of the aliased frequency

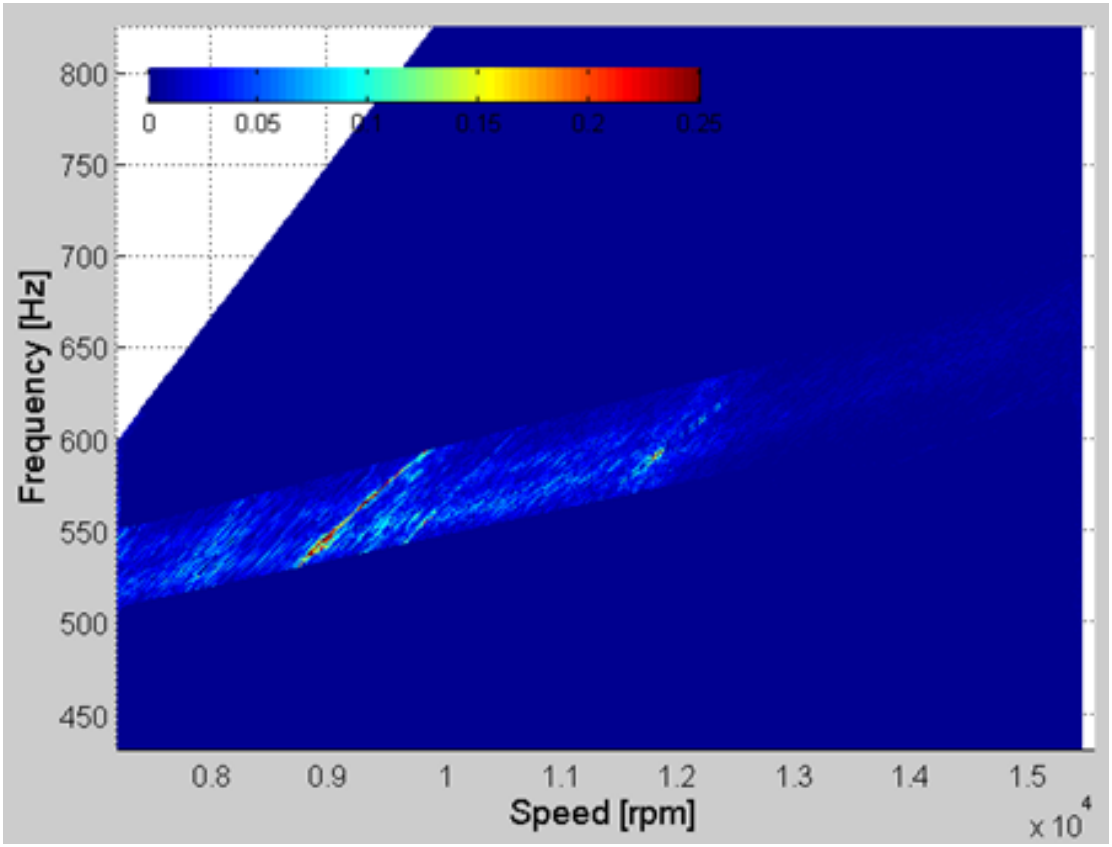

Figure 7.10 The Zplot after the anti-aliasing procedure

7.5 Conclusions

The realization of the differential sensor facilitates the calibration process and avoids the normalization of the data explained in chapter 5.

A basic real-time measurement system was illustrated. More powerful hardware and more sophisticated routines are needed to achieve the level of a professional multichannel BTT and BTC system. Nevertheless, the one sensor real time system presented here, has given satisfactory results in the calibration bench and it is an handy development platform for new applications.

8 Conclusions and Recommendations for Future Work

8.1 Conclusions

Various types of sensors have been proposed for Blade Tip Clearance and Blade Tip Timing systems including electromagnetic, magnetic, inductive, optical, capacitance, eddy currents and microwave. In this research project, a new sensor based on a magnetoresistive sensing elements has been designed, realized and tested.

Clearance tests were carried out showing the possibility to perform very accurate measurements with an uncertainty of $U = \pm 0{,}022$ mm (20:1) within the range [1 ÷ 1.5] mm of gap variation, in line with the current performance of commercial sensors. Tip-timing test cases were performed in test benches and in real turbomachines with very satisfactory results. Two external collaborations with Fogale Nanotech (France) and the ITWL (Poland) validated the system against different sensor technology and has given the possibilities to improve further its performance.

Significant improvements were introduced during this project respect the first system configuration. A differential magnetoresistive sensor was realized to avoid the calibration procedure and data normalization. A real-time software and an innovative universal calibration bench for any BTT and BTC sensor were developed. The principle of the blade motion decomposition can be now used for simulation of different working conditions and development of new methods.

A database of technical information and a significant know-how on the use of magnetoresistive sensors in turbomachinery testing is now available. The simultaneous BTC and BTT system developed was successful in all test cases. It is still at the level of prototype, but it shows all the requirements to be engineered at the level of a professional instrumentation.

8.2 Future Work

The future work should start from two main aspects:

- First of all, the application of the magnetoresistive sensors should be studied for hot environments. A new sensor configuration must be designed using a thermal shield or innovative solutions. The first limitation in this kind of application will be the maximum working temperature of the sensing element, which is currently limited at 125°C. Hence, a thermal isolation system must be developed. From the side of the magnet, the limit is the

Curie temperature, which is much higher than 125°C. The application of an electromagnet to substitute the permanent magnet should be considered. It also offers the possibility to tune the magnetic field depending on the application.

- Further developments are needed in terms of data processing methods. The anti-aliasing software reported in chapter 7 should be improved and validated with strain gauge measurements or similar. Innovative algorithms can decrease the amount of hardware components needed for BTT and BTC measurements.

9 References

[1] T. C. Booth, *Importance of tip clearance flows in turbine design.* Tip Clearance Effects in Axial Turbo-machines. Lecture Series, Von Karman Institute for Fluid Dynamics, 1985.

[2] D. Lombaert, *Blade vibrations in turbomachinery -a literature study.* Von Karman Institute for Fluid Dynamics, U-VKI2008-10, 2007.

[3] K. Chana, *Fundamentals of tip timing and tip clearance sensors.* Tip timing and tip clearance problems in turbomachinery. Lecture Series, Von Karman Institute for Fluid Dynamics, 2007.

[4] J. P. Roberts, *The potentials of tip timing and tip clearance measurements for aero propultion gas turbines,* in Tip timing and tip clearance problems in turbomachinery, Lecture Series, Von Karman Institute for Fluid Dynamics, 2007.

[5] A. von Flotow, M. Mercadal, and P. Tappert, *Health monitoring and prognostics of blades and disks with blade tip sensors*, in Aerospace Conference Proceedings, 2000 IEEE, vol. 6, pp. 433^40, IEEE, 2000.

[6] J. F. Brouckaert, *Tip timing and tip clearance problems in turbomachinery.* Lecture Series, Von Karman Institute for Fluid Dynamics, 2007.

[7] D. Cardwell, K. Chana, and P. Russhard, *The use of eddy current sensors for the measurement of rotor blade tip timing-sensor development and engine testing*, ASME GT2008-50792, 2008.

[8] J. Gallego-Garrido, G. Dimitriadis, and J. R. Wright, *A class of methods for the analysis of blade tip timing data from bladed assemblies undergoing simultaneous resonances part ii: Experimental validation*, International Journal of Rotating Machinery, vol. 2007, 2007.

[9] S. Heath and M. Imregun, *An improved single-parameter tip-timing method for turbomachinery blade vibration measurements using optical laser probes*, International journal of mechanical sciences, vol. 38, no. 10, pp. 1047-1058, 1996.

[10] H. S. Dhadwal and A. P. Kurkov, *Dual-laser probe measurement of blade-tip clearance*, Journal of turbomachinery, vol. 121, Issue 3, pag. 481-485, 1999.

[11] T. Pfister, L. Buttner, J. Czarske, H. Krain, and R. Schodl, *Turbomachine tip clearance and vibration measurements using a fibre optic laser doppler position sensor*, Measurement Science and Technology, vol. 17, no. 7, p. 1693, 2006.

[12] M. Zielinski and G. Ziller, *Noncontact blade vibration measurement system for aero engine application*, in 17th International Symposium onAirbreath-ing Engines, Paper No. ISABE-2005-1220, 2005.

[13] S. Lavagnoli, G. Paniagua, M. Tulkens, and A. Steiner, *High-fidelity rotor gap measurements in a short-duration turbine rig*, Mechanical Systems and Signal Processing, vol. 27, pp. 590-603, 2011.

[14] G. W. Terpay, *Shielded Eddy Current Sensor For Enhanced Sensitivity,* United states patent 5,942,893, 1999.

[15] R. Grzybowski, G. Foyt, W. Atkinson, W. Knoell, J. Wenger, and D. Benz, *Microwave blade tip clearance measurement system.* ASME96-GT-2, 1996.

[16] A. Maslovskiy, *Microwave Turbine Tip Clearance Measuring System for Gas Turbine Engines.* ASME-GT2008-50354, 2008.

[17] M. Wagner, A. Schulze, M. Vossick, C. Stephelbauer, R. Weigel, N. Vortmeyer, and P. Heide, *Novel microwave vibration monitoring system for industrial power generating turbines*, in Microwave Symposium Digest, 1998 IEEE MTT-S International, vol. 3, pp. 1211-1214, IEEE, 1998.

[18] C. Belsterling, *Sensing with air,* Instrumentation Science and Technology*,* vol. 18, no. 3, pp. 37—41, 1971.

[19] J. Rickman Jr, *Eddy current turbocharger blade speed detection*, IEEE Transactions on Magnetics, vol. 18, no. 5, pp. 1014-1021, 1982.

[20] C. Roeseler, A. von Flotow, and P. Tappert, *Monitoring blade passage in turbomachinery through the engine case (no holes)*, in Aerospace Conference Proceedings, 2002. IEEE, vol. 6, pp. 6-3125, IEEE, 2002.

[21] J. Gallego-Garrido, G. Dimitriadis, and J. Cooper, *Further Developments of Blade Tip-timing Data Analysis Techniques.* PhD thesis, 2005.

[22] I. B. Carrington, *Development of blade tip timing data analysis techniques*. PhD thesis, University of Manchester, 2002.

[23] G. Rossi, *Progettazione, realizzazione e caratterizzazione di un sistema di misura di vibrazioni di organi rotanti di turbomacchine con sensori stazionari.* PhD thesis, Facolta di ingegneria Universita di Ancona, 1993.

[24] I. Y. Zablotskiy and Y. A. Korostelev, *Measurement of resonance vibrations of turbine blades with the elura device*, Energomashinostroneniye,(USSR), no. 2, pp. 36-39, 1970.

[25] S. Heath, T. Slater, L. Mansfield, and P. Lof-tus, *Turbomachinery blade tip-timing measurement techniques*, Proceedings of Advisory Group for Aerospace Research and Development Conference, 90th Symposium on Advanced Non Intrusive Instrumentation for Propulsion Engines, pp. 32-1 32-9, Brussels, Belgium, 1997.

[26] S. Heath and M. Imregun, *A survey of blade tip-timing measurement techniques for turbomachinery vibration*, Journal of engineering for gas turbines and power, vol. 120, no. 4, pp. 784-791, 1998.

[27] M. Zielinski and G. Ziller, *Noncontact vibration measurements on compressor rotor blades*, Measurement Science and Technology, vol. 11, no. 7, p. 847, 2000.

[28] G. Dimitriadis, I. B. Carrington, J. R. Wright, and J. E. Cooper, *Blade-tip timing measurement of synchronous vibrations of rotating bladed assemblies*, Mechanical Systems and Signal Processing, vol. 16, n. 4, pp. 599-622, 2002.

[29] I. B. Carrington, J. R. Wright, J. E. Cooper, and G. Dimitriadis, *A comparison of blade tip timing data analysis methods*, Proceedings of the Institution of Mechanical Engineers, Part G: Journal of Aerospace Engineering, vol. 215, no. 5, pp. 301-312, 2001.

[30] J. Gallego Garrido, G. Dimitriadis, and J. R. Wright, *Development of a multiple modes simulator of rotating bladed assemblies for blade tip timing data analysis,* in Proceedings of the 27th International Conference on Noise and Vibration Engineering ISMA02, pp. 1437-1446, 2002.

[31] J. Gallego Garrido and G. Dimitriadis, *Validating synchronous blade vibration amplitudes from blade tip-timing data analysis*, Institution of Mechanical Engineers, vol. 623, no. 23, pp. 205-213, 2004.

[32] E. Armstrong and R. Stevenson, *Some practical aspects of compressor blade vibration*, The Journal of the Royal Aeronautical Society, vol. 64, no. 591, pp. 117-130, 1960.

[33] W. Robinson, *Overview of pratt and whitney nsms*, in 45th International Instrumentation Symposium, Albuquerque, New Mexico, 1999.

[34] W. Robinson and R. Washburn, *A real time noninterference stress measurement system (nsms) for determining aero engine blade stresses*, in Proceedings of the 37th Symposium of the Instrumentation Society of America, San Diego, California, pp. 91-103, 1991.

[35] H. T. Jones, *Development of advanced non-intrusive stress measurement processing techniques*, in Proceedings of the 6th National Turbine Engine High Cycle Fatigue Conference, Jacksonville, Fla, USA, 2001.

[36] B. W. Hayes, S. Arnold, C. Vining, and R. Howard, *Application of generation 4 non-contact stress measurement system on hcf demonstrator engines*, in Technical Papers of ISA, vol. 451, pp. 147-163, 2004.

[37] J. Gallego-Garrido, G. Dimitriadis, and J. R. Wright, *A class of methods for the analysis of blade tip timing data from bladed assemblies undergoing simultaneous resonances part i: Theoretical development*, International Journal of Rotating Machinery, vol. 2007, 2007.

[38] Ewins, D. (1992b). *Structural dynamic characteristics of individual blades*, in Vibration and rotor dynamic, Lecture Series 1992-06. VKI.

[39] Rao, J. (1991). *Turbomachine blade vibration*. New York: Wiley.

[40] Haupt, U. (1987a). *Blade vibration problems in centrifugal compressors*, in Flow in centrifugal compressors, Lecture Series 1987-01 (Vol. A). VKI.

[41] Hasemann, H., Weser, G., Hagelstein, D., & Rautenberg, M. (1997). *Investigation of the solidity and the blade vibration behaviour of unshrouded centrifugal compressor impellers with different aerodynamic design*, ASME, Vol. 97GT233.

[42] Rao, S. S. (2007). *Vibration of continuous systems*, Hoboken: Wiley.

[43] Imregun, M. (1999). *Aeroelasticity in axial Turbomachine*, in , Lecture Series 1999-05. VKI.

[44] Ewins, D. (1992a). *Structural dynamic characteristics of bladed disks*, in Vibration and rotor dynamic, Lecture Series 1992-06. VKI.

[45] Singh, M. P., Vargo, J. J., Schiffer, D. M., & Dello, J. D.(2000). SAFE Diagram, *A design and reliability tool for turbine blading*, Wellsville, New York: Dresser-Rand.

[46] Mehdigholi, H. (1991). *Forced Vibration of Rotating Disc and Interaction with Non-rotaring structures*. Ph.D. Thesis, College of Science, Technology andMedicine, London.

[47] JAY, R., MACBAIN, J., & BURNS, D. (1984). *Structural response due to blade vane interaction*. Journal of Engineering for Gas Turbines and Power, Vol.106, No 1, 50-56.

[48] Kushner, F. (2000). *Compressor blade and impeller rotating disk vibration avoidance parameters*. The American Society of Mechanical Engineers.

[49] Judge, J., Pierre, C., & Mehmed, O.(2001). *Experimental investigation of mode localization and forced response amplitude magnification for a mistuned bladed disk*. Journal of Engineering for Gas Turbines and Power, Vol.123, No 4, 940-950.

[50] Seinturier, E. (2005b). *Forced response computation for bladed disks industrial practices and advanced methods*, in Effects of aerodynamic unsteadiness in axial turbomachines, Lecture Series 2005-03. VKI.

[51] Singh, M., & Vargo, J.(1989). *Reliability evaluation of shrouded blading using the SAFE interference diagram*. Journal of Engineering for Gas Turbines and Power, Vol.111, No 4, 601-609.

[52] J. D. Denton. *Loss Mechanisms in Turbomachines*. Journal of Turbo-machinery, 115(4), pp 621-656, 1993.

[53] B. Glezer. *Transient Tip Clearance Analysis and Measurement Techniques*. Number 02 in Turbine Blade Tip Design and Tip Clearance Treatment. Von Karman Institute for Fluid Dynamics, Rhode Saint Genese, Belgium, January 2004.

[54] P.E.McCarty, W.Thompson Jr., *Development of non interference technique for measurement of turbine engine compressor blade stress*, Arnold Eng. Development Center Technical Report, 79-78, USAir Force, Tennessee, USA

[55] L.J.Kiraly, *Digital system for dynamic turbine engine blade displacement measurements*, NASA TM - 81382.

[56] H.Roth, *Vibration and clearance measurements on rotating blades using stationary probes*, Von Karman Institute [Lecture Series 81-7], (1981), Rhode Saint Genese, Belgium.

[57] Rossi G., Brouckaert J.-F., *Design of a blade tip timing measurement system based on uncertainty analysis*, 58th ISA International Instrumentation Symposium, San Diego (CA), June 4-7, 2012.

[58] P. A. Holman, *Magnetoresistance (MR) Transducers And How to Use Them as Sensors*, 2004.

[59] http://www.magneticsensors.com/literature.php

[60] Honeywell, *Magnetic Displacement Sensors HMC1501/1512*, (datasheet)

[61] Procházka, P. and F. Vaněk. (2010).*Contactless Diagnostics of Blade Vibration of Low-Pressure Steam Turbine Stages*, Proceedings of ISMA2010 International Conference on Noise and Vibration Engineering including USD2010. Leuven,Vol. 2420.

[62] E. Cardelli, A. Faba, R. Marsili, G. Rossi, and R. Tomassini, *Magnetic nondestructive testing of rotor blade tips*, Journal of Applied Physics 117.17, 17A705 (2015); doi: 10.1063/1.4907180.

[63] E. Cardelli, A. Faba, F. Tissi, *Surface field measurements in vector characterization of Si-Fe magnetic steel samples*, International Journal of Applied Electromagnetics and Mechanics, Volume 44, Number 3-4, pages 331-338, April 2014.

[64] E. Cardelli, A. Faba, *Vector hysteresis measurements of not oriented grain SiFe steels by a biaxial hall sensors array*, Physica B: Condensed Matter, Vol. 435, p. 34–39, February 2014.

[65] L. Andrenelli, N. Paone and G. L. Rossi, *Large-bandwidth reflection fiber-optic sensors for turbomachinery rotor blade diagnostics*, in Sensors and Actuators A, vol 32, p. 539-542, 1992.

[66] P. Nava, N. Paone, G.L. Rossi and E.P. Tomasini, *Design and experimental characterization of a nonintrusive measurement system of rotating blade vibration*, Journal of engineering for gas turbines and power, vol. 116, p. 657-662, 1994.

[67] J.-F. Brouckaert, R. Marsili, G. Rossi, and R. Tomassini, *Development and experimental characterization of a new non-contact sensor for blade tip timing*, in AIP Conference Proceedings, vol. 1457, p. 61, 2012.

[68] R. Tomassini, G. Rossi, J. Brouckaert, *On the development of a magnetoresistive sensor for blade tip timing and blade tip clearance measurement systems*, 11th International conference on vibration measurements by laser and noncontact techniques AIVELA 2014: Advances and Applications, Vol.1600, AIP Publishing, 2014, pp. 65–73.

[69] Diek, R. H., (2007), *Measurement Uncertainty Methods and Applications*, Systems and Automation Society (ISA)

[70] Castrup, S., and Castrup, HT, (2010), *Measurement Uncertainty Analysis Principles and Methods*, National Aeronautics and Space Administration

[71] Lattime, S.B., Bruce, M.S., (2004), *High-pressure-turbine clearance control systems: current practices and future directions*, Journal of Propulsion and Power, 20.2, 302-311.

[72] Przysowa R. (2014) *Analysis of synchronous blade vibration with the use of linear sine fitting*, Journal of KONBiN, 2(30), pp. 5-20, De Gruyter Open.

Acknowledgements

Thanks go to Professor Gianluca Rossi , Professor Jean-Francois Brouckaert and Professor Tony Arts for the continual advices, support and encouragements provided throughout all the course of this research.

I wish to express my gratitude to Professor Gianluca Rossi and the University of Perugia, to Professor Giampiero Naletto and the CISAS as well as the von Karman Institute to have made this research project possible.

The author would like to acknowledge all the von Karman Institute family for the wonderful international experience, the atmosphere and the personal growth.

The experimental campaign would not have been possible without the precious help and technical advices of Jean-Christophe Desilve, Terence Boyen, Pierre Cuvelier, as well as all the technician staff. Particular thanks to Christophe and Pierre, to have always listened the second question coming after “just one question!”

For the motivation, the continuous encouragements and to have always tried to increase my self-confidence, a special thank goes to Susanna.

A big thank you goes to all that friends that were with me, despite the distance. Particular thanks to Enrico, Matteo, Maurizio, Nicola and Alex.

Finally, I would like to thank my family: Angiolo, Anna Maria and Matteo, for their continuous support and encouragement throughout all my life and Paulina, to have entered in my life.

Appendix

A. The VKI R2 test rig

The VKI high speed compressor facility R-2 is a semi-closed loop test rig for investigation of axial and radial compressors (Fig. 1.). The axial compressor can have a maximum diameter of 500 mm and the casing is large enough to house a two-stage configuration. The facility is driven by a 185 kW DC motor. The rotational speed can vary up to 10,000 RPM and is monitored by an electronic speed control.

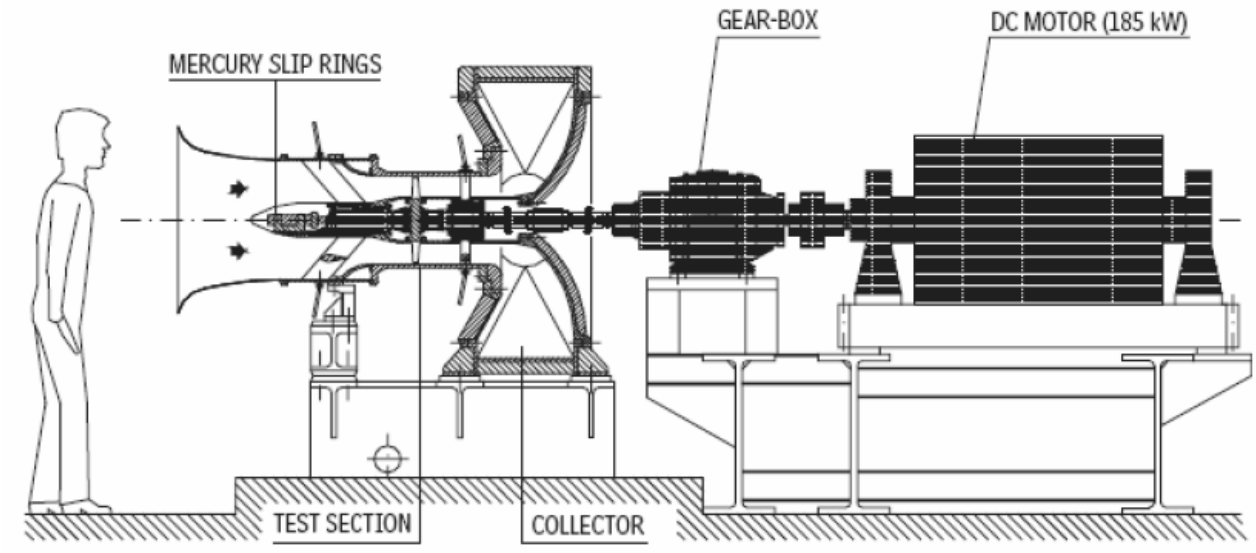

Figure A1 The VKI compressor facility R-2.

The current configuration is a single stage axial compressor installed in a 400 mm diameter test section. The compressor inlet is composed of a bell-shaped inlet duct as shown in Figure 1. The rotor (Fig. 2) is composed of 24 subsonic blades of the NACA 65 family with a hub radius of 100 mm and a tip radius of 200 mm. Figure 4 represents a characteristic section of the rotor blade. The main geometrical characteristics are presented in Table 1. Little is known about the aerodynamic design of this machine because the facility was entirely built around the rotor which was a donation from DLR to VKI in the early 70's for educational purposes.

The stator (Fig. 3) is composed of 30 blades of 50 mm chord made of simple bent and twisted thin metal plates to remove the swirl from the stage exit flow before entering the collector. The stator leading edge plane is located 85 mm downstream of the rotor trailing edge plane (at midspan). After

leaving the stator, the flow is discharged to atmosphere through a collector and an air cooler. The throttling of the massflow is obtained by closing a perforated drum in the collector downstream of the compressor. The valve rotation is tuned using a small 24 V DC electric motor.

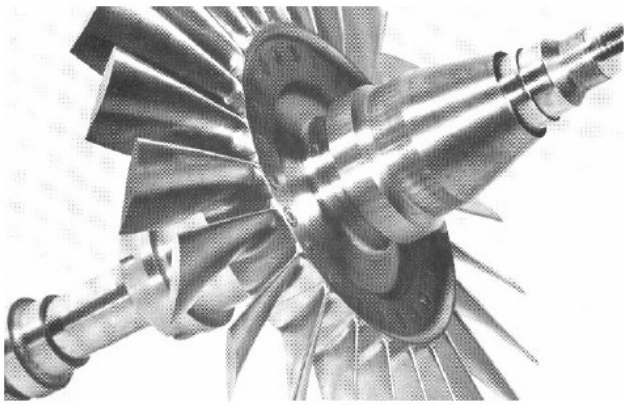

Figure A2 The R-2 compressor rotor.

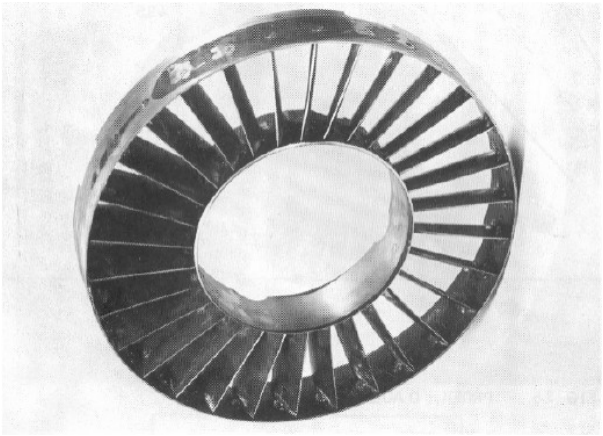

Figure A3 The R-2 compressor stator.

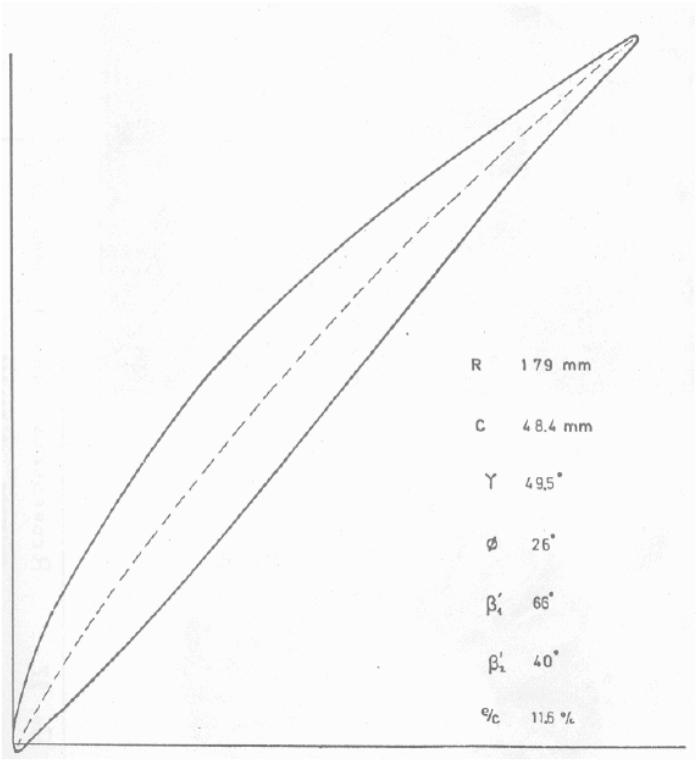

Figure A4 The R-2 compressor rotor blade (NACA 65 type).

Radius $[mm]$	Chord $[mm]$	Stagger γ $[deg]$	Turning θ $[deg]$	Thickness $\frac{e}{c}$ $[\%]$	$\sigma = \frac{c}{g}$ $[-]$
195	49.0	58.0	21.0	11.0	1.000
180	48.4	49.0	26.0	11.5	1.030
150	45.6	40.0	32.0	12.3	1.154
130	41.6	32.0	34.0	13.5	1.220
105	40.0	17.5	35.0	19.0	1.440

Table A1 Blade geometry of the R-2 compressor rotor.

The performance map of the compressor is presented in Figure 5 where the nominal rotational speed corresponds to 10,000 RPM. Presently, the maximum rotational speed of the compressor is limited to 6000 RPM. This is due to the limitation on peripheral speed of the seals used on the shaft.

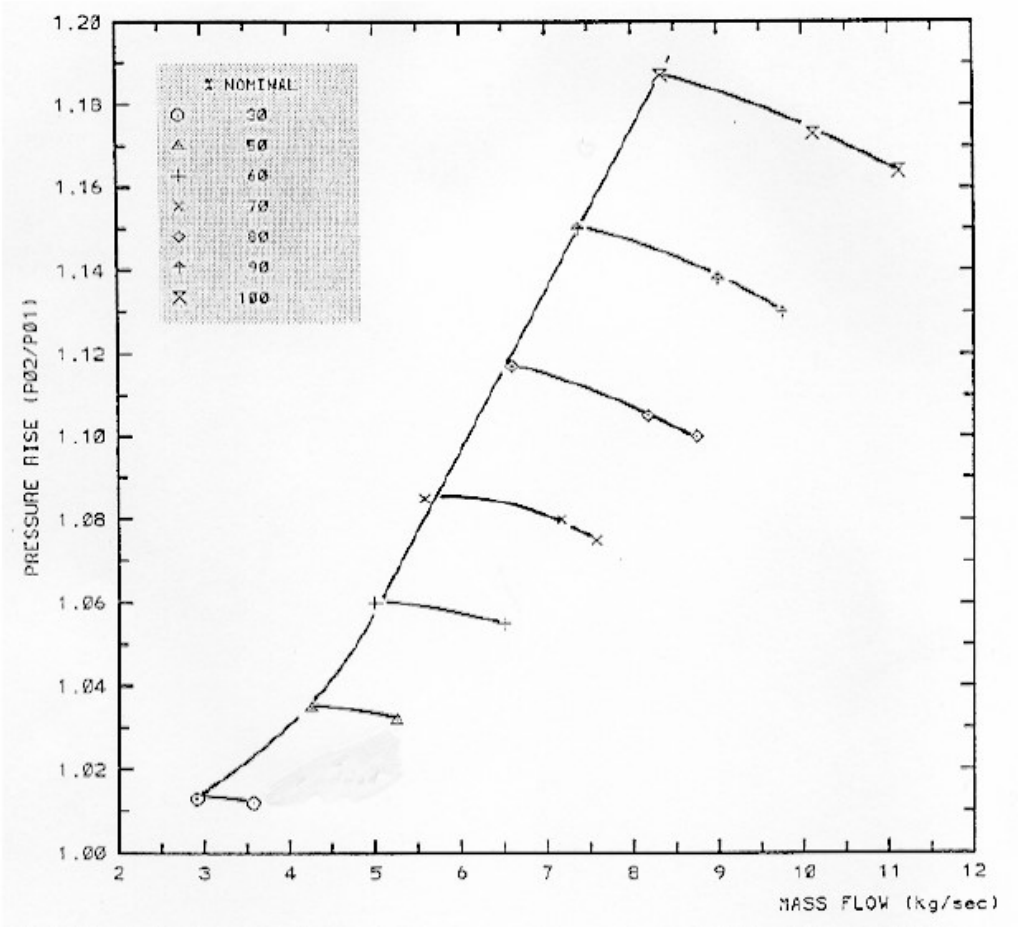

Figure A5 Performance map of the R-2 compressor.

Instrumentation

Figure 6 shows a general view of the facility. Four circumferential locations (every 90º) allow the insertion of probes upstream and downstream of the rotor.

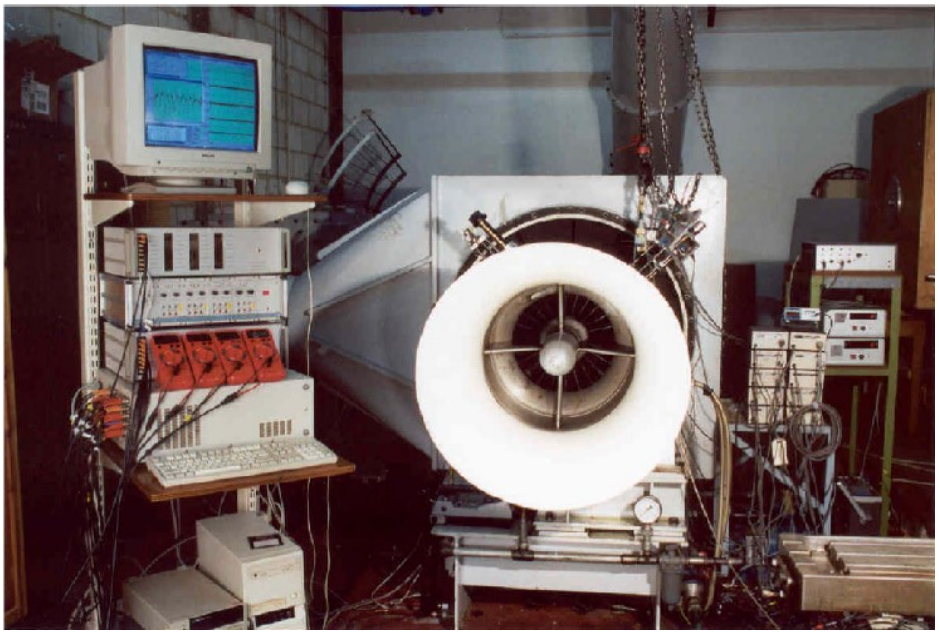

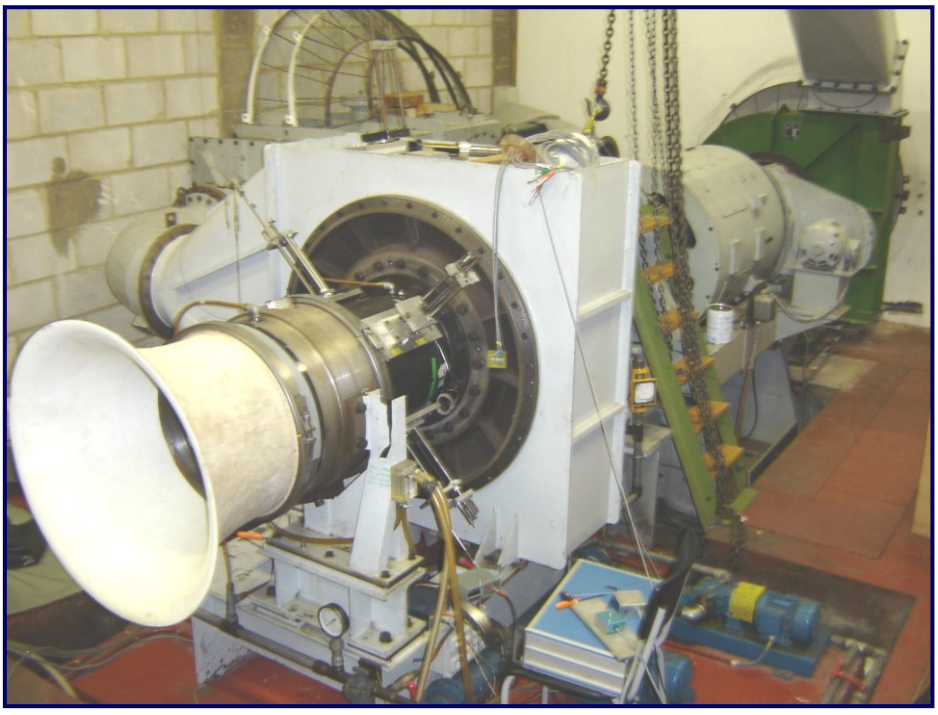

Figure A6 Instrumentation on the VKI high speed compressor facility R-2.

Figure 7 shows a view of one of the 4 instrumentation access windows (40mm x 285mm) showing also the rotor blade tip. The angular sector corresponding to the opening is 11.65 degrees. The access window is closed by an aluminium plate which allows easy modifications for insertion of probes, pressure sensors, tip timing and tip clearance sensors, infinite line probes, etc. A technical sketch of such a plate is given in Figure 8. A standard adaptor fitting could be specified in common agreement with sensor providers to fit in different sensors at the same location.

Figure A7 View of an instrumentation access window.

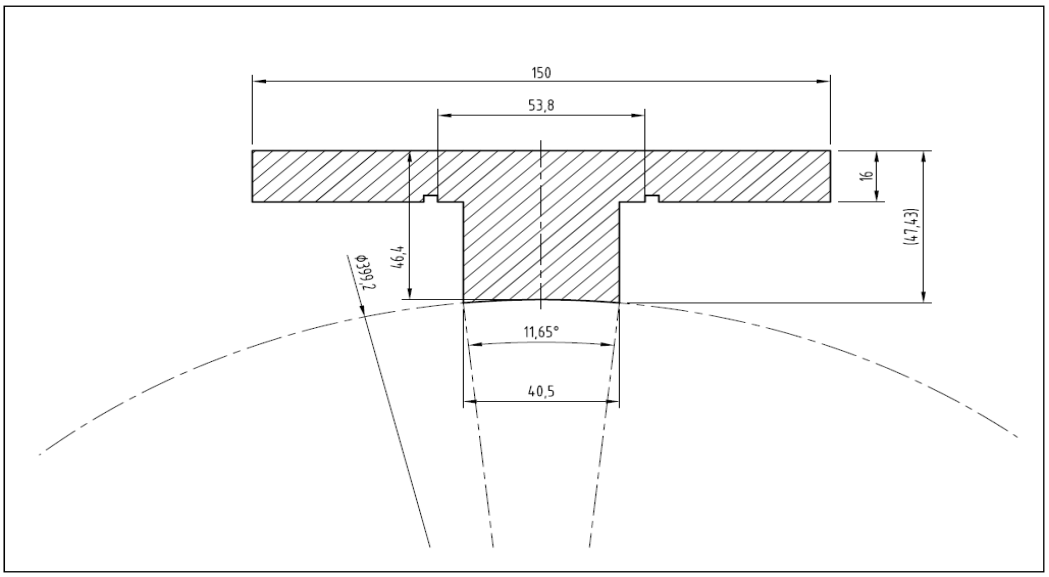

Figure A8 Sketch of instrumentation closing plate.

Other specific aspects of the rig related to tip timing

An existing inlet distortion grid may be installed in front of the rotor. It is composed of 4 sectors which can be installed together or separately at various axial distances from the rotor leading edge. The grid is made of 24 cylindrical bars of 3 mm diameter. Figure 9 shows a quarter of the inlet distortion grid installed in front of the rotor.

Figure A9 Partial inlet distortion grid installed at the compressor inlet.

Regarding tip clearance measurements, simple thickness gauge data have been taken at leading edge, mid-chord and trailing edge of the rotor, which are shown in Fig. 10. The average tip clearance is ~ 0.64 mm.

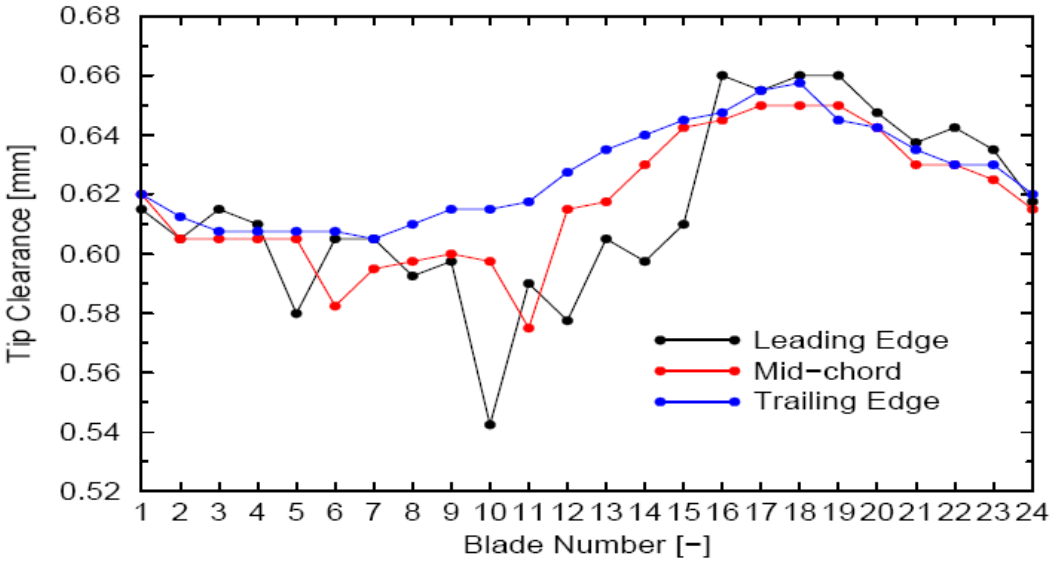

Figure A10 Rotor tip clearance distribution.

B. The magnetoresistive sensing element - Honeywell HMC1501

HMC1501/1512

SCHEMATIC DIAGRAMS

HMC1501 HMC1512

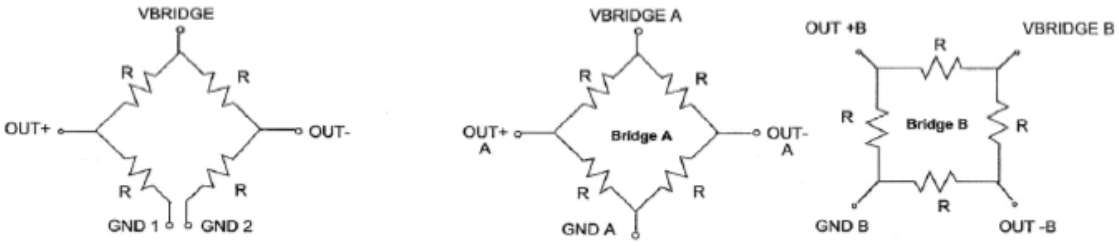

PIN CONFIGURATIONS

HMC1501

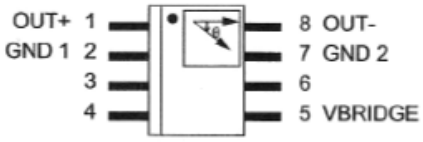

HMC1512

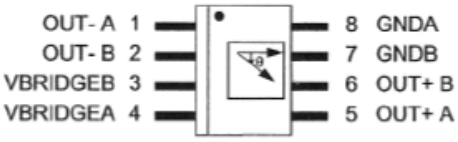

PACKAGE OUTLINE

PACKAGE DRAWING HMC1501/HMC1512 (8-PIN SOIC, dimensions in millimeters)

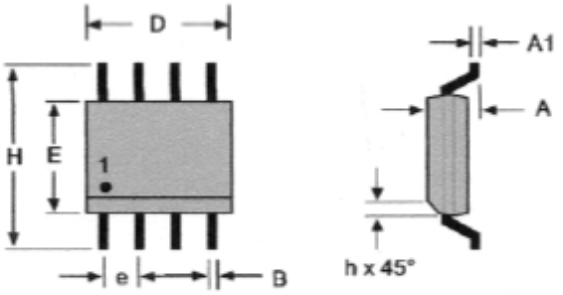

	Millimeters		Inches	
	Min	Max	Min	Max
A	1.371	1.728	0.054	0.068
A1	0.101	0.249	0.004	0.010
B	0.355	0.483	0.014	0.019
D	4.800	4.979	0.189	0.196
E	3.810	3.988	0.150	0.157
e	1.270 ref		0.050 ref	
H	5.816	6.198	0.229	0.244
h	0.381	0.762	0.015	0.030

Figure B1 Schematic diagrams and package outline

SPECIFICATIONS

Characteristics	Conditions*	Min	Typ	Max	Units
HMC1512 Bridge Elements					
Supply	Vbridge (Vb) referenced to GND	1.0	5.0	25	Volts
Resistance	Bridge current = 1mA	2000	2100	2800	ohms
Angle range	>Saturation Field	-90		+90	deg
Sensitivity	Vb=5 volts, field=80Oe @ zero crossing @ zero crossing averaged in a 45° range		 2.1 1.8		 mV/° mV/°
Output Voltage	Vb=5 volts, field=80 Oe	100	120	140	mVpp
Bridge Offset	field=80 Oe Bridge A Bridge B	 -7 -7	 0 0	 +7 +7	 mV/V mV/V
Resolution	BW=10Hz, Vb=5 volts		0.05		deg
Noise Density	@1Hz, Vb=5 volts		70		nV/sqrt Hz
Common					
Operating Temperature	Ambient	-40		+125	°C
Storage Temperature	Ambient, unbiased	-55		+150	°C
Humidity	Tested at 85°C			85	%
Hysteresis Error	Field > 80 Oe, Vb=5 volts		30 0.017		µV deg
Bridge Ohmic Tempco	Vb=5 volts, T_A= -40 to +125°C		2800		ppm/°C
Sensitivity Tempco	Vb=5 volts, T_A= -40 to +125°C		-3200		ppm/°C
Bridge Offset Tempco	T_A= -40 to +125°C		±100		ppm/°C

* Tested at 25°C except stated otherwise.

Figure B2 Specifications

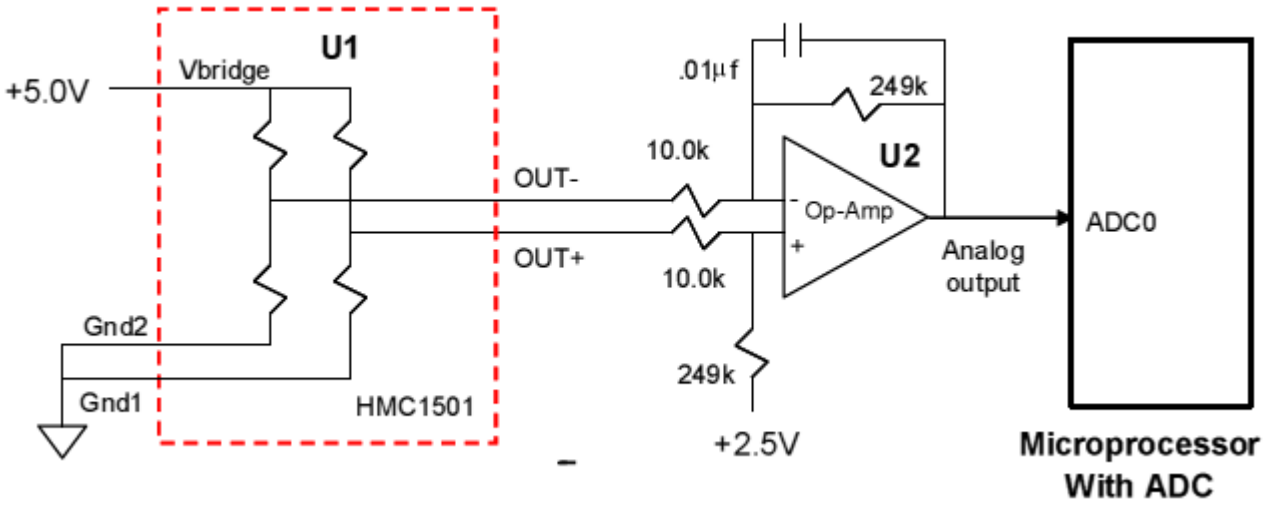

Figure B3 Basic electronic circuit

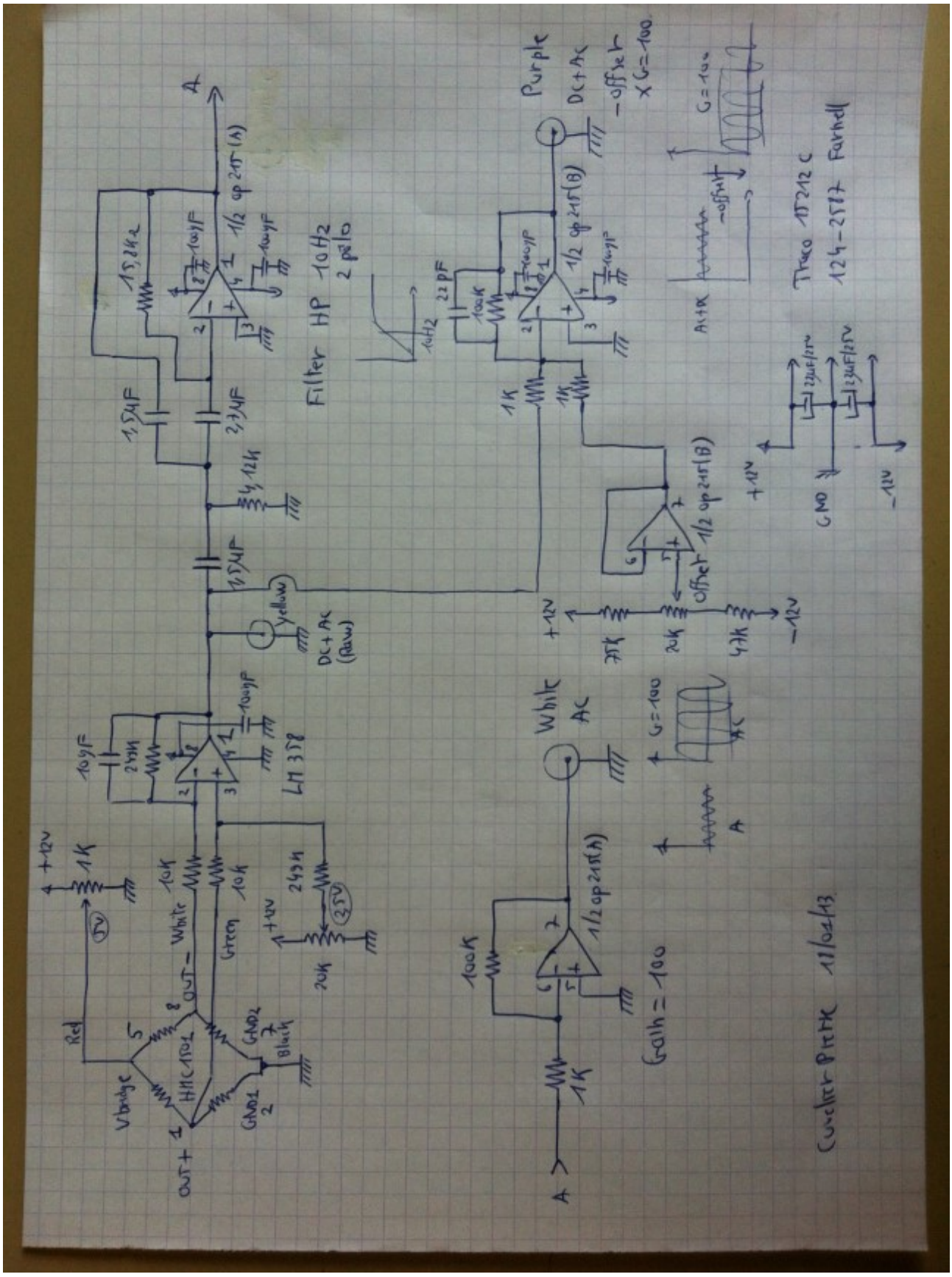

Figure B4 Scheme of the electric circuit of the analogue sensor

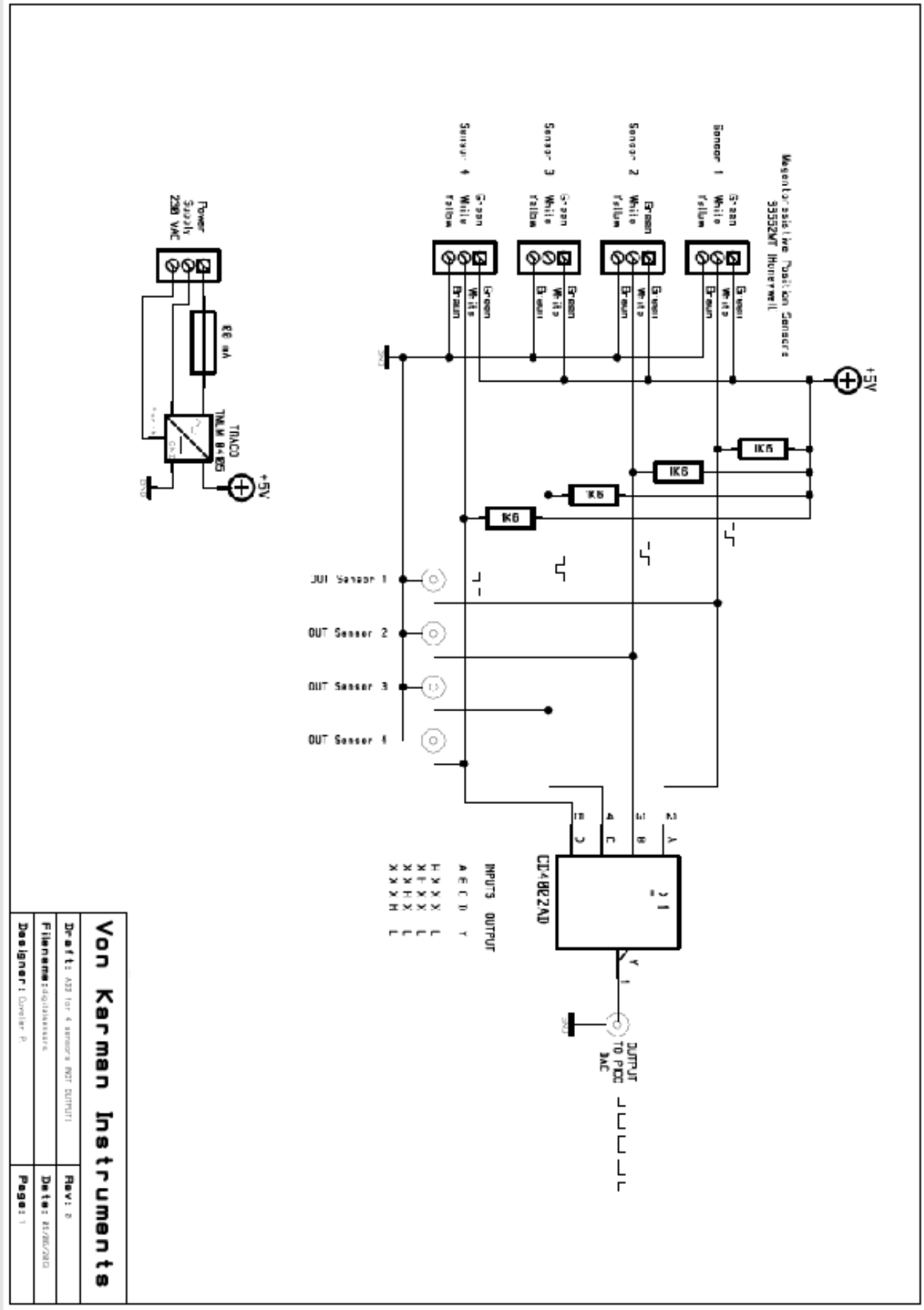

Figure B5 Scheme of the electric circuit of the digital sensor

C. The data acquisition system

MODEL	PicoScope 4424	PicoScope 4224
INPUTS		
Number of channels	4 BNC inputs	2 BNC inputs
Analog bandwidth	20 MHz (10 MHz on ±50 mV range)	
Voltage ranges	±50 mV to ±100 V	
Sensitivity	10 mV/div to 20 V/div	
Vertical resolution	12 bits (up to 16 bits with resolution enhancement)	
Input coupling	AC or DC, software-controlled	
Input impedance	1 MΩ || 22 pF	
Overvoltage protection	±200 V	
SAMPLING		
Timebases	100 ns/div to 200 s/div	
Maximum sampling rate (real-time)	1/2 channels: 80 MS/s 3/4 channels: 20 MS/s	80 MS/s
Buffer size	32 M samples shared between active channels	

Figure C1 The PicoScope 4424

MODEL	BANDWIDTH	SAMPLING	MEMORY	AWG
PicoScope 5204	250 MHz	1 GS/s	128 MS	YES
PicoScope 5203	250 MHz	1 GS/s	32 MS	YES

MODEL	PicoScope 5203	PicoScope 5204
Number of channels	2	
Vertical resolution	8 bits	
Analog bandwidth	250 MHz	
Maximum sampling rate (real time)		
One channel in use	1 GS/s	
Two channels in use	500 MS/s	
Maximum sampling rate (repetitive signals)	20 GS/s	
Buffer size	32 MS	128 MS
	If two channels in use, buffer shared between channels	
Inputs		
Input characteristics	BNC, 1 MΩ in parallel with about 15 pF	
Coupling	Selectable AC/DC	
Voltage ranges	±100 mV, ±200 mV, ±500 mV, ±1 V, ±2 V, ±5 V, ±10 V, ±20 V	
Accuracy	3%	
Overvoltage protection	±100 V	
Timebase		
Range	5 ns/div to 100 s/div	
Accuracy	50 ppm	

Figure C2 The PicoScope 5204

D. Blade Tip Clearance

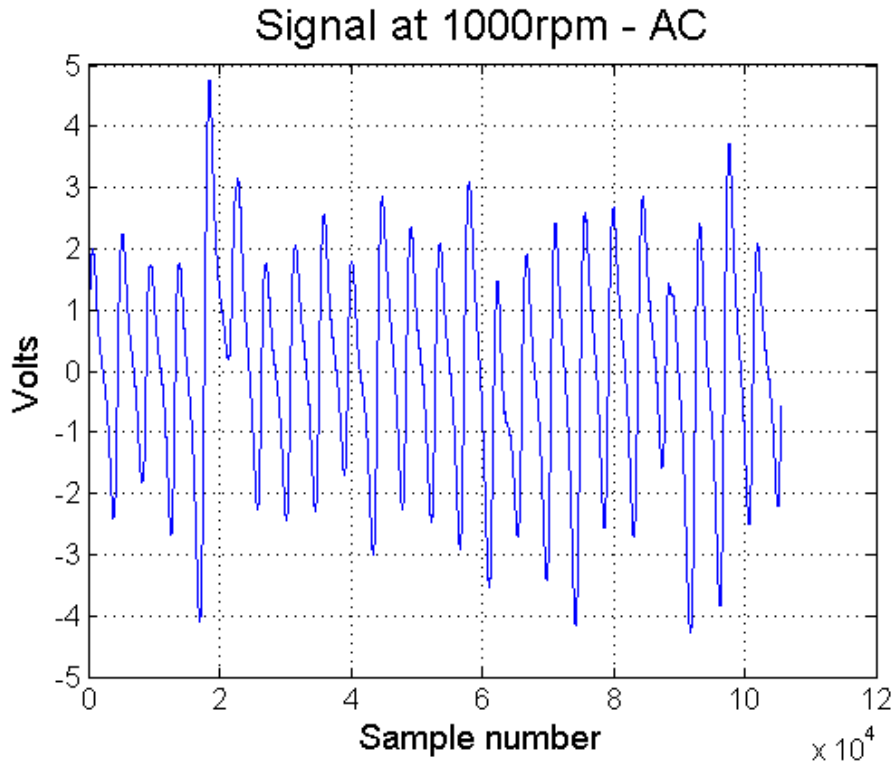

Figure D1 Acquired signal at 1000rpm

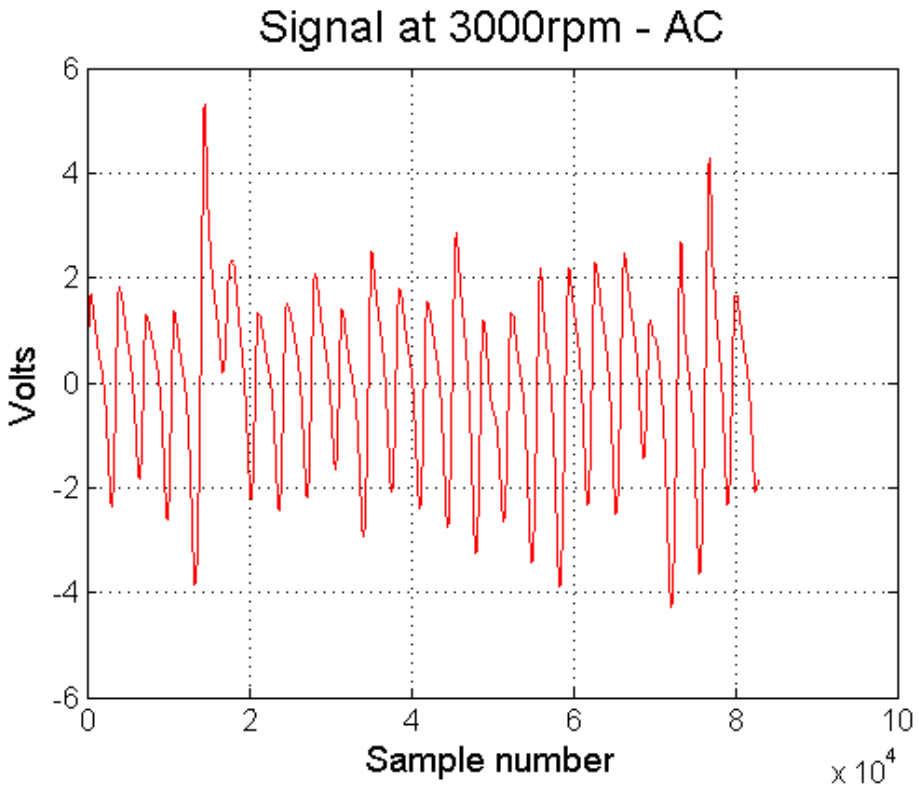

Figure D2 Acquired signal at 3000rpm

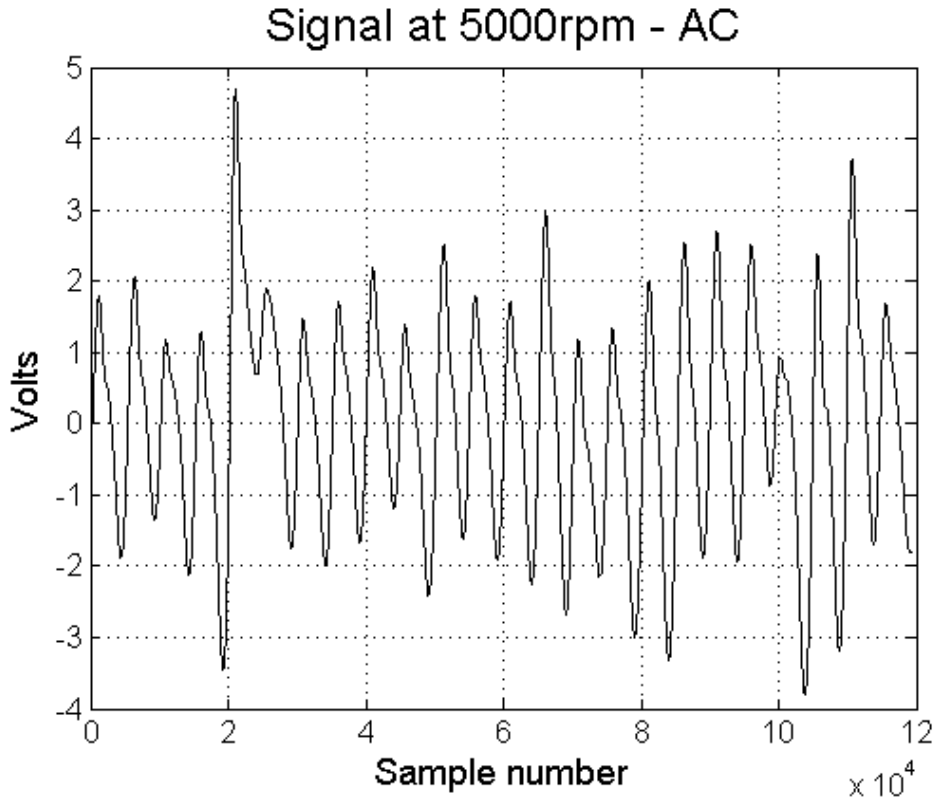

Figure D3 Acquired signal at 5000rpm

Uncertainty analysis

Standard Deviation, S_X Used to estimate the limits of random error $s_X = \sqrt{\frac{\sum_{i=1}^{N}(X_i - \overline{X})^2}{N-1}}$	Systematic Standard Uncertainty = $b_R = \left[\sum_{i=1}^{N}(b_i)^2\right]^{1/2}$
Random Standard Uncertainty, $s_{\overline{X}}$ Used to estimate the random uncertainty $s_{\overline{X}} = \frac{s_X}{\sqrt{N}}$	Random Standard Uncertainty = $s_{\overline{X},R} = \left[\sum_{i=1}^{N}(s_{\overline{X},i})^2\right]^{1/2}$ where i = the ith random uncertainty source

Table D1 Random and Systematic components of the uncertainty

Considering the above mentioned quantities, in this case the values that have been taken during the calibrations, are according to what follows:

-The systematic component has been considered equal to the comparator resolution = 0.01mm;

-The standard deviation has been evaluated during the fitting of the experimental data. N, the number of points used to obtain the calibration curve was 23 (Figure 2.15).

	systematic component	standard deviation	N	random component
calibration	0,01	0,00244875	23	0,0005106
t95	2,069			
U95	**0,021878087**			

Table D2 Uncertainty calculations

The estimated value of uncertainty is reported in Table D.2. The definition used for the calculation is shown below, with the values of the t-student's distribution.

$$U_{95} = \pm t_{95}\left[(b_R)^2 + \left(s_{\bar{X},R}\right)^2\right]^{1/2}$$

Student's t_{95}

Degrees of freedom	t_{95}	Degrees of freedom	t_{95}	Degrees of freedom	t_{95}
1	12.706	11	2.201	21	2.080
2	4.303	12	2.179	22	2.074
3	3.182	13	2.160	23	2.069
4	2.776	14	2.145	24	2.064
5	2.571	15	2.131	25	2.060
6	2.447	16	2.120	26	2.056
7	2.365	17	2.110	27	2.052
8	2.306	18	2.101	28	2.048
9	2.262	19	2.093	29	2.045
10	2.228	20	2.086	30+	2.000

Assumption:

At that stage, the temperature effect has not been taken into account. This effect has been considered negligible considering that, the test duration was less than 60 seconds, performed at ambient temperature, in the lathe, at 45 rpm. Moreover, the sensing element is a Wheatstone bridge of Permalloy elements and it should compensate the temperature unbalance itself. Anyway, for future characterization at high speed, it should be considered.

E. The Universal Calibration Bench

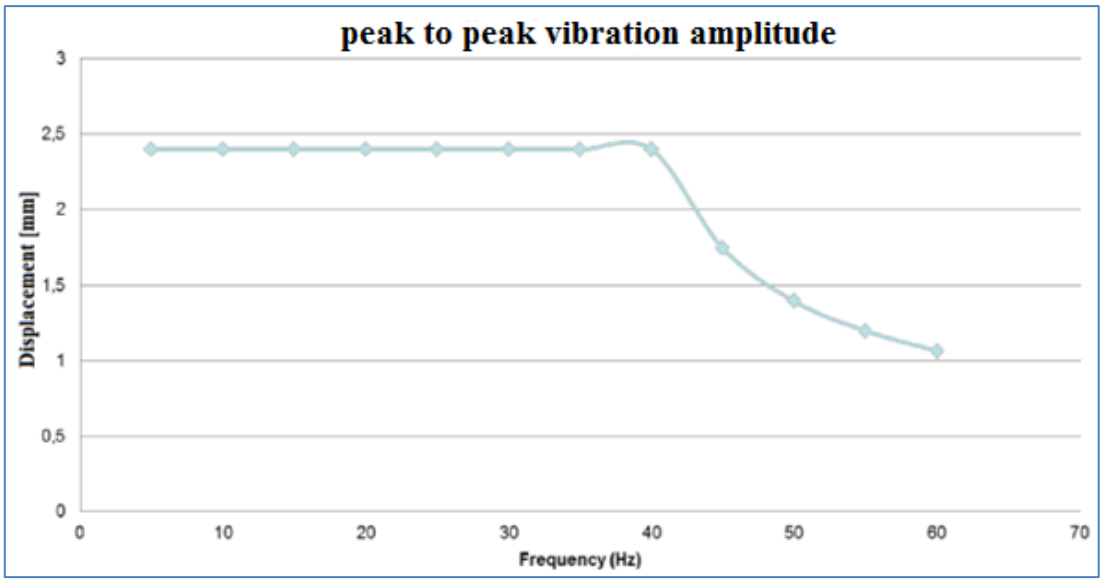

Figure E1 Maximum achievable displacements in function of the frequency

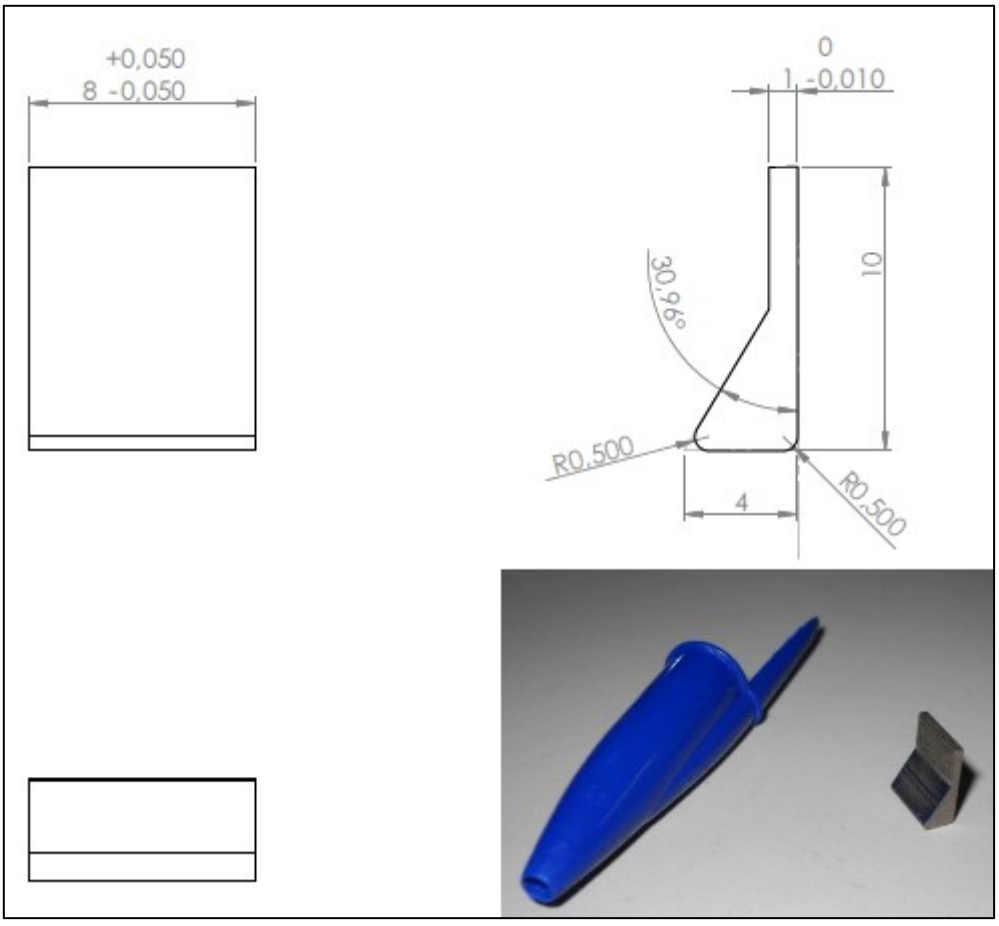

Figure E2 The new rotor blade

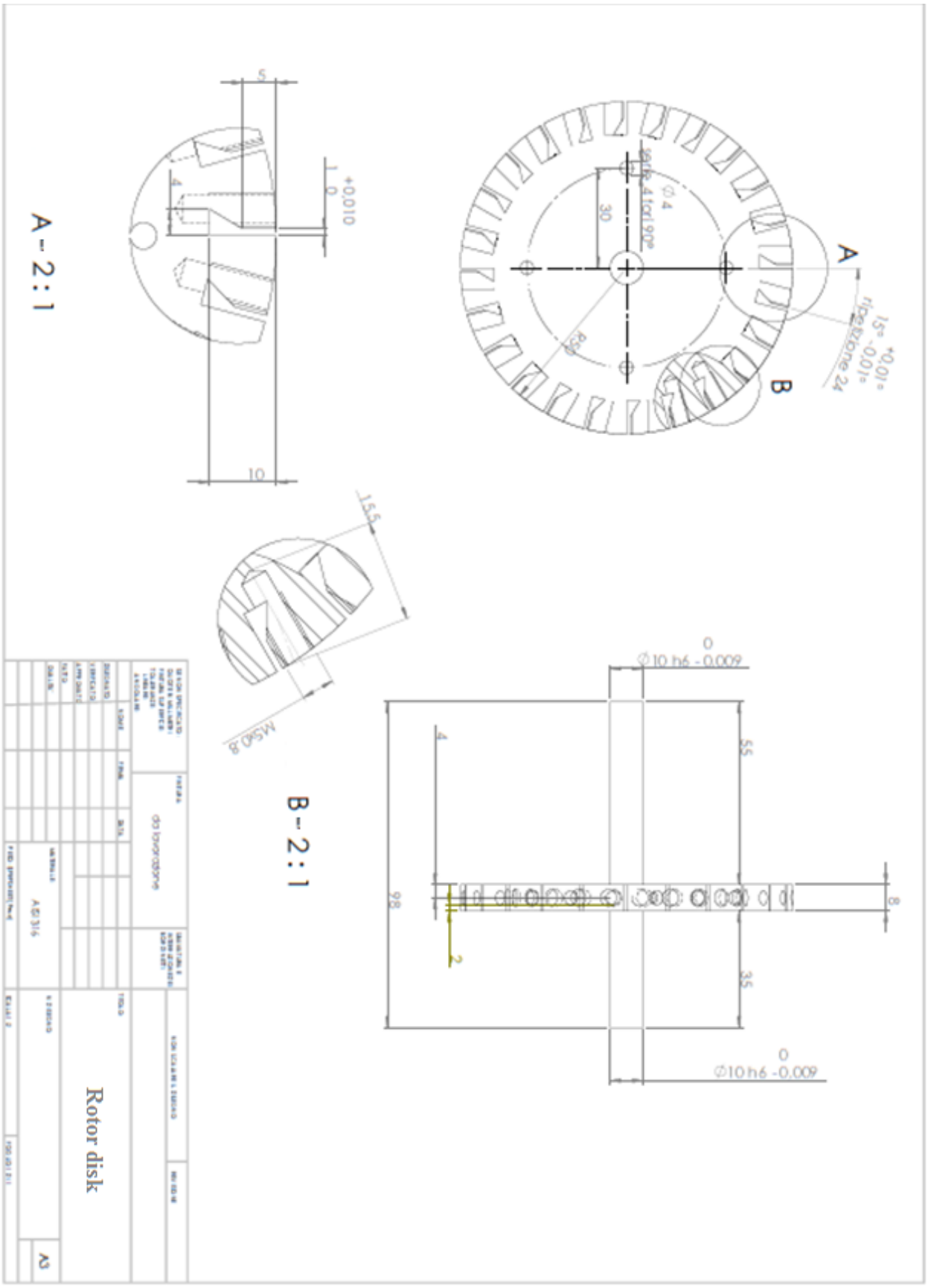

Figure E3 The new rotor disk

F. Optimization of the sensor components

The magnets used during the experimental investigation have been bought form:

http://www.supermagnete.de/eng

1. Technical information

Article	S-04-25-N	
Shape	Rod	
Diameter	4 mm	
Height	25 mm	
Tolerance in size	+/- 0,1 mm	
Direction of magnetisation	axial (parallel to height)	
Material	NdFeB (Neodymium Iron Boron)	
Type of coating	Nickel (Ni-Cu-Ni)	
Strength	approx. 580 g	approx. 5,69 N
Weight	2,3876 g	
Manufacturing method	sintered	
Magnetisation (Grade)	N42	
Max. working temperature	80 °C	
Curie temperature	310 °C	
Residual magnetism Br	12900-13200 G	1.29-1.32 T
Coercive field strength bHc	10.8-12.0 kOe	860-955 kA/m
Coercive field strength iHc	≥12 kOe	≥955 kA/m
Energy product (BxH)max	40-42 MGOe	318-334 kJ/m^3

Figure F1 The cylindrical magnet

1. Technical information

Article	W-05-G	
Shape	Cube	
Length	5 mm	
Tolerance in size	+/- 0,1 mm	
Material	NdFeB (Neodymium Iron Boron)	
Type of coating	Gold-plated nickel (Ni-Cu-Ni-Au)	
Strength	approx. 1,1 kg	approx. 10,8 N
Weight	0,95 g	
Manufacturing method	sintered	
Magnetisation (Grade)	N42	
Max. working temperature	80 °C	
Curie temperature	310 °C	
Residual magnetism Br	12900-13200 G	1.29-1.32 T
Coercive field strength bHc	10.8-12.0 kOe	860-955 kA/m
Coercive field strength iHc	≥12 kOe	≥955 kA/m
Energy product (BxH)max	40-42 MGOe	318-334 kJ/m^3

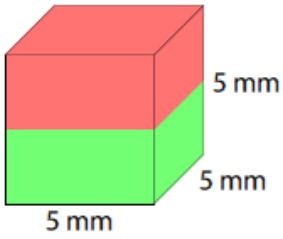

Figure F2 The cubic magnet

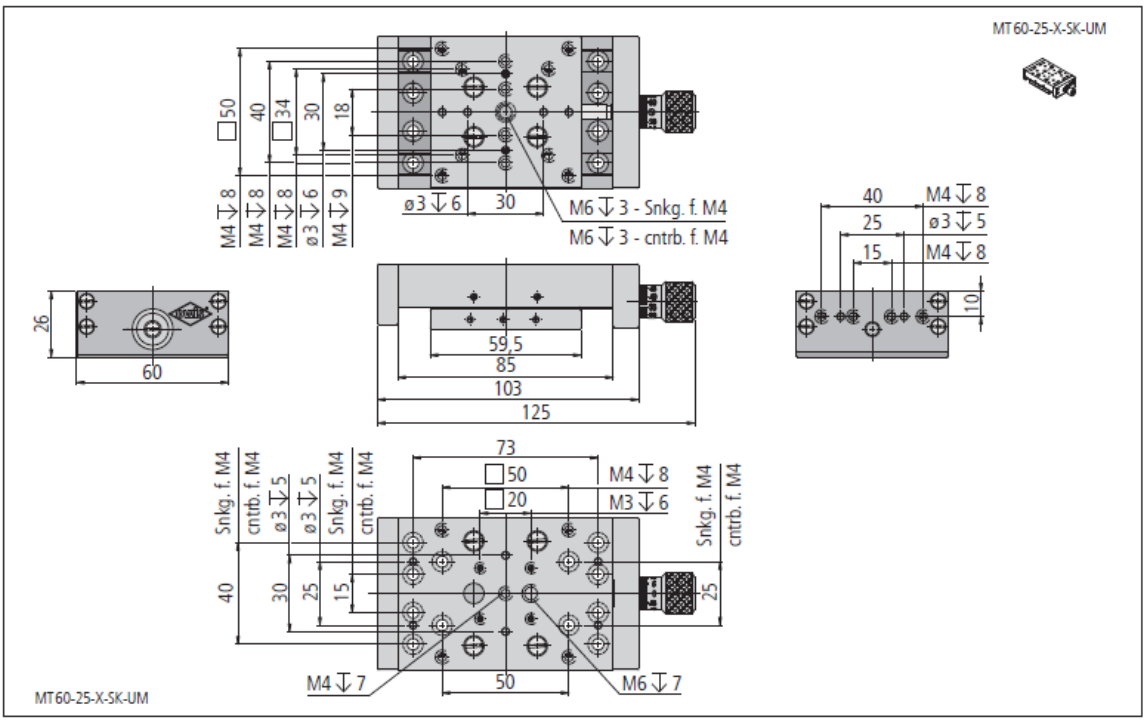

travel	25	mm
load capacity	max. 90	N
tilting moment (Mx, My, Mz)	max. 7,8	Nm
spindle pitch	0,5	mm
graduation of scale	10	µm
setting sensitivity	2	µm
permeability μ_r	< 1,01	
weight	360/730/1100	g

Figure F3 The linear slider

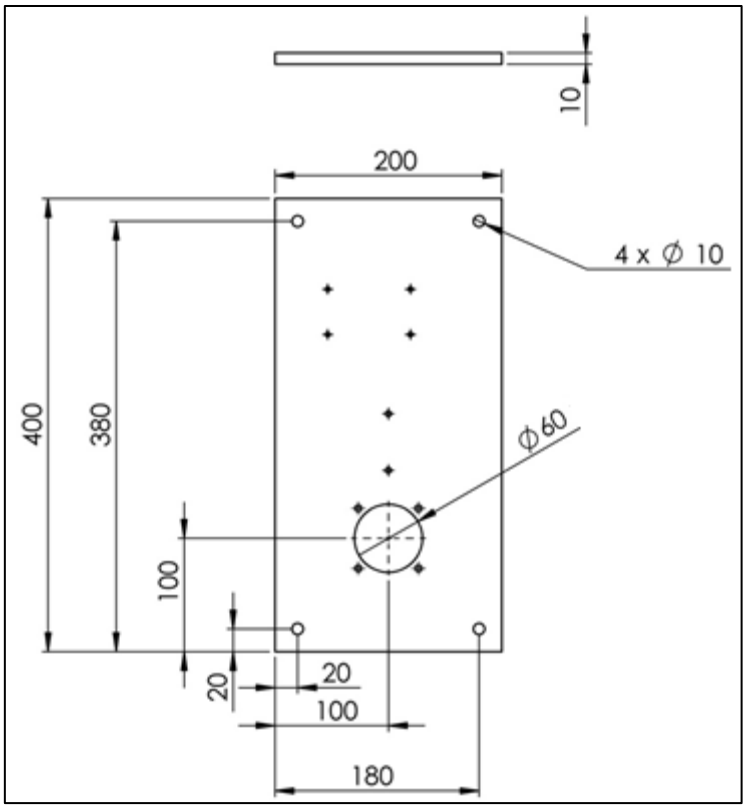

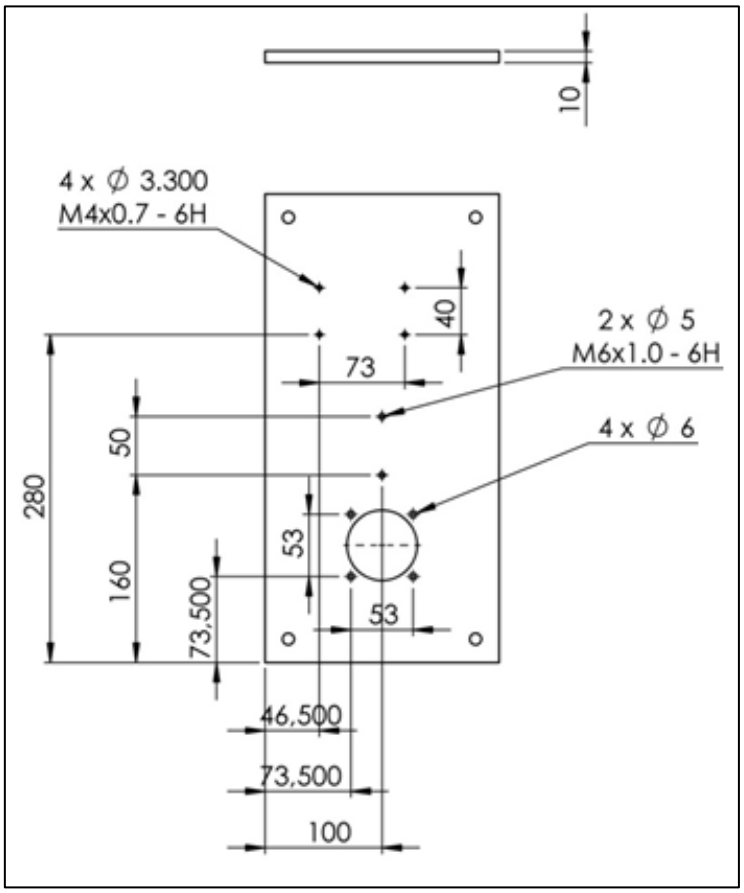

Figure F4 Base plate drawings

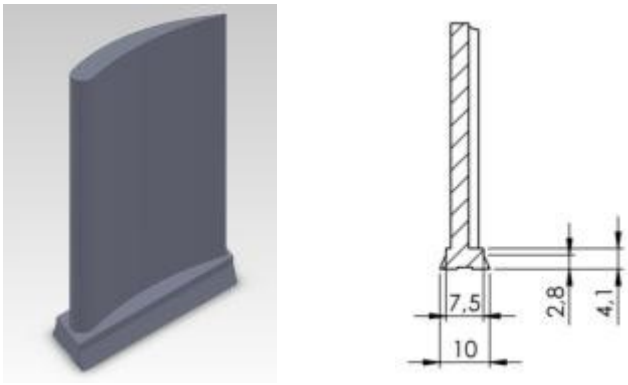

Figure F5 The drawing of the blade

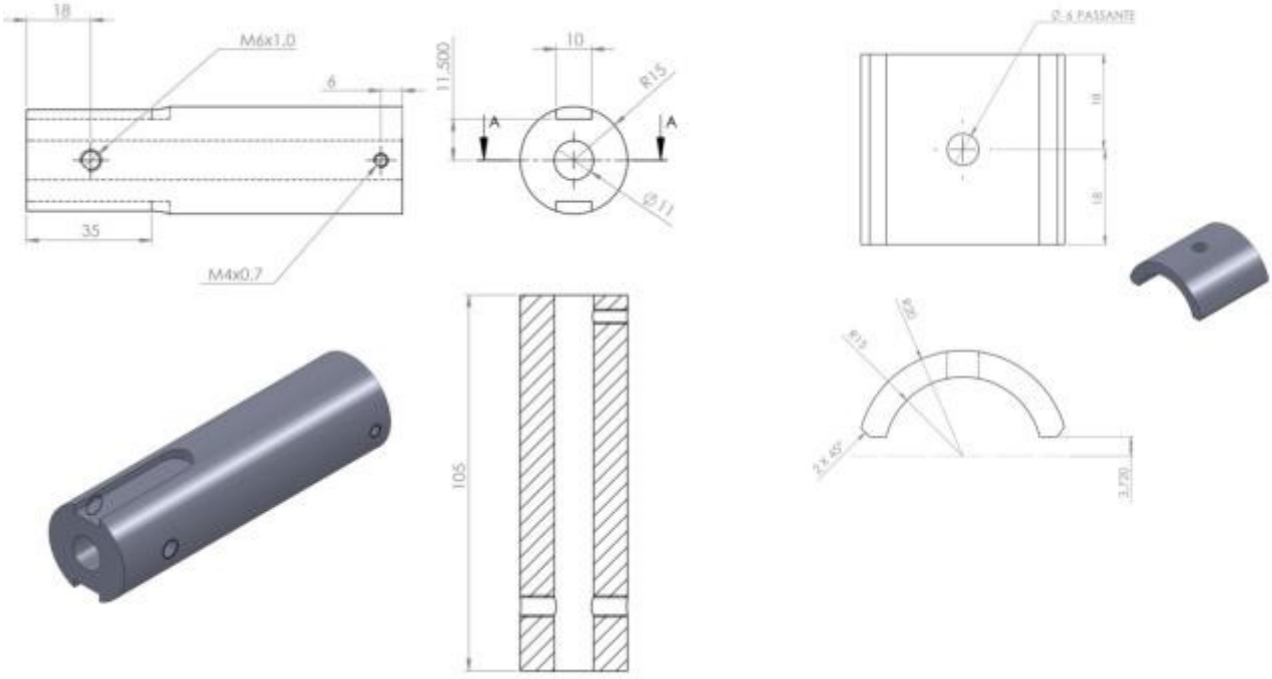

Figure F6 The shaft and the flange

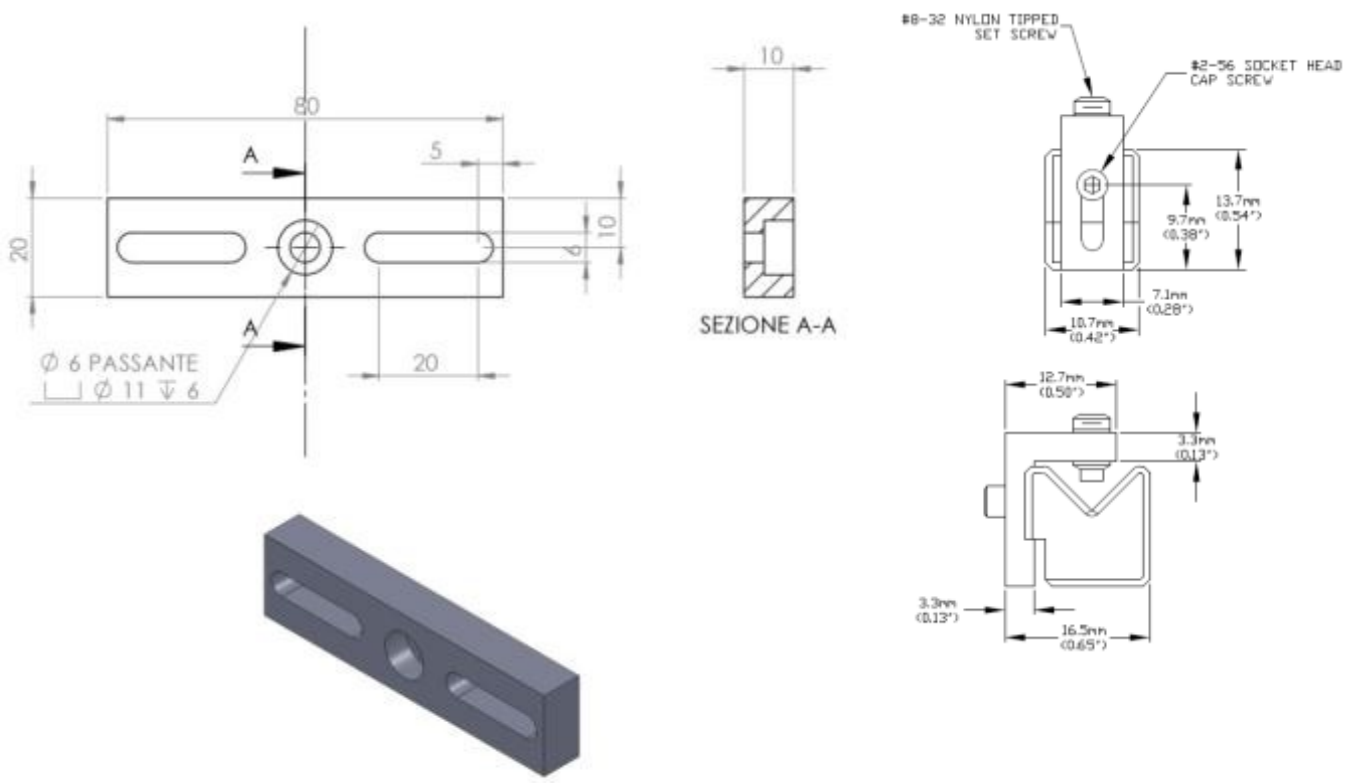

Figure F7 The sensor housing support

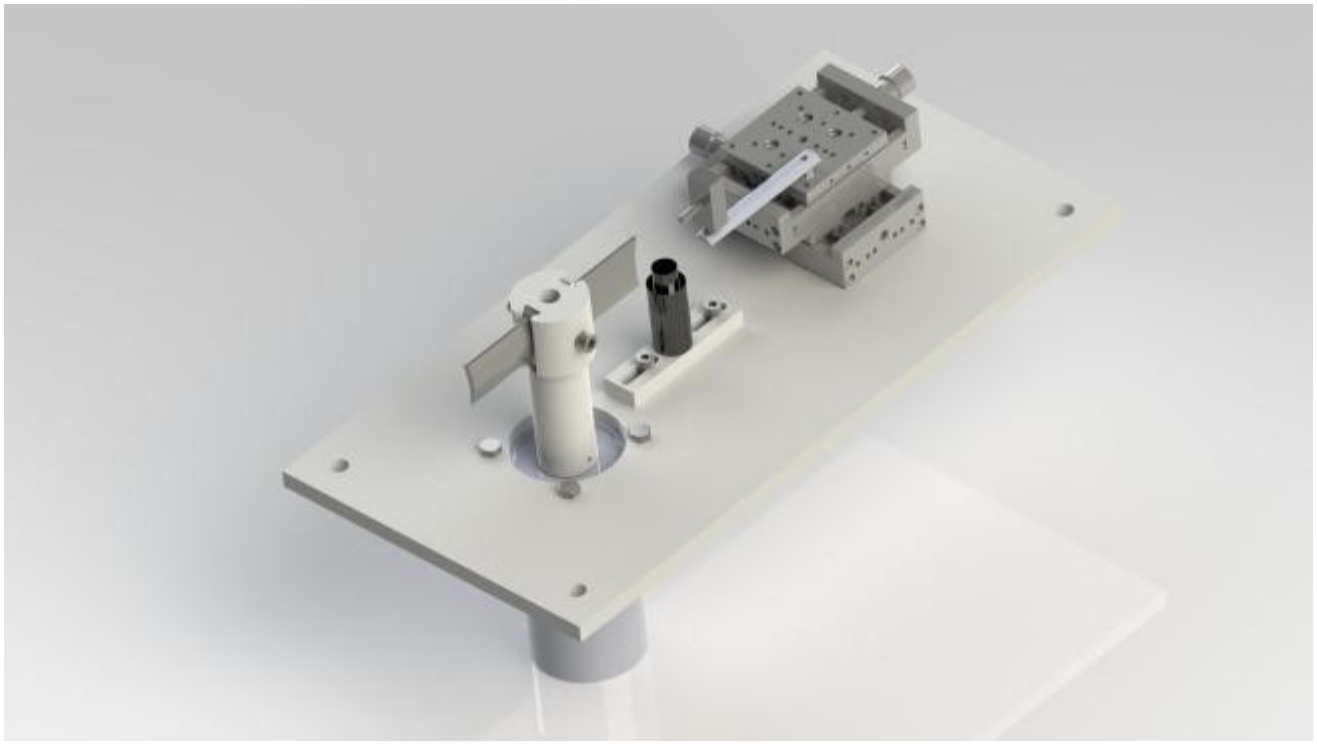

Figure F8 Rendering of the CAD assembly

			y axis				
	position [mm]		**20**	**15**	**10**	**5**	**0**
		slider [mm]	0	5	10	15	20
x axis	**39**	-10	39,50	39,25	35,32	32,25	30,28
	34	-5	39,80	39,70	37,15	34,02	32,30
	29	0	37,24	37,03	35,82	34,19	33,45
	24	5	20,08	28,43	30,33	31,08	31,75
	19	10	14,34	14,60	20,69	24,77	27,00
	14	15	23,75	8,80	9,38	16,50	19,95
	9	20	34,95	22,42	5,09	7,76	11,02

Table F1 Peak to peak output signal values

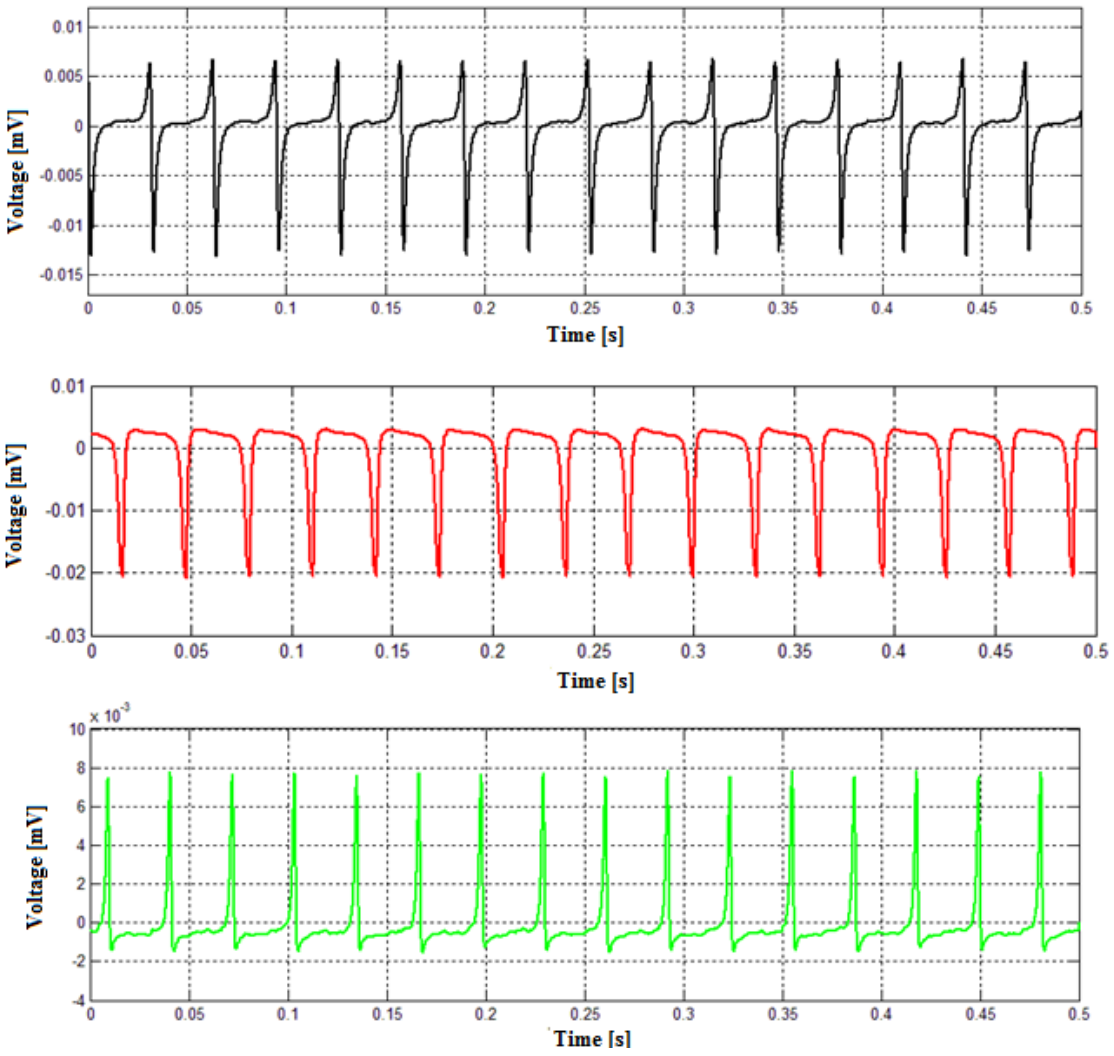

Figure F9 The different output signal shapes observed

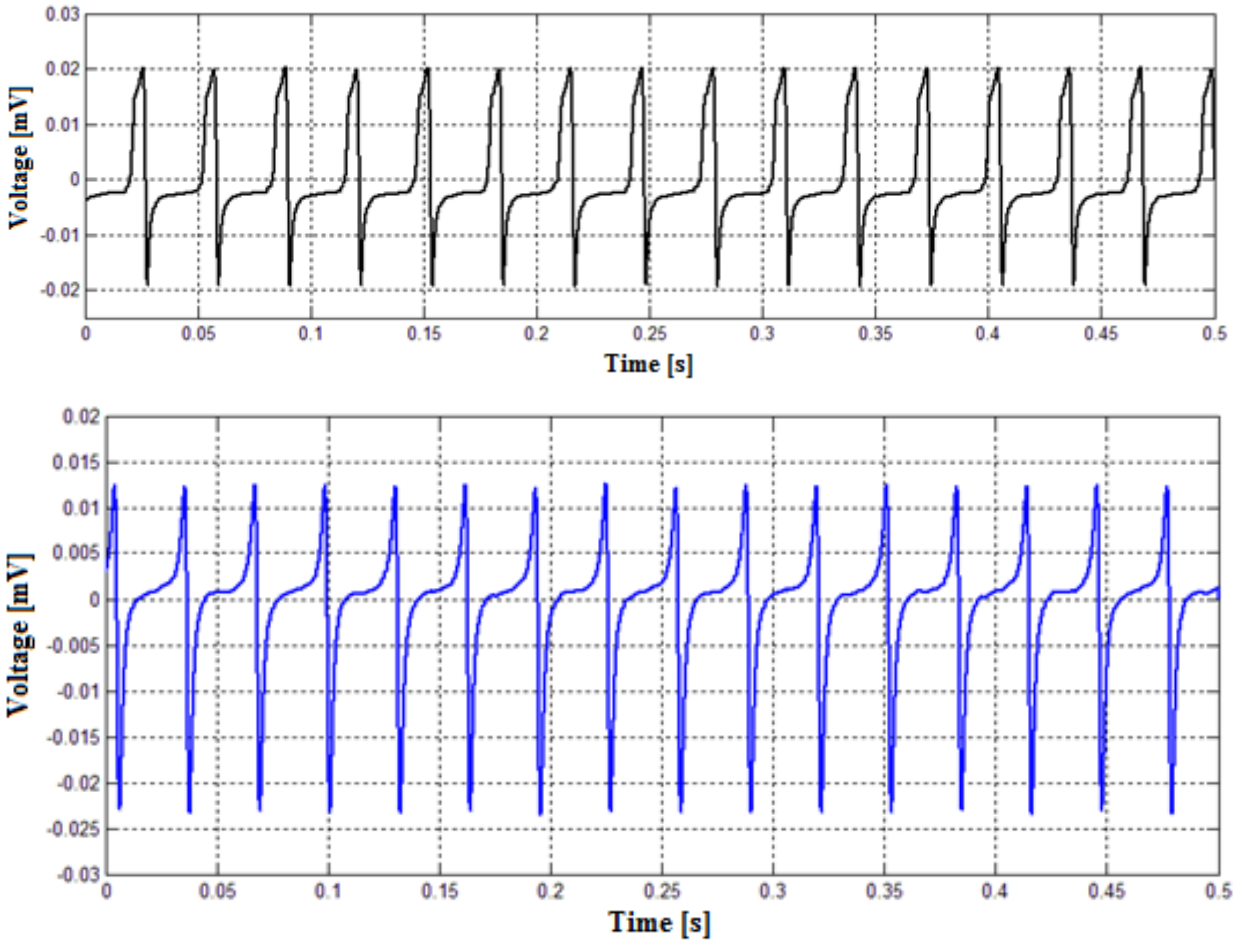

Figure F10 The maximum output signals obtained with the cylindrical magnet (top) and with the cubic magnet (bottom)